Deep Learning Approach for the Automated Characterization of Cardiac Mechanics

by

Manuel Antonio Morales

B.S., University of Central Florida (2015)

Submitted to the Harvard-MIT Division of Health Sciences and Technology
in partial fulfillment of the requirements for the degree of

Doctor of Philosophy in Medical Engineering and Medical Physics

at the

MASSACHUSETTS INSTITUTE OF TECHNOLOGY

June 2021

Author .....
Harvard-MIT Division of Health Sciences and Technology
May 10, 2021

Certified by .....
Ciprian Catana
Associate Professor in Radiology, Harvard Medical School
Thesis Supervisor

Accepted by .....
Emery N. Brown, MD, PhD
Director, Harvard-MIT Program in Health Sciences and Technology
Professor of Computational Neuroscience and Health Sciences and Technology

Deep Learning Approach for the Automated Characterization of Cardiac Mechanics

by

Manuel Antonio Morales

Submitted to the Harvard-MIT Division of Health Sciences and Technology
on May 10, 2021, in partial fulfillment of the
requirements for the degree of
Doctor of Philosophy in Medical Engineering and Medical Physics

Abstract

Cardiac mechanics reflects the precise interplay between myocardial structure and contraction essential for sustaining the blood pumping function of the heart. Ejection fraction is the usual index of function, yet mechanical impairment and even heart failure may occur without changes in this measure. Strain analysis provides more meaningful measures through non-invasive evaluation of myocardial deformation from cardiac magnetic resonance imaging data, and can therefore identify dysfunction before reduction in ejection fraction. Diagnosis based on strain measures requires highly accurate and repeatable cardiac tissue detection, labelling, and tracking. These are very challenging and time-consuming tasks requiring extensive technical and clinical expertise, and have many sources of error that limit the wider clinical adoption of strain analysis.

In this thesis, a novel deep learning workflow termed DeepStrain was developed and validated to provide automated strain analysis from standard magnetic resonance data. DeepStrain integrates three convolutional neural networks designed specifically for accurate and precise myocardial tissue detection, labelling, and tracking. These networks were trained using data from healthy subjects and cardiac patients. In healthy subjects, accuracy was evaluated using the gold standard strain analysis technique, and repeatability was assessed using data from subjects imaged multiple times. Finally, DeepStrain was tested in a prospective cross-sectional study in asymptomatic young adults with a mixture of cardiovascular disease risks factors, i.e., overweight, hypertension, and type 2 diabetes mellitus. In summary, DeepStrain automatically provides very precise measures of strain two orders of magnitude faster than current technology, enabling more accurate and comprehensive characterization of cardiac mechanics.

Thesis Supervisor: Ciprian Catana
Title: Associate Professor in Radiology, Harvard Medical School

Acknowledgments

It takes a community to raise good citizens, and it takes the collective effort of mentors, friends, and family to transform them into great scientists. I am honored and humbled to have received so much unwavering and unconditional support from so many wonderful people during this long journey.

I am deeply grateful to my advisor Ciprian Catana: for the many hours we have spent together thinking and writing about medicine and science; for inspiring me to pursue bigger goals; and for supporting and believing in my potential to do impactful research. All these experiences have taught me many lessons, and given me many valuable tools I will carry with me throughout my career.

I am truly thankful to my thesis committee for their enduring support and knowledgeable advice over the past half decade: Bruce Rosen, who has been a source of wisdom to me even before I started graduate school, and whose kind leadership have made the Martinos Center a home away from home throughout my training; Collin Stultz, for patiently guiding me through many challenging milestones, and for making me a more rigorous researcher in cardiology; Jayashree Kalpathy-Cramer, whose expertise, passion, and excitement about deep learning and medical imaging made every discussion as consequential to my research as it was fun.

I also want to thank all the people whose expertise in cardiac imaging made this work possible. I owe a great debt of gratitude to my friend and colleague David Izquierdo-Garcia, whose valuable advice pointed me in this research direction. This work would not be nearly as complete without the assistance of our Groningen collaborators, Niek Prakken and Gert Jan Snel. My sincerest gratitude to David Sosnovik, Chris Nguyen, and Maaike van den Boomen for offering their invaluable support over many years.

Many thanks to the members of the Martinos Center family: to my desk mate Michael Levine for all the fun conversations we had over the years; to Christin Sander, for all the advice and for being a source of inspiration; to Grae Arabasz, for offering his scanning know-how, logistical, and technical support; and to Donna Crowe, for

playing a key role in the success of many graduate students in the center.

My deepest gratitude to my friends and classmates, Ang Cui and John Samuelsson, who I greatly admire and respect. Our 24 hour pset marathon, practice presentations, and just plain having fun, are some of my most cherished memories at MIT.

None of this work would have been possible without my mother, Maria, whose own journey paved the road for mine. Words cannot describe how incredibly proud I feel of being her son.

To my best friend, confidant, and wife, Paola. Thank you for making our lives more colorful, for making me a kinder person, and for pushing me to become the best version of myself. I love you.

Contents

List of Figures

List of Tables

Chapter 1

Introduction

1.1 Cardiac Disease in the Twenty-First Century

Twentieth century advances in prevention, diagnostics, and treatment of cardiovascular disease resulted in a dramatic reduction in cardiovascular-related mortality during the second half of the century, which at the beginning was steadily rising from 21% of all deaths in 1933 to 39% of all deaths in 1963 in the United States. These advances were instrumental for the reversal of this trend, and by the year 2000 overall mortality rate had declined by 62% [31]. This downward trend initially continued into the twenty-first century but has remained stagnant since 2012 [117], and rapidly increasing prevalence of cardiovascular disease and heart failure have emerged as new alarming trends [49].

Cardiovascular disease is currently the leading cause of death in the United States [8], and its prevalence is projected to grow from 37% to 41% during the 2010-2030 time period. Similarly, heart failure prevalence is projected to grow from 2.8% to 3.5%, reflecting a 25% rise over the same time period [49]. Further, worrisome studies suggest cardiovascular disease prevalence and morality rates in young adults are increasing, which could also exacerbate the future burden of heart failure as this population segment ages [39, 36].

Several factors have emerged as the main drivers of these trends, including ageing of the post-war baby-boom generation that is now reaching the age at which

risk of heart failure increases [17]. Another factor is the higher survival rate among patients after acute coronary events, since adverse myocardial remodeling following these events is the most common cause of heart failure [34]. Worldwide shifts towards sedentary lifestyles and suboptimal diets are major factors as well, since these shifts have lead to an increase of obesity and diabetes in the population. Both obesity and diabetes are strong independent risk factors for increased cardiovascular morbidity and mortality, and are suspected to contribute to increased incidence of heart failure in the young [39]. In the modern era, these risks factors represent significant challenges in cardiovascular medicine, since both conditions are potentially the largest epidemics of the twenty-first century [164, 131, 48].

Prevention and management of obesity and diabetes, as well as other other cardiovascular risk factors such as hypertension, could be effective strategies in the prevention of cardiac disease. More generally, advances in prevention are expected to play a significant role in re-establishing downward trends in cardiovascular disease prevalence and mortality in the future. Nevertheless, it has become evident that twentieth century measures of cardiac function are increasingly limited in the modern era, especially relating to earlier recognition of cardiac dysfunction.

1.2 Evaluating Cardiac Mechanics in The Modern Era

The cardiac cycle is essentially a repeating pattern of contraction and relaxation of the heart, consisting of a *systolic* (i.e., contracting) and a *diastolic* (i.e., relaxing) phase. Cardiac mechanics are determined by the precise interplay between myocardial contractility, architecture, and loading conditions during the cardiac cycle. Preload is related to the stretch of the myocardial fibers before contraction. Afterload is related to the load against which the ventricle contracts. A brief summary of the cardiac cycle is provided below. For a more comprehensive description we recommend the book *Pathophysiology of Heart Disease* by Leonard S. Lilly [75]

The contracting phase normally lasts 0.3s, and the relaxing phase lasts 0.5s. This cycle begins and ends when the *left-ventricular* myocardium is fully relaxed, otherwise known as *end-diastole* (Fig. 1-1). The volume of the left-ventricular cavity at this point is known as the end-diastolic volume. Contraction of the ventricle at the onset of systole forces the closure of the mitral valve, the opening of the aortic valve, and ultimately the *ejection* of blood from the left ventricle to the body. The conclusion of the ventricular ejection, signaling the end of the contracting phase, is known as *end-systole*. At this point, the aortic valve closes, starting the process of left-ventricular isovolumetric relaxation. When the mitral valve re-opens, due to a differential pressure gradient between the left atrium and ventricular cavity, blood oxygenated by the lungs flows passively yet rapidly through the mitral valve into the left-ventricular cavity. Seventy percent of the left-ventricular cavity re-filling occurs during this passive filling stage, otherwise known as *early-diastole*. In late-diastole, contraction of the left atrium propels a final bolus of blood into the ventricle. This contraction contributes 20%–30% of total left-ventricular cavity filling volume. Finally, filling of the ventricle ends at end-diastole, and contraction of the ventricle begins a new cycle.

1.2.1 Diastolic Dysfunction

In normal subjects, myocardial isovolumetric relaxation and suction should precede atrial filling, therefore it should be relatively load independent. However, several diseases such as hypertrophic cardiomyopathy, myocardial fibrosis and ischemic disease can result in altered relaxation (Fig. 1-2). In these diseases, myocardial diastolic function and motion reflect movement that is secondary to atrial filling, i.e., the ventricle is actively pushed by incoming blood. In stage I diastolic dysfunction, this impaired relaxation results in increased reliance on the left atrium kick to fill the ventricle. Other stages include pseudonormal and irreversible impaired relaxation. In any case, measures of the isovolumetric relaxation rate of the heart during the early-diastolic phase are good indicators of diastolic dysfunction.

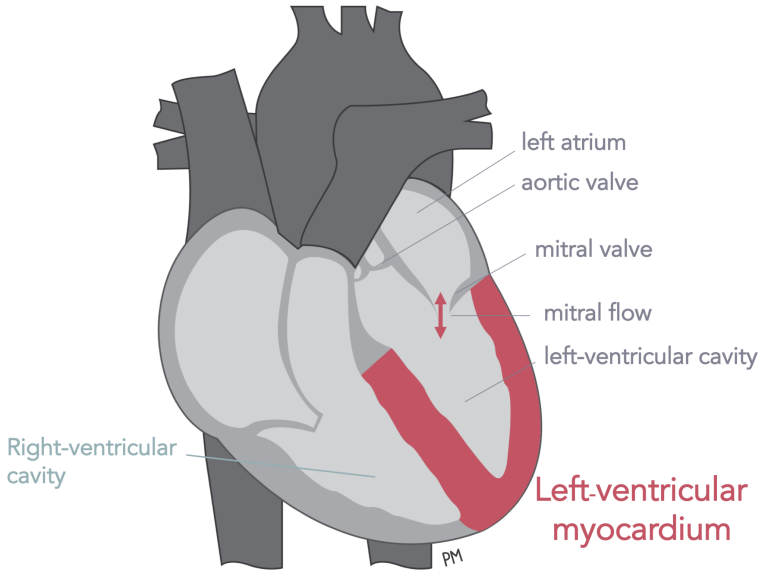

Figure 1-1: Human heart anatomy. Highlighted in red is the left-ventricular myocardium. Double arrow indicates blood in-flow and out-flow across the mitral valve.

1.2.2 Systolic Dysfunction

Several conditions affecting myocardial contractility can result in systolic dysfunction, such as coronary artery disease, chronic volume overload, and dilated cardiomyopathies. Hypertension can also lead to systolic dysfunction by increasing the afterload. *Ejection fraction* is the usual index of left-ventricular systolic function, defined as

$$\text{Ejection Fraction } (\%) = \frac{\text{End-diastolic Volume} - \text{End-Systolic Volume}}{\text{End-diastolic Volume}} \tag{1.1}$$

A low ejection fraction may be due to a decrease in the numerator term in (1.1), or due to an increase in end-diastolic volume, therefore it may not always provide an appropriate description of systolic function. In addition, mechanical impairment and even heart failure may occur without changes in this measure. In some ways, the ejection fraction is an oversimplification of the complex heart failure syndrome, and several calls to action have been made by the clinical community about the need for

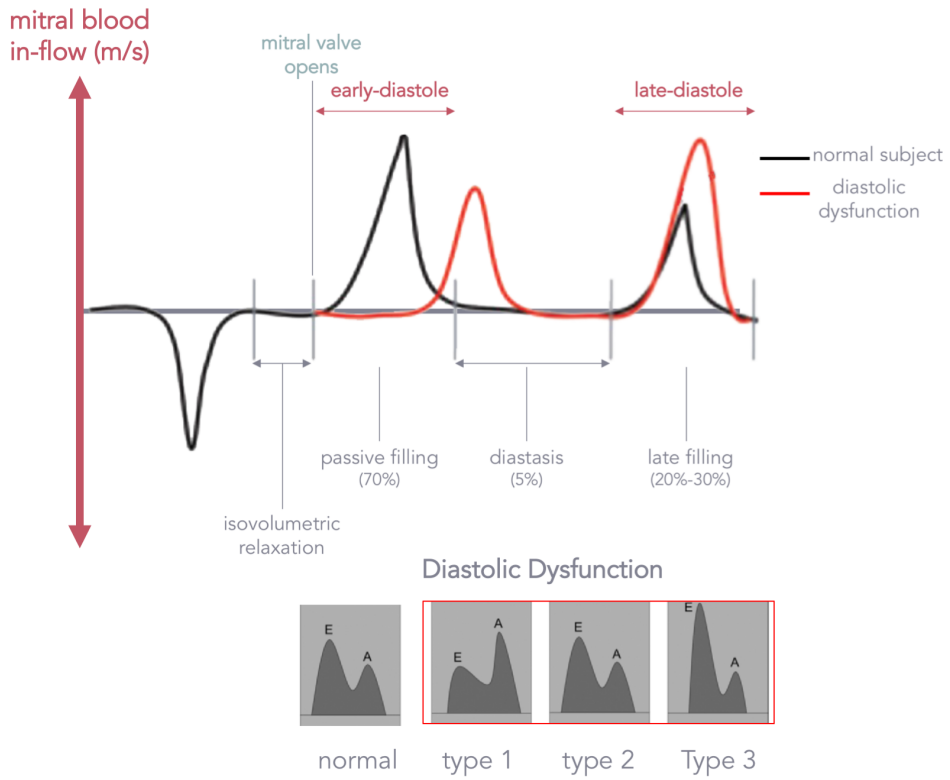

Figure 1-2: Mitral valve blood-inflow.

more sophisticated measures of cardiac mechanics [67, 88, 136]. This is particularly important in the modern era where the majority of new cases of heart failure occur in the setting of preserved ejection fraction, which already accounts for more than 50% of all cases. More alarmingly, the specific pathological processes that result in heart failure in both the elderly, obese, and diabetic populations in many cases occur without changes in the ejection fraction, which complicates diagnosis and treatments in these populations [136].

1.3 Technologies to Characterize Cardiac Mechanics

1.3.1 Morphological, functional, and strain measures

Morphological and functional measures

Standard morphological measures of cardiac mechanics include the end-diastolic and end-systolic cavity volumes, and the left-ventricular mass. Using the ventricular cavity volumes, measures of systolic function such as the ejection fraction can be evaluated using (1.1). Metrics of diastolic function can also be assessed with tissue Doppler imaging by measuring the mitral blood in-flow (Figures 1-1 and 1-2), including the peak filling rate during the early-diastolic phase (i.e., E peak), and the peak filling rate during the late-diastolic phase (i.e., A peak). The E/A ratio is a common indication of diastolic dysfunction.

Strain measures

Motion tracking techniques for strain analysis provide a more thorough characterization of left-ventricular mechanics through non-invasive evaluation of myocardial deformation along multiple directions (Fig. 1-3). These techniques could be based on echocardiography and cardiac magnetic resonance (MR) imaging data (Fig. 1-4), and could be used to identify systolic dysfunction before ejection fraction is reduced. In addition, although it is traditionally held that diastolic dysfunction precedes systolic dysfunction, recent work suggested that asymptomatic systolic dysfunction detected by strain may instead be the first sign of diabetic heart disease [27]. Furthermore, strain imaging studies in patients with type 2 diabetes mellitus have shown that asymptotic systolic dysfunction is associated with adverse long-term prognosis, and provides incremental prognostic value to diastolic dysfunction. [52, 80, 98]. Thus, strain characterization of the cardiac mechanics could give a more complete picture of the underlying biomechanical status of the left ventricle, complementary to the usual measures of morphology and function.

Strain is defined as percent change in myocardial fiber length per unit length (Fig.

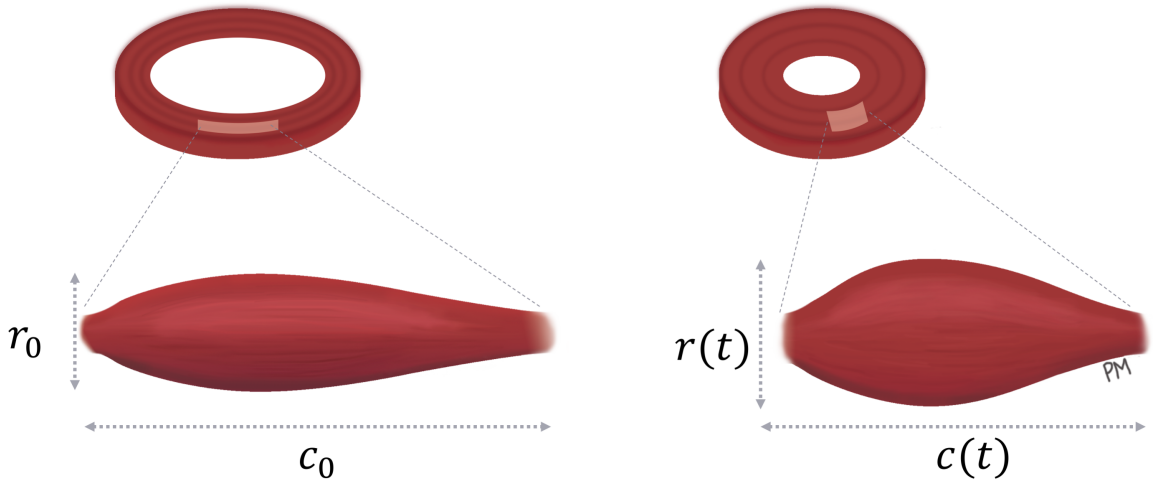

Figure 1-3: Deformation of myocardial fibers. The end-diastolic phase is shown on the left. End-systolic phase is shown on the right.

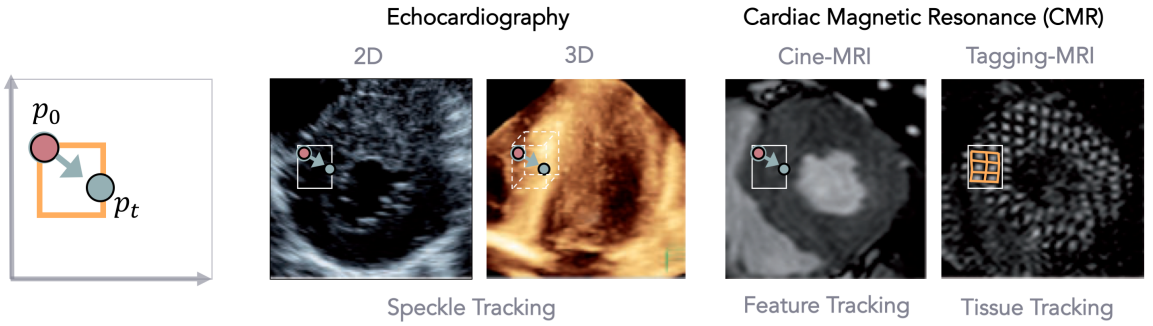

Figure 1-4: Motion tracking techniques

1-3). During contraction of the myocardium, shortening of circumferential fibers $c(t)$ from a relaxed length c_0 results in a normally negative circumferential strain ϵ_c. Lengthening of radial and longitudinal fibers leads to positive radial strain ϵ_r and longitudinal strain ϵ_l. The time derivative $d\epsilon/dt$ is known as the strain rate.

$$\begin{aligned} \epsilon_r(t) &= \frac{r(t) - r_0}{r_0} > 0 \\ \epsilon_c(t) &= \frac{c(t) - c_0}{c_0} < 0 \\ \epsilon_l(t) &= \frac{l(t) - l_0}{l_0} > 0 \end{aligned} \tag{1.2}$$

Once strain and strain rate have been measured for the entire cardiac cycle, different

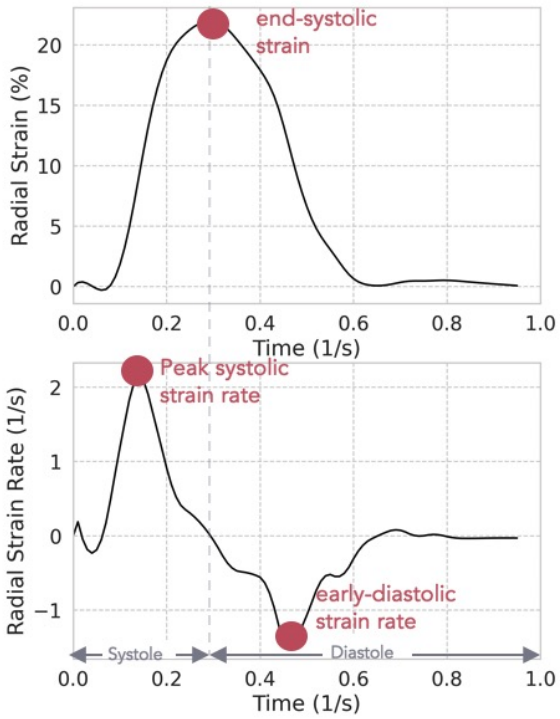

Figure 1-5: Global measures of myocardial strain.

parameters can be extracted (Fig. 1-5). These parameters can be based on timing and magnitude: end-systolic strain is defined as the global strain value at end-systole and is the recommended default parameter for the description of myocardial deformation [143]; systolic strain rate is defined as the peak (i.e., maximum) absolute value of global strain rate during systole and is an index of contractility [37]; early-diastolic strain rate is defined as the peak absolute value of global strain rate during diastole and is a marker of diastolic dysfunction [62].

1.3.2 Cardiac magnetic resonance

Echocardiography is commonly the first-line imaging modality used to assess cardiac function, yet these data remain limited for strain mapping tasks by their low reproducibility of acquisition planes [3] and temporal stability of tracking patterns [143]. In non-diagnostic or cases with inconclusive echocardiography findings, cardiac MR imaging plays an important complementary role and is often requested [108] to provide the most accurate and reproducible assessment of cardiac function, structure,

and tissue properties [120]. This thesis thus focuses on the most advanced methods for motion tracking, i.e., tagging and cine MR.

Tagging

Tagging MR alters the magnetization the myocardial tissue in a specific geometric pattern. Regions with altered magnetization appear as dark lines in the images. Because the magnetization is a property of the tissue, the tag lines move along with the tissue in which they are created, deforming during contraction. In other words, tagging MR establishes an intrinsic grid in the myocardial tissue that deforms according to myocardial motion. Deformation of grid lines across the myocardial form the ideal condition for motion tracking (Fig. 1-6).

Tissue tracking of tagging images has been widely accepted as the reference standard imaging modality for strain quantification with extensive validation *in vitro*[155] and *in vivo*[33, 154, 154, 77, 134, 81, 90]. However, tagging images have low temporal resolution which could result in inaccurate measures of strain rate. Furthermore, tagging requires dedicated acquisition sequences and time-consuming post-processing steps using specific software tools not widely available. Therefore, tagging has mainly remained a research tool.

Cine

In contrast to tagging, cine techniques apply a homogeneous magnetic field across the entire field-of-view. As a consequence, the tissue intensity within the myocardium is relatively uniform, lacking any obvious patters to facilitate motion tracking. This is not necessarily a limitation of cine acquisitions. On the contrary, acquisition and processing of these images is fast and straightforward, and therefore they are ubiquitously acquired and used in clinical practice to evaluate morphological and functional measures. Despite these strengths, motion tracking from cine data is quite challenging. In addition to the homogeneous tissue intensity, the anisotropic resolution of cine data further complicates estimation of three-dimensional motion. A typical cine dataset has 1.5 mm resolution in the x-y-plane and between 5-10 mm along the z

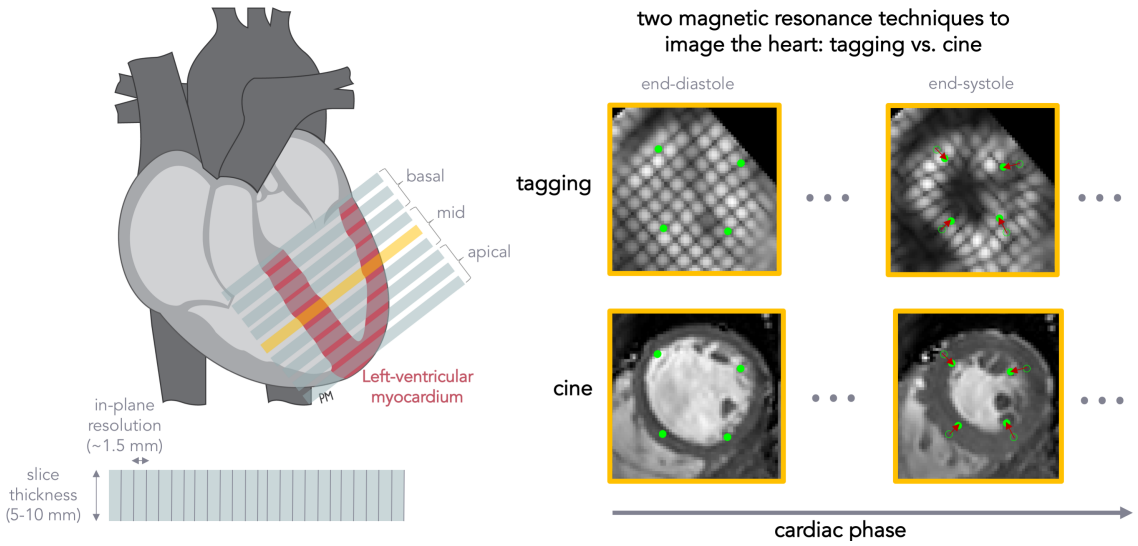

Figure 1-6: Magnetic resonance imaging of the myocardium across a mid-ventricular plane. The tagging sequence is shown on top, and cine is shown at bottom. From left to right, each plane acquisition collects data across one complete cardiac cycle.

direction (Fig. 1-6).

1.4 Technical Challenges in Characterization of Cardiac Mechanics

Irrespective of modality or algorithm, accurate and precise cardiac motion tracking is a very challenging task with multiple sources of discrepancies that have limited its wide clinical adoption [3]. Operator-related discrepancies are introduced when the myocardial wall borders are delineated manually, a time-consuming process that requires considerable expertise and results in significant inter- and intra-observer variability [124]. Automatic delineation approaches have been implemented within computational pipelines [148], but other factors related to the motion tracking algorithms itself can also influence strain assessment, including the appropriate selection of tuneable parameters whose optimal values can differ between patient cohorts and acquisition protocols (e.g., the size of the search region in block-matching methods [105]). Further, these algorithms often make assumptions about the properties of the myocardial tissue (e.g., incompressible and elastic [18, 86]), or use registration methods

to drive the solution towards an expected geometry. However, recent evidence has shown the validity of these assumptions varies between healthy and diseased myocardium [70], suggesting these approaches may not accurately reflect the underlying biomechanical motion. Modality-related image quality could also complicate interpretation of abnormal strain values since these could reflect either real dysfunction or artifact-related inaccuracies, leading to some degree of subjectivity or non-conclusive results. Lastly, although automated segmentation and motion tracking commercial software is available for cine MR, manual correction of delineated contours used for tracking is often required, resulting in significant variations in strain depending on segmentation method and type of commercial software [76].

In an excellent review article on the various sources of discrepancies in strain analysis, Amzulescu *et al* [3]. highlighted that reported normal (i.e., healthy) ranges of strain vary largely between the different motion tracking modalities and algorithms, albeit to a lesser extend for tagging methods (Fig. 1-7). These wide ranges may be explained by patient-related factors (i.e., age, gender, and ethnicity) and haemodynamic factors (heart rate and blood pressure), but more likely reflect a lack of precision in existing technology due to the technical factors described above. Addressing these technical sources of variations is crucial for wide clinical adoption since application of myocardial strain to quantify deformation in pathological states requires the accurate and precise definition of normal strain.

In this dissertation we describe a novel myocardial strain analysis workflow with specific technical and practical attributes that aims to address most of these sources of discrepancies. For operator-related factors, we propose a method that is scanner to radiology-report fully-automatic. This approach has the added advantage that, in addition to strain, other morphological and functional parameters such as left-ventricular mass, end-diastolic and end-systolic volumes, and ejection fraction can also be automatically evaluated. For motion algorithm factors, our method is data-driven and does not make assumptions about the underlying physiology, and is parameter-free at inference. Finally, we show that our method is robust to various kinds of modality-related image artifacts.

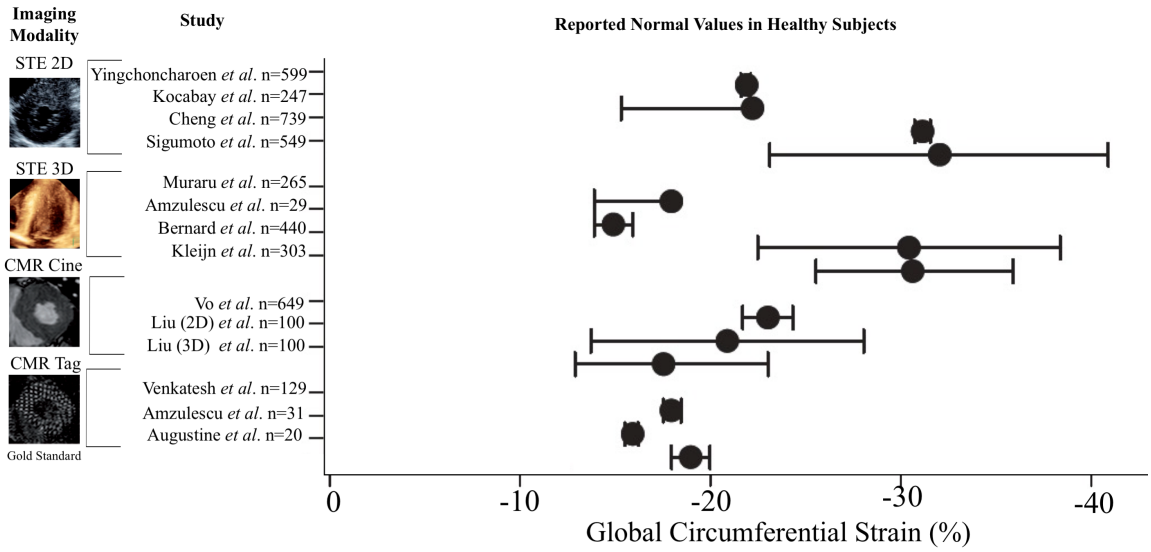

Figure 1-7: Reported normal (mean and 95% confidence interval) global circumferential strain in healthy subjects for different imaging modalities and methods. Adapted from Amzulescu *et al.* [3].

1.5 Role of Deep Learning in cardiac MR

Deep learning methods refer to machine learning, a branch of artificial intelligence, using multiple layers of adjustable computing elements that, over the last decade, have achieved remarkable success in several tasks, starting with speech and visual recognition. The success of deep learning and the pace at which ever more complex models are developed relies is part on equally remarkable powerful graphic processing units. Since 2012, the amount of computations on these graphic processing units used by the largest deep learning models has been increasing exponentially, growing by more than 300,000x from AlexNet to AlaphaGoZero (Fig. 1-8a). The availability of vast amounts of data has also been crucial in the success of deep learning methods, some arguing that the improvement in performance obtained from increasing the size or quality of the data outweighs any improvement that can be obtained from tweaking the deep learning algorithm. Fortunately, digitization of various industries has resulted in expansion of the global datasphere, with the healthcare industry expected to grow faster than the rest (Fig. 1-8b). Many hospitals are heavily investing in high-performance graphic processing unit clusters in anticipation of this trend, enabling

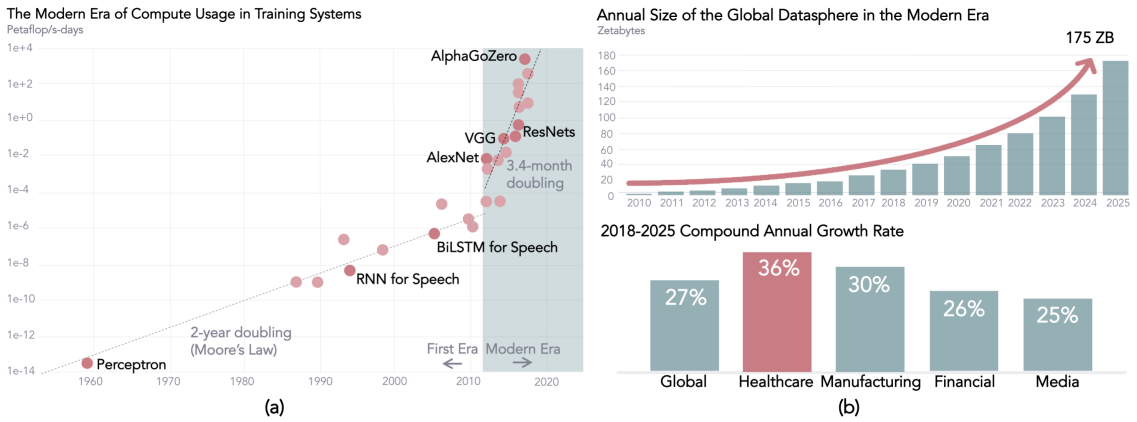

Figure 1-8: (a) Deep learning computing (a) and healthcare datasphere in the modern era.

vast amounts of local storage for data processing, faster experimentation, larger deep learning models, and ultimately more productive and significant clinical discoveries.

Cardiac MR is in many ways an ideal imaging modality for cardiovascular focused deep learning. From an *instrumentation* perspective, innovations in scanning technology are still pushing MR to new limits of magnetic strength [100]. Stronger magnets are producing higher resolution images, which means more data are stored per scan [55]. These innovations could synergize with deep learning techniques that have been successfully applied to MR image acquisition and reconstruction tasks [161, 162]. For instance, they could be used to reconstruct high-quality cardiac MR images from undersampled k-space measurements to reduce scanning time [123, 44]. They could also accelerate the reconstruction of useful but complex cardiac MR sequences that were previously clinically unfeasible due to lengthy optimization times during reconstruction [42] (Fig. 1-9a). With the advent of these technologies, more scans can be done in less time, potentially leading to higher volumes and quality of cardiac MR data. However, since these data must be carefully analyzed to quantify any evidence of disease, this growing volume and complexity of imaging data could exacerbate occupational fatigue in radiologists, potentially resulting in worse diagnostic performance [46, 133]. From a *quantification* perspective, recent deep learning models for cardiac MR have been proposed that may help shoulder the increasing workload by providing more automated workflows. These include preprocessing [122], segmentation and

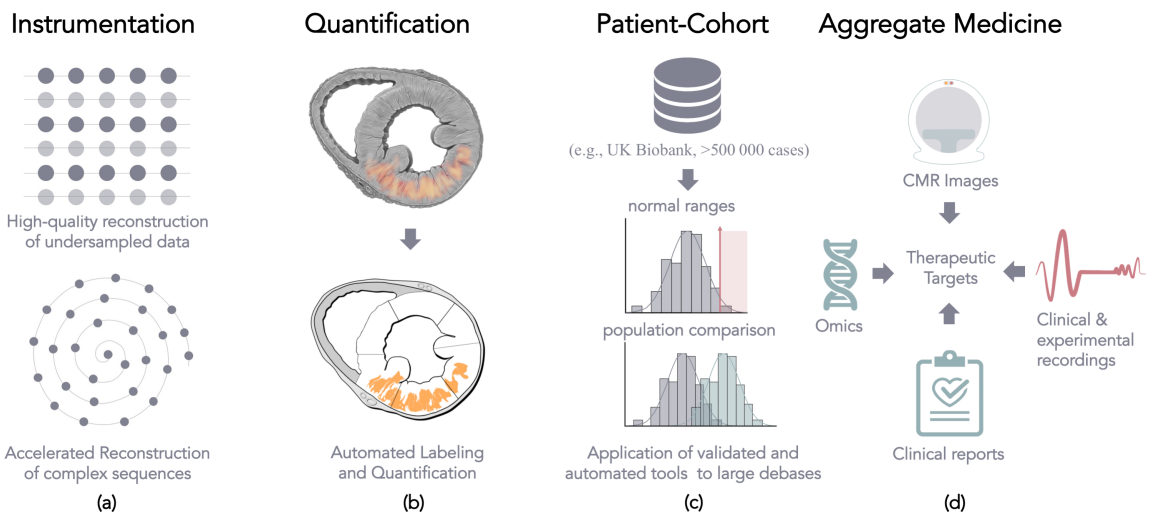

Figure 1-9: The role of deep learning in cardiac MR.

analysis of morphology and function [118], and more recently scar quantification [26] (Fig. 1-9b).

From a *patient-cohort* point of view, applications to large databases (e.g., UK Biobank, >500,000 cases) could enable quick and automatic definition of normal value ranges of various cardiac parameters (e.g., strain), or comparisons between large populations [119](Fig. 1-9c). Lastly, in *aggregate medicine* applications, a fully-automatic deep learning workflow could leverage different kinds of cardiac MR data to offer an incredibly rich set of cardiac MR imaging features describing the mechanical status of the heart. New and exciting deep learning methods could combine these cardiac MR imaging features with other clinical and genetic information to generate insightful and actionable information (Fig. 1-9d). Nevertheless, care must be taken both by clinicians and deep learning developers to avoid wrong measurements and subsequently incorrect interpretations. Therefore, the lifecycle of any deep learning workflow must include a thorough validation of each component.

1.6 Aims and Thesis Overview

The overall goal of this dissertation project was to develop a novel cardiac MR deep learning workflow to characterize the cardiac mechanics. This workflow was designed

with specific technical and practical attributes to make it available for immediate and wide research use. Validation and comprehensive assessment of the accuracy and repeatability of the workflow was also performed. In the last chapter, we also discuss how the proposed workflow could be used for several other quantitative, patient-cohort, and aggregate medicine applications.

The overall goal was split into three aims.

1.6.1 Aim 1: To develop a deep learning method capable of cardiac motion estimation using a widely-available cardiac MR sequence.

In Chapter 2 we describe a novel deep learning method for three-dimensional cardiac motion estimation trained using data from healthy and cardiovascular disease adults. The model is based on clinically-standard cine MR data and could be integrated in routine studies without modifications to the standard cardiac MR protocol. The proposed technique was evaluated on a pediatric dataset using several intensity-based and binary metrics, and the performance was compared to several state-of-the-art non-learning registration methods.

1.6.2 Aim 2: To develop and validate an automated cardiac MR workflow for clinically-feasible quantification of cardiac mechanics.

In Chapter 3 we describe the design and validation of a fully-automatic cardiac MR workflow for strain analysis using some of the techniques developed in section 1.6.1. The proposed workflow enables quantification of morphological, functional, and strain measures. Each of the workflow components was benchmarked against learning and non-learning techniques, and was validated against a reference tagging MR method. The intra-scanner repeatability of global and regional strain measures was also assessed. In this chapter we also describe global and regional applications and discuss

the potential clinical utilization of our approach. This work is the first to report within a single study the characterization, validation, and repeatability of a learning-based method for strain analysis.

1.6.3 Aim 3: Test the proposed workflow in asymptomatic subjects without known but suspected cardiac dysfunction to determine the clinical value of deep learning characterization of cardiac mechanics.

In chapter 4 the proposed technique was tested in a prospective cross-sectional study in asymptomatic young adults with a mixture of cardiovascular disease risks factors, i.e., overweight, hypertension, and type 2 diabetes mellitus. We focused on these populations because of the immediate high clinical impact, although conceivably future studies could characterize other populations.

Finally, in chapter 5 the key implications of the proposed techniques are discussed, including remaining challenges to overcome for full clinical adoption.

Chapter 2

Learning Cardiac Motion

2.1 Introduction

Characterizing the motion of the heart using noninvasive imaging techniques such as cardiac MR is challenging but potentially very important. On the technical side, this information could be used to improve the quality of the cardiac MR data acquired by using cardiac gating techniques [9], or to minimize the unwanted effects of motion on the positron emission tomography (PET) data acquired simultaneously in integrated PET-MR scanners [65]. From a more clinical perspective, detailed knowledge of the complex three-dimensional motion of the heart during the cardiac cycle (e.g., myocardial strain) would inform us about its mechanical status, with potential diagnostic implications [129]

Ideally, the motion estimates should be obtained from cardiac MR sequences such as cine that are routinely used for clinical purposes. This breath-hold sequence allows the acquisition of data corresponding to each specific time point in the cardiac cycle (i.e., systole, diastole). Characterizing the three-dimensional motion of the whole heart across time from these images is challenging because the tissue intensity is relatively homogeneous and morphological details to facilitate the temporal correspondence search are limited. Furthermore, because a cine volume in a time frame is technically a two-dimensional stack of independently acquired sections, rather than an actual three-dimensional volume where the whole heart is simultane-

ously acquired, out-of-plane motion during the cardiac cycle makes the derivation of three-dimensional estimates challenging.

Deep learning methods have demonstrated the advantage of allowing real-world data guide learning of abstract representations that can be used to accomplish pre-specified tasks, and have been shown to be more robust to image artifacts than non-learning techniques for some applications [163, 23]. Promising learning methods for cardiac motion estimation from cine MR data have been proposed [110, 112, 111, 156]. These learning methods usually consist of an intensity-based loss function and a constrain term [112, 20], the latter using common machine learning techniques (e.g., L2 regularization of all learnable parameters) or direct regularization of the motion estimates (e.g., smoothness penalty [112], anatomy-aware [15]). However, only two-dimensional formulations have been proposed to-date, and motion predicted using these approaches could be influenced by out-of-plane motion during the cardiac cycle, resulting in overestimation of in-plane motion and reduced reproducibility [78].

In this chapter we present the first unsupervised three-dimensional cardiac motion estimation network (CarMEN) for deformable motion modeling from cine MR data. Although we used the method to register cardiac cine MR images here, CarMEN is in principle broadly applicable to other cardiac image registration tasks.

Our aims were to train and test CarMEN by using data from adult and pediatric participants, and to compare its accuracy to that of several popular state-of-the-art registration packages in the presence of out-of-plane three-dimensional movement, acquisition artifacts, and pathological changes. We hypothesized that CarMEN would achieve better accuracy compared to non-learning techniques.

2.2 Background

2.2.1 Mathematical Representation of Cine MR Data

Let V_t denote a grayscale cine MR frame at time t defined over an n-Dimensional (nD) domain $\Omega \subset \mathbb{R}^n$, and let $v \in \Omega$. Similarly, let M_t denote the corresponding

labeled frame at time t defined over an nD domain $\Omega^K \subset \mathbb{N}_0$, and let $v^k \in \Omega^K$ denote all $v \in \Omega$ with label k.

When $n = 2$, v is a pixel and V_t is an image at frame t. When $n = 3$, v is a voxel and V_t is a "volume", in the sense that it represents a stack of independently acquired images at frame t covering the heart from apex to base. By independently acquired we mean the collection of images across a specific ventricular section (e.g., mid-ventricle) at multiple frames covering a complete cardiac cardiac cycle (Fig. 1-6). This is in contrast to more recent free-breathing MR sequences where data from the whole heart can be acquired simultaneously [139].

In standard image registration formulation, a *moving* frame $V_t : \mathbb{R}^n \rightarrow \mathbb{R}$ is registered onto a *fixed* reference frame $V_{t=0} : \mathbb{R}^n \rightarrow \mathbb{R}$, yielding the transformation $u_t : \mathbb{R}^n \rightarrow \mathbb{R}^n$. For cardiac motion estimation, u_t denotes the myocardial displacement from a fully-relaxed end-diastolic phase at $t = 0$, to a contracted phase at $t > 0$. Formally, for each $v \in \Omega$, $u_t(v)$ is an approximation of the myocardial displacement during contraction such that $V_{t=0}(v)$ and $(u_t \circ V_t)(v)$ correspond to similar cardiac regions. The operator $\circ$ refers to application of a spatial transform to V_t using u_t via bilinear (for $n = 2$) or trilinear (for $n = 3$) interpolation to approximate $V_{t=0}$.

Most existing non-learning registration algorithms iteratively estimate u_t by solving

$$\hat{u}_t = \arg\min_{u_t} \mathcal{L}_{intensity}(V_{t=0}, u_t \circ V_t) + \lambda_s \mathcal{L}_{smoothness}(u_t), \tag{2.1}$$

where $\mathcal{L}_{intensity}$ is an intensity-based term that measures the image dissimilarity between $V_{t=0}$ and $u_t \circ V_t$, the regularization term $\mathcal{L}_{smoothness}$ enforces smoothness in u_t, and λ_s is the regularization parameter. In this study, we reformulate this optimization as a learning task by modeling a function $g(V_{t=0}, V_t) = u_t$ as a convolutional neural network (section 2.3.1), and by recasting the terms in (2.1) as differentiable loss functions (section 2.3.2).

2.2.2 Convolutional Neural Network for Motion Estimation

The function $g(V_{t=0}, V_t) = u_t$ could be modeled using two potential convolutional neural network formulations. The first uses two separate, yet identical encoders for the two frames to combine them at a later stage as shown in Fig. 2-1b. With this formulation the network is constrained to first produce meaningful representations of the two frames separately and then combine them on a higher level. This roughly resembles the standard matching approach when one first extracts features from patches of both images and then compares those feature vectors. A decoder is then used to estimate the motion from the combined representation. One potential benefit of this approach for cardiac imaging is that it enables joint optimization of segmentation and motion estimation tasks [113]. However, studies in computer vision have shown that this formulation tends to generalize poorly to variations in motion, and has difficulty with large displacements [30]. An alternative formulation is to concatenate both input frames together and feed them through a single encoder-decoder pipeline, allowing the network to decide itself how to process the pair to extract the motion information (Fig. 2-1c). This formulation has been shown to generalize better to different datasets and motions relative to the separate encoder approach [30].

Throughout this dissertation, we refer to CarMEN as an encoding-decoding network that uses the single encoder formulation with concatenated inputs [30]. In section 2.3.1 we describe the first three-dimensional CarMEN implementation specific to cine MR data, and in section 3.3.1 we improve upon this original design by leveraging simulated data and weak labels of the myocardium using a segmentation network.

2.3 Method

2.3.1 CarMEN for Multiresolution Motion Estimation

The input to CarMEN was the pair V_t, $V_{t=0}$ concatenated into a two-channel volume. This volume was passed through several encoding and decoding layers to derive a

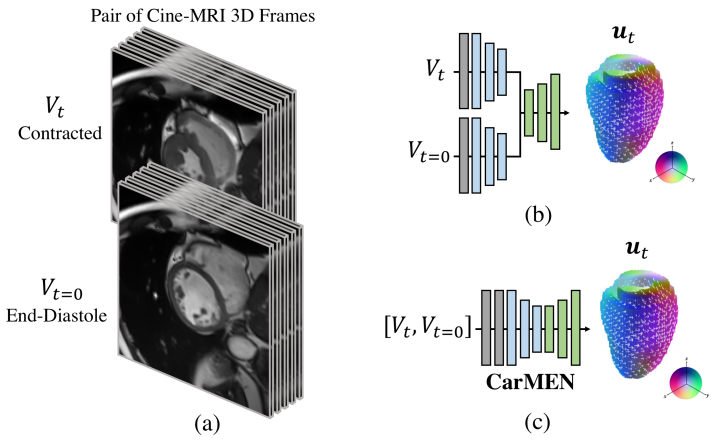

Figure 2-1: Motion estimation from cine MR frames using convolutional networks.

three-channel volume u_t at multiple resolutions, each channel representing the x, y, z components of motion. Specifically, the decoding layers generate coarse predictions $u_{t,j}$, each representing u_t downsampled by 2^j (Fig. 2-2). The encoder has eight convolutional layers with stride of two in three of them and a leaky rectified linear unit after each layer. Convolutional filter sizes were $3 \times 3 \times 3$ for all layers. The number of feature maps increased in the deeper layers, roughly doubling every second layer with a stride of two. The decoder has four upconvolutional layers consisting of unpooling followed by convolution. We applied the upconvolution to feature maps and concatenated it with corresponding feature maps from the contractive part of the network and an upsampled coarse motion prediction. Each step increases the resolution twice, and a convolutional filter of $3 \times 3 \times 3$ was used to generate a coarse prediction $u_{t,j}$ at each layer, where $j = 4, \ldots, 0$. Thus, the resolution of the estimates $u_{t,0}$ of the final layer is equal to that of the input.

2.3.2 Loss Functions for Unsupervised Learning of Motion

The intensity and smoothness terms in 2.1 were implemented as the mean absolute difference loss function

$$\mathcal{L}_{intensity} := \mathcal{L}_{MAE}(V_{t=0}, u_t \circ V_t) = \frac{1}{|\Omega|} \sum_{v \in \Omega} \left| V_{t=0}(v) - (u_t \circ V_t)(v) \right|, \qquad (2.2)$$

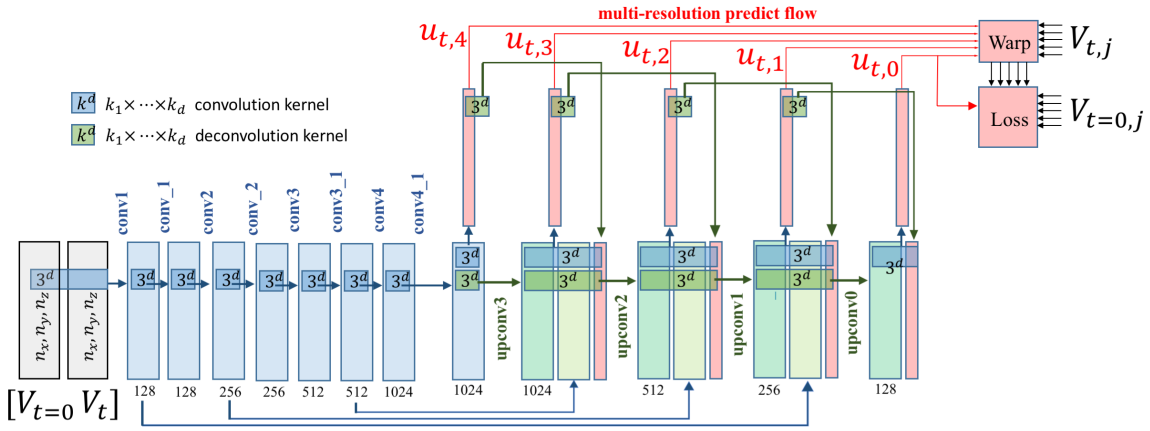

Figure 2-2: CarMEN architecture for multiresolution motion estimation

and a diffusion regularizer

$$\mathcal{L}_{smoothness} := \mathcal{L}_{\nabla}(u_t) = \sum_{v \in \Omega} \|\nabla u_t(v)\|^2 \tag{2.3}$$

The gradient operator ∇ was approximated using differences between neighboring voxels. These loss terms were evaluated for each output $u_{t,j}$, an approach akin to a multiresolution pyramid strategy used in conventional optimization techniques to improve the capture range and robustness of the registration [74]. Thus, the loss function used to train CarMEN was

$$L = \sum_{j=0}^{4} \mathcal{L}_{MAE}(V_{t=0,j}, u_{t,j} \circ V_{t,j}) + \lambda_s \mathcal{L}_{\nabla}(u_{t,j}) \tag{2.4}$$

2.4 Experiments

2.4.1 Datasets

In this study, the Automated Cardiac Diagnosis Challenge Dataset (ACDC) was used for development, and a pediatric dataset was used for evaluation. Both datasets were publicly available.

Automated Cardiac Diagnosis Challenge Dataset

The ACDC dataset consists of cine MR data from 150 subjects acquired at the University Hospital of Dijon, France [10]. The datasets were acquired with two MR scanners of different magnetic strengths (1.5 T - Manetom Aera, and 3.0 T - Magnetom Trio TIM, Siemens Medical Solutions, Germany). The subjects were evenly divided into five groups: healthy and patients with hypertrophic cardiomyopathy, abnormal right ventricle, myocardial infarction with reduced left-ventricular ejection fraction, and dilated cardiomyopathy. These data were available as *train* (n=100) and *test* (n=50) sets, with manual segmentations of the left and right ventricular cavities and left-ventricular myocardium included for the train set only (Fig. 2-3). Manual segmentations and group classification of the test set were privately held by the challenge organizers for evaluation and ranking of segmentation and diagnoses challenges.

Pediatric Dataset

The pediatric dataset consists of cine MR data from 33 subjects (aged 2-17 years) acquired at the Department of Diagnostic Imaging of the Hospital for Sick Children in Toronto, Canada [4]. The datasets were acquired with a GE Genesis Signa MR scanner (GE Healthcare, Milwaukee, Wisconsin, USA). Most of the subjects displayed a variety of heart abnormalities such as cardiomyopathy, aortic regurgitation, enlarged ventricles, and ischemia. A smaller number displayed left ventricle related abnormalities, and two subjects had normal cardiac anatomy and function. This dataset is unique in the sense that it includes manual segmentations of the left-ventricular cavity and myocardium for all cardiac phases in subjects with a wide range of heart abnormalities, providing us with a realistic and challenging performance benchmark for evaluation (Fig. 2-4).

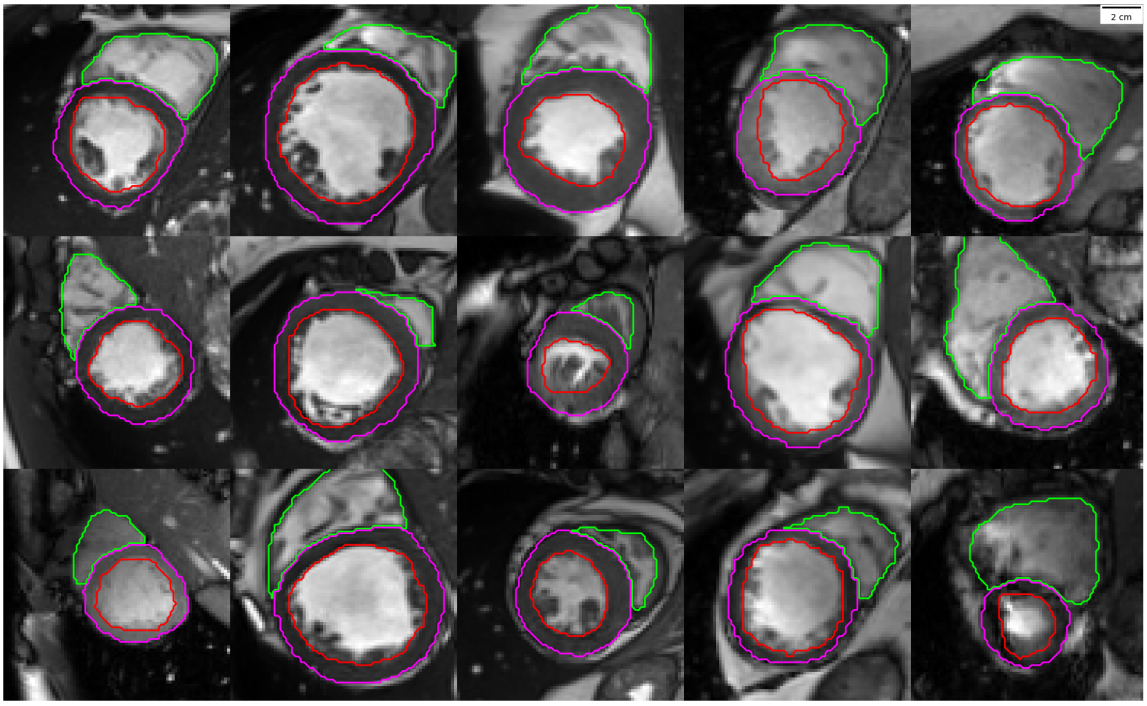

Figure 2-3: ACDC Dataset. Representative cine MR end-diastolic images at mid-ventricle for three subjects from the train set with manually delineated contours of the right-ventricular cavity (green), and left-ventricular cavity (red) and myocardium (magenta). Left to right: healthy, dilated and hypertrophic cardiomyopathy, myocardial infarction, and abnormal right ventricle.

Preprocessing

Only the ACDC train set and pediatric datasets were used for training and evaluation, accordingly. The ACDC test set was not used in this study but it was used in chapter 4. All cine MR frames and corresponding manual segmentations were resampled to a 256×256×16 volume grid with 1.5 mm×1.5 mm in-plane resolution and variable slice thickness (4-7 mm). Each frame was subsequently manually centered and cropped to 80×80×16 using the manual segmentations as reference. This step was required to fit the three-dimensional frames into the memory of the graphic processing unit.

2.4.2 CarMEN Implementation

We used TensorFlow (version 1.6; Google, Mountain View, Calif) to implement and train CarMEN. For training, a sample was defined as the pair $(V_{t=0}, V_t)$; therefore,

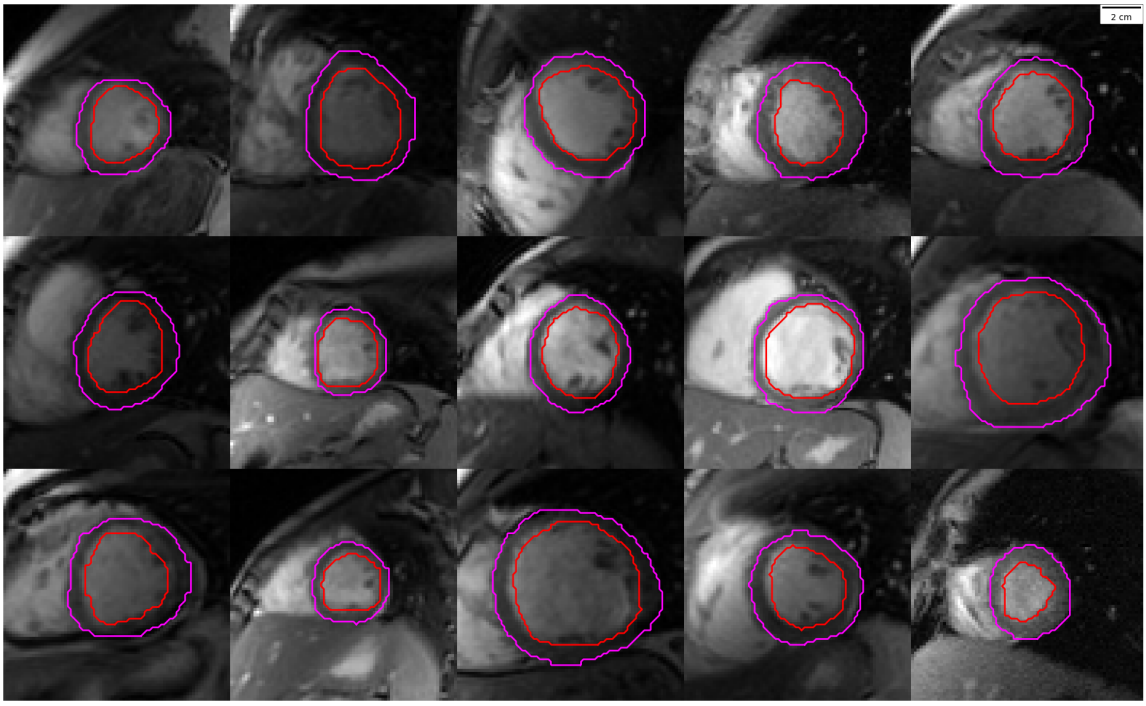

Figure 2-4: Pediatric dataset. Representative cine MR end-diastolic images at mid-ventricle with manually delineated contours of the left-ventricular cavity (red) and myocardium (magenta).

for a subject with T frames, we had a total of T samples available for training:

$$\{(V_{t=0}, V_t)\}_{\{t=0,1,\ldots,T\}}$$

We trained CarMEN with 2,512 samples from 100 subjects (ACDC train set) using minibatches of 10 pairs. Data augmentation included random z-axis rotations and x, y translations. A step decay learning rate schedule initialized at 1×10^{-4} and reduced by half every 10 epochs was used. The regularization parameter λ_s was set to 1×10^{-7}. CarMEN was trained for 100 epochs, each corresponding to one complete pass through the 2,512 samples. To reduce overfitting to one particular anatomy or frame property, the 2,512 samples were randomized at the beginning of each epoch (i.e, each batch was made up of different subjects and different cardiac phases). The training time was 4 hours and motion estimates at inference were generated in 9 seconds. A 12 GB graphic processing unit from Nvidia was used to train the models.

2.4.3 Evaluation Metrics

CarMEN was evaluated on the pediatric dataset with 627 samples from 33 subjects. Pairs $(V_{t=0}, V_t)$ $\forall t > 0$ were included in the evaluation. The accuracy of the motion estimates was assessed indirectly by evaluating $\mathcal{L}_{intensity}(V_{t=0}, u_t \circ V_t)$ using multiple functions for $\mathcal{L}_{intensity}$. Although some of the most common functions such as peak signal-to-noise ratio are used because they are fast and easy to implement, these correlate poorly with registration quality as perceived by a human observer [157]. Thus, we also evaluated our method by using the multiscale structural similarity index metric, a state-of-the-art metric that accounts for changes in local structure and correlates with the sensitivity of the human visual system [159]. We also evaluated the normalized cross-correlation function because it is less sensitive to linear changes in the MR signal intensity in the compared images.

The manual segmentations included in the pediatric dataset enabled us to evaluate CarMEN using a non-intensity metric. Let $M_t, M_{t=0}$ correspond to manual segmentations of frames $V_t, V_{t=0}$, and let $u_t = g(V_t, V_{t=0})$. If the motion estimates u_t represent accurate myocardial displacements, the anatomical labels in $M_{t=0}$ and $u_t \circ M_t$ corresponding to the same anatomical structure should overlap well. The overall overlap of the left-ventricular myocardium labels was quantified by measuring the Dice Similarity Coefficient (Dice) between $M_{t=0}$ and $u_t \circ M_t$, where a Dice score of 1 indicates the myocardium labels are identical and is a proxy for the accuracy of the predicted motion. We compared the performance of CarMEN to that of five state-of-the-art non-learning methods for image registration: two B-spline approaches with the Insight Segmentation and Registration Toolkit, or ITK, package (https://www.itk.org) [83]; a B-spline Elastix variation; a mass-preserving approach termed Vampire [35]; and the Diffeomorphic Demons, or dDemons, algorithm [142].

Statistical Analysis

Data were treated as nonparametric and presented as median and interquartile range and compared by using two-sided Wilcoxon signed-rank tests. Statistical analysis

was performed in Python (version 2.7; Python Software Foundation, Wilmington, Del; https://www.python.org). A two-sided $P < .001$ was considered to indicate statistical significance. All P values reported in the next sections refer to comparisons between a non-learning registration method and CarMEN.

2.5 Results

CarMEN and Vampire showed significantly ($P<0.001$; n = 627) better performance relative to the other four state-of-the-art methods for all the metrics except Dice score (Fig. 2-5 and Table A.1). CarMEN had a significantly higher Dice score (0.77 [interquartile range: 0.72–0.81]) relative to Vampire (0.71 [0.58–0.80]), dDemons (0.74 [0.69–0.78]), and ITK B-Spline 2 (0.76 [0.71–0.80]). There was no significant difference in the Dice score between CarMEN and the other two methods. Relative to CarMEN, Vampire had a significantly higher peak signal-to-noise ratio (38.2 [32.9–40.2] vs 30.2 [27.5–33.8]), higher normalized cross-correlation (1.00 [0.99–1.0] vs 0.99 [0.98–0.99]), and higher multiscale structural similarity index metric (0.99 [0.99–1.0] vs 0.96 [0.95–0.98]). Representative images of patients with various diseases are shown in Figure 2-6. A common feature of the non-learning methods is the disappearance of the papillary muscles in the warped images, i.e., in $u_t \circ V_t$. In contrast, these structures are preserved in most of the images obtained with CarMEN. CarMEN is also more robust to acquisition artifacts, and better preserves anatomic features.

2.6 Discussion

We developed a novel deep learning method for three-dimensional cardiac motion estimation using data from healthy subjects and cardiac patients for training. Our model is based on clinically-standard data and could be integrated in routine cardiac MR studies without modifications to the standard cardiac MR protocol. The proposed technique was evaluated on a pediatric dataset using several intensity-based and binary metrics, and the performance was compared to several state-of-the-art

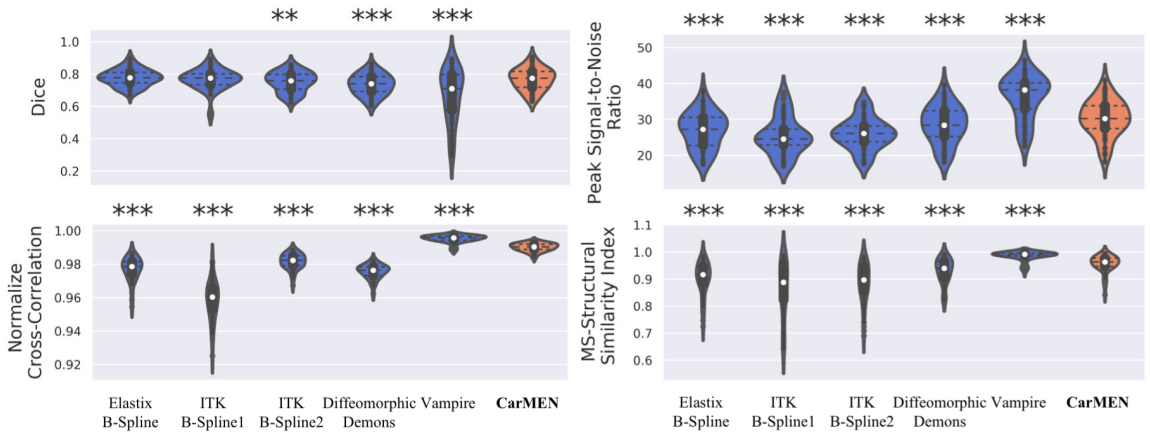

Figure 2-5: Evaluation of CarMEN using five different image similarity metrics represented with nonparametric violin plots. Violin plots are essentially mirrored density plots. Higher values for all metrics is considered good. P values are relative to CarMEN and were obtained by using two-sided Wilcoxon signed-rank tests.

non-learning registration methods. We demonstrated that the deep learning model of cardiac motion learned from one dataset was capable of generalizing to new data with better accuracy than that of non-learning techniques.

Vampire performed significantly better than CarMEN in all intensity-based metrics, which would sugggest at first glance that it is a better technique. However, Vampire had the lowest average Dice score among all methods and had several Dice scores below 0.4, indicating large errors in the estimated motion vectors. The culprit of this apparent paradox is a mass-preserving term $\det(\nabla u_t)$ used in the Vampire algorithm, which is used to replace the registration term $(u_t \circ V_t)$ with $(u_t \circ V_t) \cdot \det(\nabla u_t)$ during optimization. This term accurately modulates the intensities of the MR images, but fails when applied to integer-valued images (i.e., labeled frames). Thus, although $V_{t=0}$ and $(u_t \circ V_t) \cdot \det(\nabla)$ *look* similar, the underlying transformation u_t is inaccurate. In contrast, CarMEN had a significantly better performance relative to all other methods across all intensity-based metrics, and equal or better Dice score.

We found CarMEN to be reliable across multiple diseases and capable of preserving fine-detailed pathological features, which is essential to assess the mechanical status of the heart since these pathological features are often associated with abnormal wall motion. In contrast, most other methods were unable to handle highly abnormal

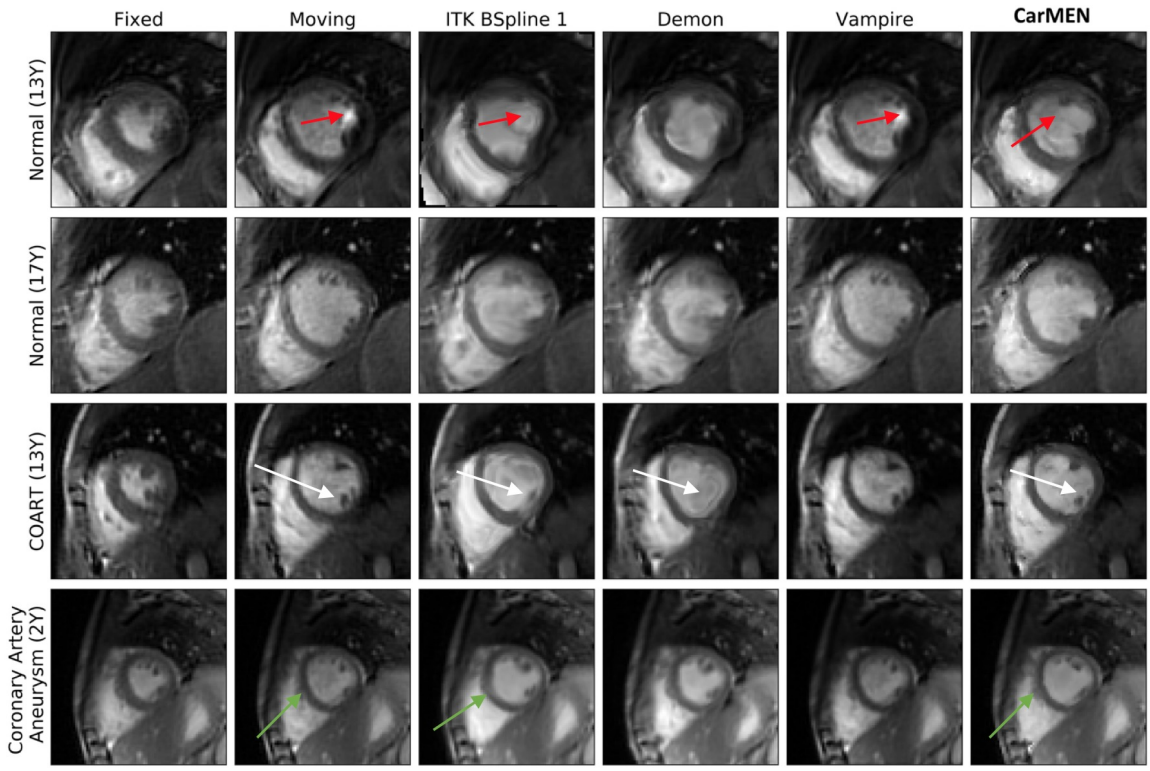

Figure 2-6: CarMEN outperforms non-learning methods across various diseases and ages. First and second columns correspond to heart at end-systole and end-diastole, accordingly. Moving image is warped to fixed position using the predicted motion. Two healthy participants and two patients are shown. CarMEN is more robust to image artifacts relative to other methods such as ITK B-Spline 1 and Vampire (black arrows). Papillary muscles disappear in some non-learning methods but are preserved by proposed method (white arrows). CarMEN does a better job at preserving anatomy relative to ITK B-Spline 1 (arrowheads). COART = coarctation of the aorta

left-ventricular anatomy. We note that compared to the training data, the pediatric dataset originated from a different institution, was acquired with a scanner from a different vendor, and came from a distinct patient population. Despite these notable challenges, our method better handled off-section three-dimensional movement as evident by the accurate mapping of papillary muscles. Furthermoe, CarMEN was more robust to acquisition artifacts, and better preserved abnormal anatomic information (i.e., it did not overfit to a healthy adult heart). Thus, these results suggest CarMEN does not memorize any particular anatomy or phase, instead learning a more general model of cardiac anatomy and motion.

2.6.1 Limitations to Address

The current implementation was only a first step towards a fully-automatic method for motion estimation since manual centering and cropping of the heart was required. In section 3.3.1 we propose a convolutional neural network to automate this step as well. We also found that indirect measures of motion estimation accuracy using registration techniques (e.g., intensity-based and binary metrics to compare transformed images) are prone to error, potentially resulting in incorrect interpretations of the results. In section 3.4.3 we evaluate the motion estimates directly using manual tracking landmarks as labels. Lastly, our method had an unfair advantage in that it was designed specifically to address challenges related to three-dimensional cardiac motion estimation, whereas the non-learning methods could be applied to general registration tasks. Thus, in the next chapter we compare CarMEN to state-of-the-art methods for cardiac motion estimation that were designed and optimized by domain experts specifically for cardiac MR data.

2.6.2 Conclusion

We have developed the first unsupervised learning–based approach for deformable three-dimensional cardiac MR image registration. We validated our approach comprehensively and demonstrated higher registration accuracy relative to several popular state-of-the-art image registration methods.

Chapter 3

Learning Myocardial Strain

3.1 Introduction

Myocardial strain analysis from cine data is an exciting and promising technique for earlier detection of asymptomatic left-ventricular dysfunction prior to reduction in ejection fraction, but several concerns have been raised regarding its robustness in wider clinical settings as described in section 1.4. Besides the imaging modality-related factors, the main technical sources of error are segmentation and motion estimation.

Deep learning segmentation methods have been proposed [128, 165, 12] and implemented within strain computational pipelines [45, 110], and we and others have shown that cardiac motion estimation can be recast as a learnable problem as well. However, none of these methods have considered the accuracy of myocardial strain as a design factor or have been applied to strain analysis, and none have been validated against reference tagging techniques. In chapter 2 we demonstrated that CarMEN produces more accurate estimates than various non-learning registration techniques. Thus, incorporating our method within a strain analysis framework could potentially enable accurate, user-independent, and quantitative characterization of cardiac mechanics both globally and regionally.

We propose DeepStrain, a fast, automated workflow that derives global and regional strain measures from cine data by decoupling the motion estimation and seg-

mentation tasks. With decoupling, segmentations are not used for motion estimation but rather to derive clinical parameters and to identify a cardiac coordinate system for strain analysis, further reducing the variability in strain directly related to segmentation. This chapter describes a carefully designed strain quantification-specific CarMEN implementation that handles challenges associated with the anisotropic resolution of cine data. Our loss weighting strategy to find the optimal balance between motion regularization terms also differs from previous methods which have traditionally relied on registration techniques as indirect measures of motion accuracy. Instead, we simulated cine data with corresponding ground-truth cardiac motion to identify the hyperparameters yielding accurate motion and strain estimates. The optimally trained configuration is available online at https://github.com/moralesq. Finally, this chapter also provides a comprehensive assessment of the accuracy and repeatability of DeepStrain measures, a task that has been mostly ignored in the deep learning literature but is critical to clinical adoption [3].

3.2 Background

3.2.1 Mathematical Representation of Myocardial Strain

Strain represents percent change in myocardial length per unit length. The 3D analog for MR is given by the Lagrange strain tensor

$$\epsilon_t = \frac{1}{2}\big(\nabla u_t + \nabla u_t^T + \nabla u_t^T + \nabla u_t\big) \tag{3.1}$$

where u_t denotes myocardial displacement as defined in section 2.2.1. Radial and circumferential strain are the diagonal components of the tensor evaluated in cylindrical coordinates. Strain rate is the time derivative of (3.1). Global strain is defined as the average of ϵ over the whole left-ventricular myocardium volume. Regional strain is defined as the average of ϵ over the volume of specific myocardium segments defined by the American Heart Association polar map. Specific parameters based on timing and magnitude are extracted from the measures evaluated over a whole cardiac cycle:

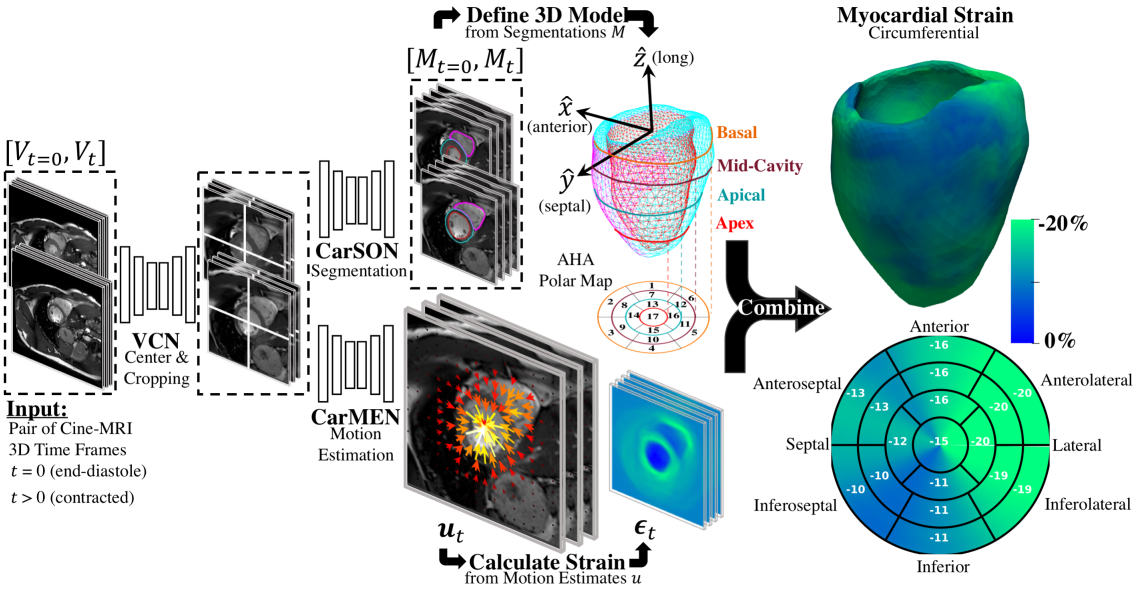

Figure 3-1: Overview of proposed DeepStrain workflow.

end-systolic strain, defined as the global strain value at end-systole; systolic strain rate, defined as the peak (i.e., maximum) absolute value of global strain rate during systole; early-diastolic strain rate, defined as the peak absolute value of global strain rate during diastole.

3.3 Method

3.3.1 Centering, Segmentation, and Motion Estimation

DeepStrain consists of a series of convolutional neural networks that perform three tasks: a ventricular centering network (VCN) for automated centering and cropping, a cardiac segmentation network (CarSON) to generate tissue labels, and CarMEN to generate u_t using the formulation described in section 2.2.2. The estimates u_t are used to calculate myocardial strain, and segmentations are used to calculate morphological and functional parameters of cardiac function, identify a cardiac coordinate system and regions-of-interest necessary for strain analysis, and generate tissue labels from unlabeled cine frames that can be leveraged for anatomical regularization of motion estimates at training time (Fig. 3-1).

Shared Architecture

DeepStrain decouples segmentation and motion estimation tasks, enabling inspection of sources of error from each task independently. However, inspection of potential sources of error would be challenging if each task was formulated using drastically different network architectures. Thus, building upon our first implementation described in section 2.3.1, CarMEN was modified such that all networks in the DeepStrain workflow have a common encoder-decoder architecture.

Let C_k denote a Convolution-BatchNorm-PReLU layer with k filters. CD_k denotes an Upsampling-Convolution-BatchNorm-PReLU layer with upsampling applied using nearest-neighbor interpolation of stride $2 \times 2 \times 2$. Unless specified, all convolutions are $3 \times 3 \times 3$ spatial filters applied with $1 \times 1 \times 1$ stride. An encoding layer Ek consists of a C_k layer followed by a second C_k layer with stride $2 \times 2 \times 2$. A third C_k layer follows but without BatchNorm-PReLU. The output is the residual connection made by element-wise addition of the second C_k layer before BatchNorm-PReLU are applied, and the third C_k layer. A decoding layer Dk consists of a C_k layer with $(1 \times 1 \times 1)$-sized filters followed by CDk and C_k layers. Thus, the $2 \times 2 \times 2$ strided convolution in Ek downsamples by a factor of 2, whereas the upsampling operation with stride $2 \times 2 \times 2$ in Dk upsamples by a factor of 2.

With this notation, the encoder-decoder architecture common to all three networks consists of an encoder with E64-E128-E256-E512-E512-E512-E512 layers, and a decoder with D512-D512-D512-D256-D128-D64 layers. After the last layer in the decoder, a final CDk layer without BatchNorm -PReLU and with $(1 \times 1 \times 1)$-sized filters is applied to map to the number of output channels (k=1 for VCN, 4 for CarSON, and 3 for CarMEN). Exceptions to the rules above are: (1) CarSON consists of two-dimensional operations, i.e., convolutions are 3×3 spatial filters applied with 1×1 stride. (2) For CarMEN, we experimented with another implementation where all filters and strides were of size 1 along the third dimension, motivated by the fact that subjects had variable resolution along that dimension.

VCN

Let V denote a cine frame with $n = 3$ as defined in section 2.2.1. VCN uses a single-channel array V with size $256 \times 256 \times 16$ to generate a single-channel array G_{pred} of equal size, where G_{pred} corresponds to a Gaussian distribution with mean defined as the left-ventricular myocardium center of mass. This approach models the uncertainty associated with the center location, especially in pathological cases, and enables automated generation of ground-truth labels when manual segmentation of uncropped images is available. VCN was trained using the mean square error loss function

$$\mathcal{L}_{MSE}(G_{gt}, G_{pred}) = \frac{1}{|\Omega|} \sum_{v \in \Omega} \big(G_{gt}(v) - G_{pred}(v)\big)^2 \tag{3.2}$$

At inference, the input volume V_t is centered and cropped around the voxel with the highest value in G_{pred} to generate a new cropped array of size $128 \times 128 \times 16$, which is the input to CarSON and CarMEN.

CarSON

Let V, M denote corresponding grayscale and labeled cine frames with $n = 2$ as defined in section 2.2.1. CarSON is a two-dimensional architecture that uses single-channel images $V$of size 128×128 to generate a 4-channel labeled images M_{pred} of equal size, each channel corresponding to a label of a cardiac structure. We experimented with two different variations of a loss function $\mathcal{L}_{seg}$ to train CarSON using the manual segmentations M_{gt} as the ground-truth labels. First, the multi-class Dice coefficient loss function

$$\mathcal{L}_{seg} := \mathcal{L}_{MDC}(M_{gt}, M_{pred}) = -\frac{1}{4} \sum_{k=0}^{3} 2 \frac{|v_{gt}^k \cap v_{pred}^k|}{|v_{gt}^k| + |v_{pred}^k|}, \tag{3.3}$$

where $k \in [0, 3]$ represents each of the tissue labels (i.e., background, right-ventricular cavity, left-ventricular myocardium, and left-ventricular cavity), and $v^k \in \Omega^K$ denotes all the pixels with label k. Second, the pixel-wise categorical cross-

entropy:

$$\mathcal{L}_{seg} := \mathcal{L}_{CCE}(M_{gt}, M_{pred}) = -\frac{1}{4\Omega^K} \sum_{k=0}^{3} \sum_{v \in \Omega^K} v_{gt}^k \ \log(v_{pred}^k) \tag{3.4}$$

CarMEN

Let V_t, M_t denote corresponding grayscale and labeled cine frames with $n = 3$ as defined in section 2.2.1. Although the current implementation of CarMEN shares some similarities with that presented in section 2.3.1, both having the same convolutional neural network formulation discussed in section 2.2.2, we have made several design modifications that were specific for accurate strain quantification. Specifically, in addition to the unsupervised loss functions (2.2) and (2.3), we used a supervised function $\mathcal{L}_{anatomical}$ that leverages segmentations of the input volumes at training time to impose an anatomical constrain on the estimates

$$\mathcal{L}_{anatomical}(M_{t=0}, u_t \circ M_t) = \mathcal{L}_{seg}(M_{t=0}, u_t \circ M_t) \tag{3.5}$$

This loss term is useful when manual segmentations of various cardiac tissues are available during training but not during testing, or when weak labels can be quickly derived using an automated technique (e.g., CarSON). We experimented with different function variations of the anatomical constrain (3.5), namely (3.3) and (3.4). Thus, the semi-supervised loss function for CarMEN is a linear combination of (2.2), (2.3), and (3.5), weighted by λ_i, λ_s, λ_a, accordingly:

$$L = \lambda_i \mathcal{L}_{MAE}(V_{t=0}, u_t \circ V_t) + \lambda_s \mathcal{L}_{\nabla}(u_t) + \lambda_a \mathcal{L}_{anatomical}(M_{t=0}, u_t \circ M_t) \tag{3.6}$$

Other variations were exclusive to estimation of motion from three-dimensional cine frames. Convolution, pooling, and upscaling was implemented with $3 \times 3 \times k_z$ operations, where k_z could be set to either 1 or 3. For $k_z = 1$, operations were carried out only in the x-y-plane to account for the low and varying z resolution, different

from three-dimensional architectures for segmentation with $3 \times 3 \times 3$ convolutions and in-plane-only pooling and upscaling [56]. Thus, context in the z-dimension is aggregated through trilinear interpolation of V_t and M_t volumes in (2.2) and (3.5), and through application of three-dimensional spatial gradients to u_t in (2.3). At inference, the entire cycle of a single subject can be analyzed using sequential inputs $\{(V_{t=0}, V_t)\}_{\{t=0,1,\ldots,T\}}$.

3.4 Experiments

3.4.1 Datasets

In this study, the ACDC dataset introduced in section 2.4.1 was used for development, and the publicly available cardiac motion analysis challenge (CMAC) dataset was used for evaluation of motion and strain accuracy. Additionally, we acquired cine data at the A.A. Martinos Center for Biomedical Imaging to assess intra-scanner repeatability of strain measures.

Cardiac Motion Analysis Challenge Dataset

The CMAC dataset consists of paired tagging- and cine data from 15 healthy subjects (three female, aged 28 $\pm$ 5 years) acquired at the Division of Imaging Sciences and Biomedical Engineering, King's College London, United Kingdom [135]. The datasets were acquired using a 3T Philips Achieva System (Philips Healthcare, Best, The Netherlands). Each dataset included 12 landmarks defined at end-diastolic on the tagging grid and manually-tracked throughout the cardiac cycle by the challenge organizers (Fig. 3-2). The purpose of these landmarks is to assess the accuracy of motion estimates derived from either tagging- or cine data as detailed in section 3.4.3.

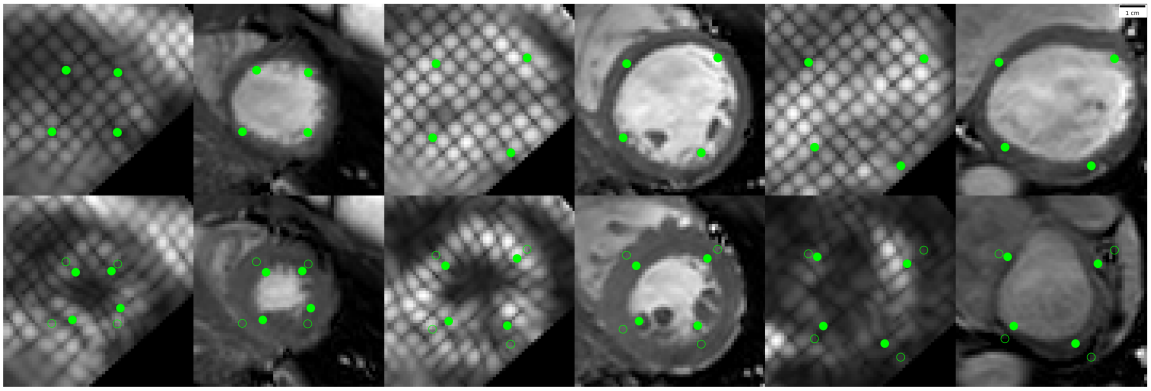

Figure 3-2: Representative subject from the CMAC dataset with tagging- and cine images at end-diastole (top) and end-systole (bottom). Landmarks (green) were defined at end-diastole and manually-tracked throughout the cardiac cycle by the CMAC challenge organizers. Left to right: septal, mid, and basal landmarks.

Intra-Scanner Repeatability Dataset

This dataset consists of 10 healthy subjects recruited to undergo repeated scans. Standard cardiac MR protocols were acquired on a 3 T MR system (Biograph mMR, Siemens Healthiness, Germany, Erlangen) in healthy volunteers during two separate consecutive scan sessions on the same day (Fig. 3.4.1). Written consent was obtaining from all volunteers with approval of the Institutional Review Board (2018P002912) and in agreement with the Health Insurance Portability and Accountability Act at the Massachusetts General Hospital. The major inclusion criteria were >21 years old, no history of cardiovascular disease, and no MR contradictions. Each MR protocol included standard localizer scans and a single slice cine acquisition in a long cardiac axis view, followed by a stack of short axis cines covering the heart from the base to the apex using a retrospectively ECG gated balanced steady-state gradient echo sequence with the following parameters; repetition time=38.61ms, echo time=1.26ms, flip angle=28 degrees, field-of-view=277 mm×340 mm, matrix size=208×170, slice thickness=6mm, slice gap=6mm. After each full protocol, the volunteers were asked to leave the scanner room before going back in for a second acquisition of exactly the same protocol.

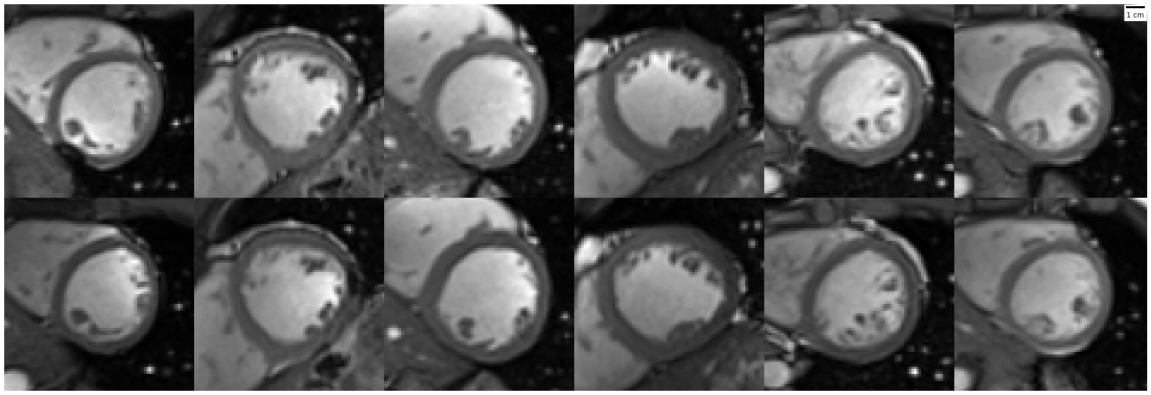

Figure 3-3: Representative cine end-diastolic images at mid-ventricle from six subjects from the Martinos dataset from acquisition 1 (top) and 2 (bottom).

Preprocessing

All frames were resampled to a 256×256×16 volume grid with 1.25 mm×1.25 mm in-plane resolution and variable slice thickness (4-7 mm).

3.4.2 DeepStrain Implementation

For optimization experiments and final model training, all networks were trained in TensorFlow ver. 2.0 with Adam optimizer parameters beta1,2 = 0.9,0.999, random initialization, batchsize = 80 (5 for CarMEN), and learning rate = 1×10^{-4}.

Design of a strain quantification-specific CNN

Reported normal ranges of strain in healthy individuals using non-learning methods vary largely between the different deformation methodologies, limiting the clinical utility of strain measures. We used this concept as a heuristic in updating CarMEN, i.e., a useful design should minimize the variation in strain values in healthy individuals. To assess the impact of design choices on this heuristic, we separated the ACDC training set into two group-balanced train and test subsets, each with 50 subjects. We trained CarMEN for 300 epochs using two different layer operation sizes (i.e., $3 \times 3 \times k_z$ with $k_z \in \{1, 3\}$), and two different implementations of $\mathcal{L}_{seg}$ in (3.5), namely the multi-class Dice coefficient and categorical cross entropy losses.

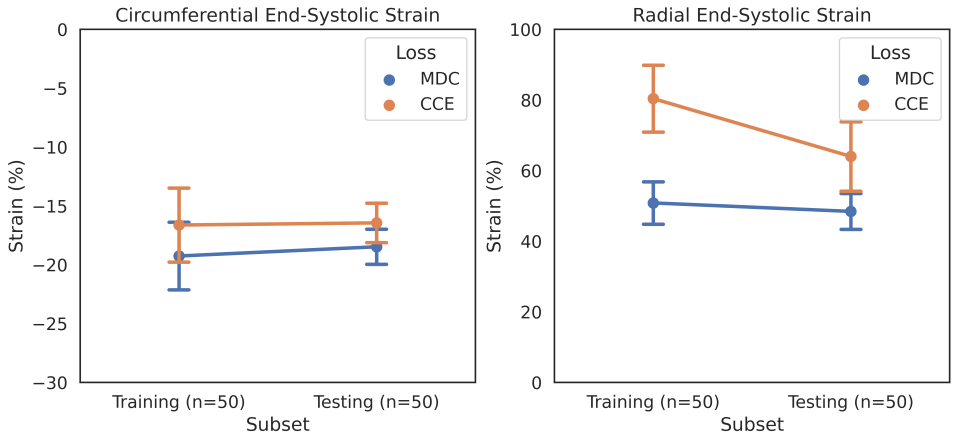

Figure 3-4: Effect of anatomical regularization of motion estimates on strain. Regularization with multiclass Dice coefficient (MDC) and categorical crossentropy (CCE) functions result in different strain values in healthy subjects, shown as mean and standard deviation.

With $k_z = 3$ comparison of loses showed that categorical cross entropy leads to increased standard deviation in radial end-systolic strain in healthy train (n=10) and test (n=10) subjects, and large differences in the average radial end-systolic strain between training and testing sets (Fig. 3-4). Multiple experiments with different regularization parameters showed similar results, and that setting $k_z = 1$ reduces deviations in healthy strain. Thus, the new CarMEN design used $3 \times 3 \times 1$ operations and was regularized using the multi-class Dice coefficient loss function.

Novel loss weighting strategy for accurate motion and strain estimation

Most proposed networks to-date have used registration terms such as (2.2) and (3.5) to indirectly assess the accuracy of u_t on validation or test datasets, including our own evaluation in section 2.4.3. However, this approach is prone to errors since inaccurate and even unrealistic u_t solutions can minimize these terms. To find an optimal balance between loss terms, we simulated cardiac cine frames with known ground-truth motion. Specifically, we used the established extended cardiac-torso (XCAT) phantom software to generate three-dimensional anatomy masks at multiple time frames with size $128 \times 128 \times 16$ and average resolution set to $1.5 \times 1.5 \times 5$ mm^3 [125]. We used the XCAT extension, MRXCAT [150], to simulate the MR acquisitions on

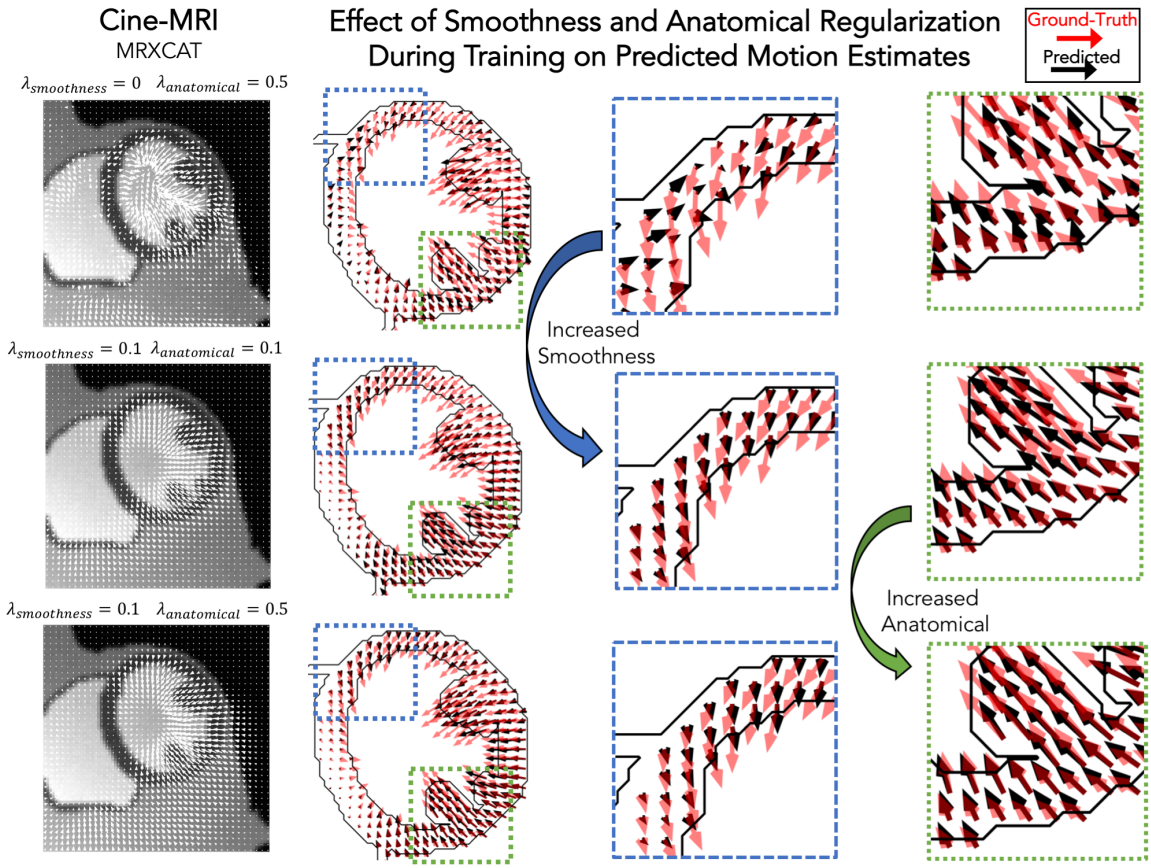

Figure 3-5: First row shows the predicted (black) motion estimates when the anatomical regularization is set to 0.5 and smoothing is set to 0. Relative to the ground-truth (red), these estimates are highly irregular. Increasing (third colum) the smoothness to 0.1 and setting anatomical to 0.1 improves the direction of the estimates, but the magnitude is reduced. This is corrected by increasing anatomical regularzation to 0.5 (fourth column).

the anatomy masks. Each simulation consisted of three frames approximately at end-diastole, mid-systole, and end-systole. We then trained CarMEN with various regularization parameters for 300 epochs using 100 subjects from the ACDC train set, and tested the models on the MRXCAT data by evaluating the end-point error between ground-truth and predicted motion estimates within the left ventricle myocardium.

Setting $\lambda_s = 0$ leads to highly irregular motion vectors (e.g., off by more than 90 degrees) relative to ground-truth (Fig. 3-5). Setting the smoothness and anatomical weights to $\lambda_s = \lambda_a = 0.1$ leads to smoother and better aligned vectors, albeit with a

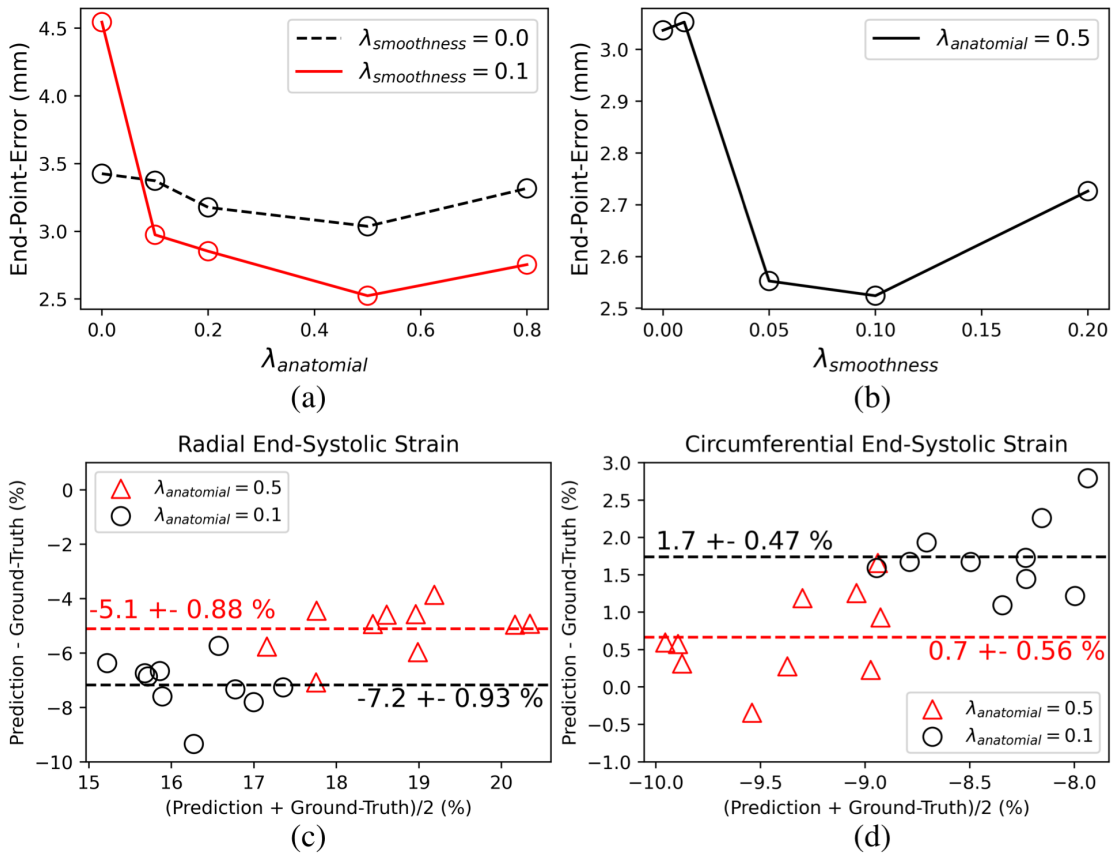

Figure 3-6: Qualitative effects of smoothing and anatomical regularization on the accuracy of motion estimates. First row shows the predicted (black) motion estimates when the anatomical regularization is set to 0.5 and smoothing is set to 0. Relative to the ground-truth (red), these estimates are highly irregular. Increasing (third column) the smoothness to 0.1 and setting anatomical to 0.1 improves the direction of the estimates, but the magnitude is reduced. This is corrected by increasing anatomical regularzation to 0.5 (fourth column).

slightly decreased magnitude. Increasing the anatomical weight to $\lambda_a = 0.5$ further improves the estimates by generating vectors with similar magnitude and orientation to the ground-truth. Quantitative measures of motion accuracy showed similar results across various regularization values, and these changes in motion estimation accuracy were reflected as bias changes in strain values (Fig. 3-6). We found the optimal parameters to be $\lambda_i = 0.01, \lambda_a = 0.5, \lambda_s = 0.1$.

Final model training

Ground-truth distributions for VCN were created using the manual segmentations. VCN and CarSON were trained using the end-diastolic and end-systolic frames of the train set, as only these included ground-truth segmentations. This provided 200 training samples for VCN and 3200 for CarSON, the latter having more samples since it is a 2D architecture and all frames were resampled to a volume with 16 slices. VCN was tested by five-fold cross-validation, whereas the accuracy of CarSON was assessed by submitting the results to the challenge website. Once CarSON was trained, we generated segmentations of the test set to train CarMEN using the entire ACDC dataset, i.e., 100 subjects from the train set with manual segmentations and 50 from the test set with CarSON-predicted segmentations. Only the ED-ED and ED-ES pairs were used for training. The former pair is useful for the network to learn the identity transformation. Data augmentation included random rotations and translations, random mirroring along the x and y axes, and gamma contrast correction. All data augmentation was performed only in the x-y plane.

3.4.3 Evaluation Metrics

Evaluation of CarSON

The CarSON-predicted and manual segmentations were compared using the Hausdorff distance and Dice score metrics at both end-diastolic and end-systolic phases. Accuracy of left-ventricular morphological and functional measures derived from segmentations, including end-diastolic volume, ejection fraction, and left-ventricular myocardium, was assessed using the correlation, bias, and standard deviation metrics. The mean absolute error for the end-diastolic volume and myocardium were also computed for comparison against the intra- and inter observer variability reported by [39]. Right-ventricular labels were not analyzed since they were not used to assess cardiac function but rather to define the direction of the septal wall, which is needed to construct the left-ventricular strain polar maps with a normalized orientation between subjects. We compared our results to top-3 ranked methods published for the ACDC

test set as these appear in the leader-board of the challenge [128, 56, 165, 12].

Evaluation of CarMEN

CMAC organizers defined 12 landmarks at intersections of gridded lines on tagging images at end-diastole, one landmark $p_{t=0}$ per wall (septal, inferior, lateral, interior) per ventricular level (basal, mid, septal). These landmarks were manually-tracked on tagging images by two observers over the cardiac cycle, and each position was transformed from tagging to cine coordinates using DICOM header information (Fig. 3-2). We used the CarMEN motion estimates u_t to automatically deform the landmarks from end-diastolic to contracted phases, and the accuracy was assessed using the in-plane end-point error function L_{EPE} between deformed $p'_t = u_t \circ p_{t=0}$ and manually-tracked p_t landmarks, defined by

$$L_{EPE}(p, p') := \sqrt{(p_x - p'_x)^2 + (p_y - p'_y)^2} \tag{3.7}$$

Due to temporal misalignment between the tagging and cine acquisitions, (3.7) was evaluated only at end-systole. Specifically, let $p_t^{i,j}$ denote the landmarks of subject i at frame t manually-tracked by observer j. The accuracy of CarMEN was assessed using the average end-point error

$$\frac{1}{2n} \sum_{i=1}^{n} \sum_{j=1}^{2} L_{EPE}(p_{t=ES}^{i,j}, u_{t=ES} \circ p_{t=0}^{i,j}) \tag{3.8}$$

Our results were compared to those reported by the four groups that responded to the challenge [135], MEVIS [132], IUCL [127], UPF [19], and INRIA [85, 89]. All groups submitted tagging-based motion estimates, but only UPF and INRIA provided estimates based on cine MR.

Evaluation of DeepStrain

The tagging method with the lowest average end-point error at end-systole was used as the reference for strain analysis. The tagging-based motion estimates were registered and resampled to the cine space. Global strain and strain rate values throughout the

entire cardiac cycle were derived from the resampled estimates, and were compared to cine based strain measures obtained with DeepStrain using Bland-Altman Analysis.

Repeatability of DeepStrain

Global- and regional-based analyses were performed to assess the repeatability of measures from two acquisitions using the Martinos dataset described in section 3.4.1. Relative changes and absolute relative changes were calculated, taking the first acquisition as the reference. End-systolic strain and strain rate were calculated for the global-based analysis. or region-based analyses, end-systolic strain values were normalized using the polar map, and both relative change and absolute relative change were evaluated for each of the segments in the polar map.

Statistics

For validation, Bland-Altman analysis was used to quantify agreement between predicted and tagging strain measures. We used the term bias to denote the mean difference and the term precision to denote the standard deviation of the differences, the latter computed with 1-degree of freedom. Differences were also assessed using a paired t-test with Bonferroni correction for multiple comparisons. For global- and regional-based analyses of strain intra-scanner repeatability, intraclass correlation coefficient (ICC) estimates and their 95% confidence intervals were calculated based on a single-rating, absolute agreement, 2-way mixed-effects model. Analyses were performed on Python v3.4 with the statistical pingouin module.

3.5 Results

3.5.1 Centering, Segmentation and Motion Estimation

Centering, segmentation, and motion estimation for an entire cardiac cycle (25 frames) was accomplished in $<$13s on a 12GB graphic processing unit and $<$2.2 min on a 32GB RAM CPU. VCN located the left-ventricular center of mass with a median

error of 1.3 mm. Training with a multi-class Dice coefficient loss function resulted in slightly more accurate segmentations compared to categorical cross-entropy (Table 3.1), therefore the former model was used for all remaining analyses. With this model, correlation of CarSON and manual left-ventricular morphological and functional measures was >0.98 across all measures, and biases in ejection fraction (+0.25 ± 3.2%), end-diastolic (+0.76 ± 6.7 mL) and end-systolic (+0.19 ± 5.8 mL) volumes, and mass (+1.4 ± 10.3 g) were not significant. Further, these biases were smaller than those obtained with other methods, which were positive for end-diastolic volume (1.5 to 3.7 mL), negative for the myocardium (-2.1 to -2.9 g), and close to zero (±0.5%) for EF. Simantiris *et al.* [128] obtained the best precision for ejection fraction (2.7 vs. 3.2% variance with CarSON), end-diastolic volume (4.6 vs. 6.7 mm), and myocardium (6.5 vs. 10.3 g). Isensee *et al.* [56] obtained the best results on geometric metrics, i.e., lower Hausdorff distance for the left-ventricular cavity (end-diastole 5.5 vs. 5.7 mm; end-systolic 6.9 vs. 7.7 mm) and myocardium (7.0 vs. 8.1 mm; 7.3 vs. 9.2 mm), and higher Dice score for the myocardium (0.904 vs. 0.898; 0.923 vs. 0.913). The Dice score for the cavity was similar for all methods (0.967, 0.929). The mean absolute error for the end-diastolic volume and myocardium were 5.3 ± 4.1 mL and 6.8 ± 6.5 g.

Fig. 3-7a illustrates a representative example of the tagging and cine images from a CMAC subject. Landmarks defined at end-diastolic were deformed to end-systolic using the CarMEN estimates and compared to manual tracking. Banding artifacts on cine images showed no clear effect on derived motion estimates or landmark deformation at end-systolic or throughout the whole cardiac cycle. The manual tracking inter-observer variability was 0.86 mm (Fig. 3-7b, dotted line). Within cine-based techniques, CarMEN (2.89 ± 1.52 mm) and UPF (2.94 ± 1.64 mm) had lower ($p<0.001$) absolute end-point error relative to INRIA (3.78 ± 2.08 mm), but there was no significant difference between CarMEN and UPF. All tagging-based methods had lower absolute end-point error compared to cine approaches, particularly MEVIS (1.58 ± 1.45 mm).

Table 3.1: State-of-the-art methods for left-ventricular segmentation shown at end-diastole (ED) and end-systole (ES) on the ACDC test set compared to proposed approach. Red are the best results for each metric.

Left-Ventricle Label		**Dice Similarity Coefficient**		**Hausdorff Distance**		**Ejection Fraction**			**End-Diastolic Volume**		
Rank	Method	ED val.	ES val.	ED mm	ES mm	Corr. val.	bias±std %		Corr. val.	bias±std mL	
*	**CarSON MDC**	0.97	0.93	5.66	7.68	0.99	0.25	3.18	1.00	0.76	6.67
*	**CarSON CCE**	0.95	0.89	6.87	8.68	0.99	0.88	3.13	1.00	0.85	6.72
1	Simantiris *et al.*	0.97	0.93	6.37	7.57	0.99	-0.36	2.69	1.00	2.03	4.61
2	Isensee *et al.*	0.97	0.93	5.48	6.92	0.99	0.49	2.97	1.00	1.53	5.74
3	Zotti *et al.*	0.96	0.91	6.18	8.39	0.99	-0.48	3.11	1.00	3.75	5.15
Myocardium Label		**Dice Similarity Coefficient**		**Hausdorff Distance**		**Left-Ventricular Mass**			**End-Systolic Volume**		
Rank	Method	ED val.	ES val.	ED mm	ES mm	Corr. val.	bias±std g		Corr. val.	bias±std mL	
*	**CarSON MDC**	0.90	0.91	8.13	9.19	0.98	1.41	10.32	0.99	1.15	9.39
*	**CarSON CCE**	0.86	0.87	8.90	10.35	0.98	0.96	9.60	1.00	-1.16	6.39
1	Isensee *et al.*	0.90	0.92	7.01	7.33	0.99	-2.55	8.28	0.99	-1.98	8.34
2	Simantiris *et al.*	0.89	0.90	8.26	9.58	0.99	-2.90	6.46	0.98	-2.13	10.11
3	Calisto *et al.*	0.87	0.90	8.20	8.32	0.99	-2.10	7.91	0.99	-1.79	8.58

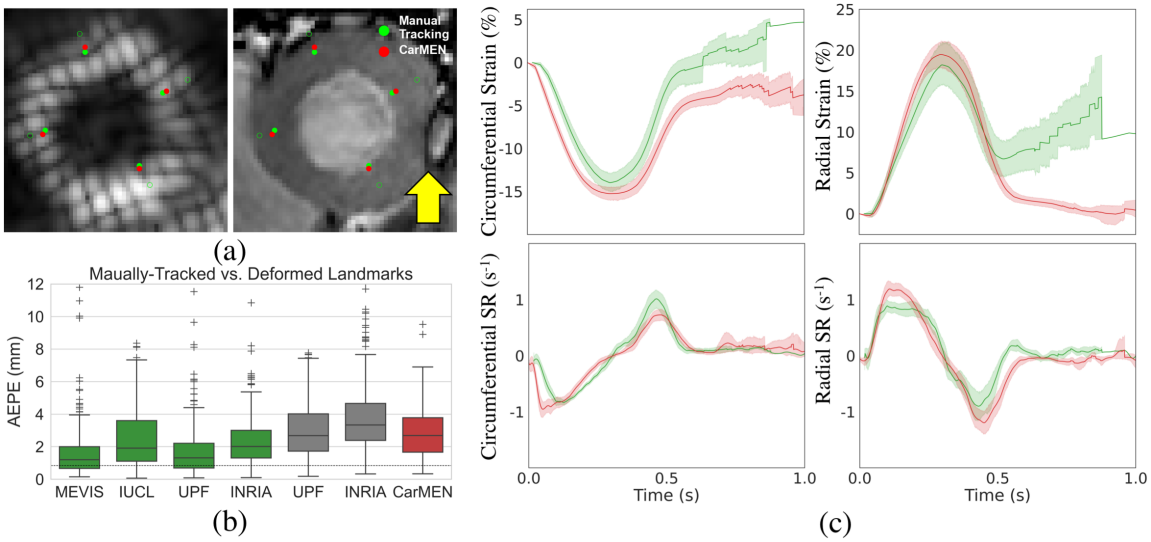

Figure 3-7: Validation of motion and strain. (a) Landmarks at end-diastole (unfilled green) are manually-tracked (green) and deformed with CarMEN to endsystole (red). Yellow arrow indicates a banding artifact. (b) Average end-point-error (AEPE) at end-systole between manual and CarMEN-deformed landmarks was assessed and compared to other methods. (c) MEVIS- and DeepStrain-based strain (top) and strain rate (SR, bottom) measures are compared.

3.5.2 Strain validation against tagging-MRI

Table 3.2 shows the normal ranges (mean [95% confidence interval]) of strain derived from cine data for all healthy subjects, including subjects from the training,

validation, and repeatability cohorts. Across datasets, DeepStrain generated values with narrow confidence intervals of end-systolic strain (circumferential: 1.1%, radial: 2.5%), systolic strain rate (0.13 s^{-1}, 0.19 s^{-1}), and early-diastolic strain rate (0.14 s^{-1}, 0.26 s^{-1}). Specifically, circumferential and radial values across datasets were: -16.9% [-17.4 -16.3] and 23.2% [22 24.4] for end-systolic strain, -1.1 s^{-1} [-1.2 -1.1] and 1.4 s^{-1} [1.3 1.5] for systolic strain rate, and 0.80 s^{-1} [0.73 0.86] and -1.5 s^{-1} [-1.6 -1.3] for early-diastolic strain rate, accordingly. These values were similar to tagging-based ones, although circumferential early-diastolic strain rate from cine data was lower, mostly in the train set (0.7± 0.2 s^{-1}).

Comparison of tagging- and cine-based strain measures with matched subjects showed an overall agreement in timing and magnitude of strain and strain rate throughout the cardiac cycle, although there were visual differences in peak strain rate parameters (Fig. 3-7c). Visual inspection of image artifacts on cine data showed no evidence that these artifacts affected strain values derived with DeepStrain. Quantitative comparisons of tagging- and cine-based measures showed biases in circumferential end-systolic strain (-14.2 ± 2.2 vs. -15.3 ± 1.5%; bias -1.17 ± 2.93%), radial end-systolic strain (18.4 ± 5.1 vs. 19.7 ± 3.4%; +1.26 ± 5.37%) and early-diastolic strain rate (-1.2 ± 0.5 vs. -1.4 ± 0.3; -0.21 ± 0.52 s^{-1}) were not significantly different from zero. However, there were larger differences ($p<0.01$) in radial systolic strain rate (1.0 ± 0.2 vs. 1.3 ± 0.2 s^{-1}; 0.32 ± 0.34 s^{-1}), and circumferential systolic strain rate (-0.9 ± 0.1 vs. -1.2 ± 0.2 s^{-1}; 0.30 ± 0.22 s^{-1}) and early-diastolic strain rate (1.2 ± 0.2 vs. 0.8 ± 0.1 s^{-1}; 0.40 ± 0.23 s^{-1}).

3.5.3 Strain Intra-Scanner Repeatability

Global strain time series derived from repeated acquisitions are shown in Fig. 3-8a. The overall bias in circumferential and radial end-systolic strain were 0.17% and -0.16%, accordingly. Average relative change between parameters was less than ± 1% for end-systolic strain and less than ± 5% for peak strain rate (Table 3.3). Average absolute relative change was 5% for end-systolic strain (circumferential: 3.0 ± 2.0%; radial: 5.1 ± 5.8%), 8% for systolic strain rate (8.0 ± 6.8%; 7.7 ±

Table 3.2: Normal ranges of strain with DeepStrain in healthy subject. Tagging-based measures are shown for the CMAC cohort. DeepStrain repeatability is shown for two acquisitions (ACQ)

	ACDC (n=20)	CMAC (n=15)		MARTINOS (n=10)		COMBINED (n=45)
	Cine	Tagging	Cine	Cine ACQ 1	vs. ACQ 2	Cine
			End-Systolic Strain (%)			
Circ	-17.8 (1.6)	-14.2 (2.2)	-15.3 (1.5)	-17.3 (0.7)	-17.5 (0.9)	-16.9 [-17.4 16.3]
Rad	24.5 (2.9)	18.4 (5.1)	19.7 (3.4)	25.9 (3.4)	25.7 (4.1)	23.2 [22.0 24.4]
			Systolic Strain Rate (s^{-1})			
Circ	-1.1 (0.2)	-0.9 (0.1)	-1.2 (0.2)	-1.0 (0.2)	-1.0 (0.2)	-1.1 [-1.2 -1.1]
Rad	1.3 (0.4)	1.0 (0.2)	1.3 (0.2)	1.7 (0.3)	1.6 (0.3)	1.4 [1.3 1.5]
			Early-Diastolic Strain Rate (s^{-1})			
Circ	0.7 (0.2)	1.2 (0.2)	0.8 (0.1)	1.0 (0.2)	1.0 (0.2)	0.80 [0.73 0.86]
Rad	-1.4 (0.5)	-1.2 (0.5)	-1.4 (0.3)	-1.8 (0.3)	-1.7 (0.4)	-1.5 [-1.6 -1.3]

4.0%), and 10% for early-diastolic strain rate (10.2 ± 7.8%; 9.2 ± 8.6%). Mean ICC values showed repeatability was good to excellent for end-systolic strain (0.75; 0.90), systolic strain rate (0.77, 0.91), and early-diastolic strain rate (0.83, 0.84). The limits of agreement, which defines the interval where to find the expected differences in 95% of the cases assuming normally distributed data, were 2% and 6% for circumferential and radial end-systolic strain, and 0.5 s^{-1} for strain rate measures. Average relative change and absolute relative change across regional segments were within ± 2% for circumferential and ± 5% for radial end-systolic strain, except in anterior segments (± 8%) radially (Fig. 3-8b). Regional mean ICC values showed good to excellent repeatability across all segments, except circumferentially near inferoseptal, inferior, and inferolateral walls where repeatability was moderate (Supplementary Table 1). Limits of agreement showed that 95% of differences occurred within 5% and 10% intervals for circumferential and radial end-systolic strain.

3.5.4 Evaluation in Cardiac Patients

Global values of strain and strain rate across the cardiac cycle (Fig. 3-9) for all 100 subjects in the ACDC train set showed progressive decline in strain values starting

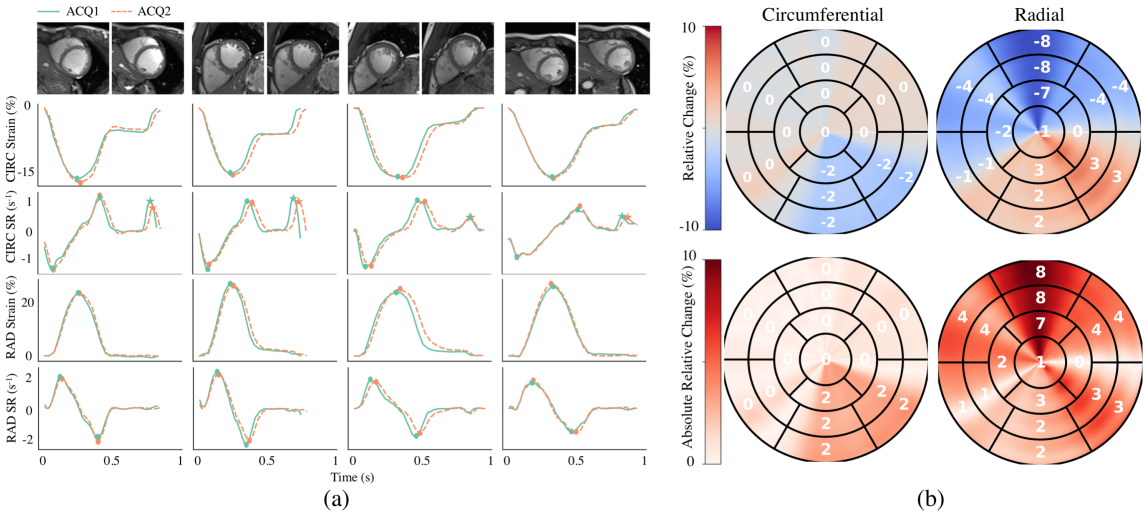

Figure 3-8: Intra-scanner repeatability of (a) global and (b) regional myocardial strain measures

Table 3.3: Intra-scanner repeatability of global circumferential (CIRC) and radial (RAD) strain measures.

Measure	RC (%)	aRC (%)	ICC [95% CI]	LoA
Circ ESS	1.0 (3.6)	3.0 (2.0)	0.75 [0.22-0.92]	[-1.36 1.02 %]
Rad ESS	-0.9 (7.9)	5.1 (5.8)	0.90 [0.64-0.97]	[-3.03 3.36 %]
Circ SRs	0.8 (10.8)	8.0 (6.8)	0.77 [0.31-0.94]	[-0.23 0.22 s^{-1}]
Rad SRs	-4.9 (7.4)	7.7 (4.0)	0.91 [0.67-0.98]	[-0.15 0.34 s^{-1}]
Circ SRe	2.5 (13.0)	10.2 (7.8)	0.83 [0.47-0.96]	[-0.26 0.22 s^{-1}]
Rad SRe	-2.5 (12.7)	9.2 (8.6)	0.84 [0.50-0.96]	[-0.32 0.41 s^{-1}]

with hypertrophic cardiomyopathy, followed by abnormal right ventricle, myocardial infarction, and dilated cardiomyopathy. Specifically, relative to the healthy group, radial end-systolic strain was reduced in all patient populations. Radial systolic and early-diastolic strain rate were also reduced in all patient groups, except for systolic strain rate in hypertrophic cardiomyopathy. Fig. 3-10 shows both the cine image and the circumferential end-systolic strain polar map of a healthy subject and two patients with myocardial infarction. Strain values in the healthy polar map have a homogeneous distribution. In contrast, in one myocardial infarction patient the map indicates a diffused reduction, and inspection of the myocardium on the cine image shows an anteroseptal infarct that coincides in location with segments with more

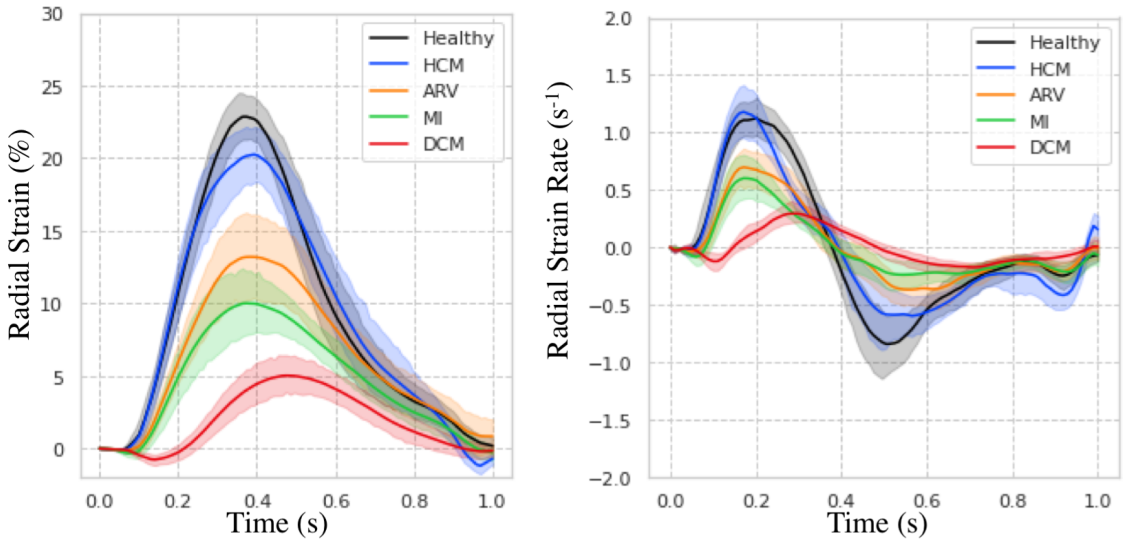

Figure 3-9: Radial strain and strain rate measures on the ACDC train set.

prominent decreases in strain. In a different myocardial infarction patient with an infarct located in a similar septal region, strain changes are focal and localized to the anteroseptal wall.

3.6 Discussion

In this study we developed a fast deep learning framework for strain analysis based on cine data that does not make assumptions about the underlying physiology, and we benchmarked its segmentation, motion, and strain estimation components against the state-of-the-art. We compared our segmentations to other deep learning methods, motion estimates to other non-learning techniques, and strain measures to a reference tagging technique. We also presented the intra-scanner repeatability of DeepStrain-based global and regional strain measures, and showed that these measures were robust to image artifacts in all cases were distortions were present. Global and regional applications were also presented to demonstrate the potential clinical utilization of our approach. Our work is the first to report within a single study the characterization, validation, and repeatability of a learning-based method for strain analysis.

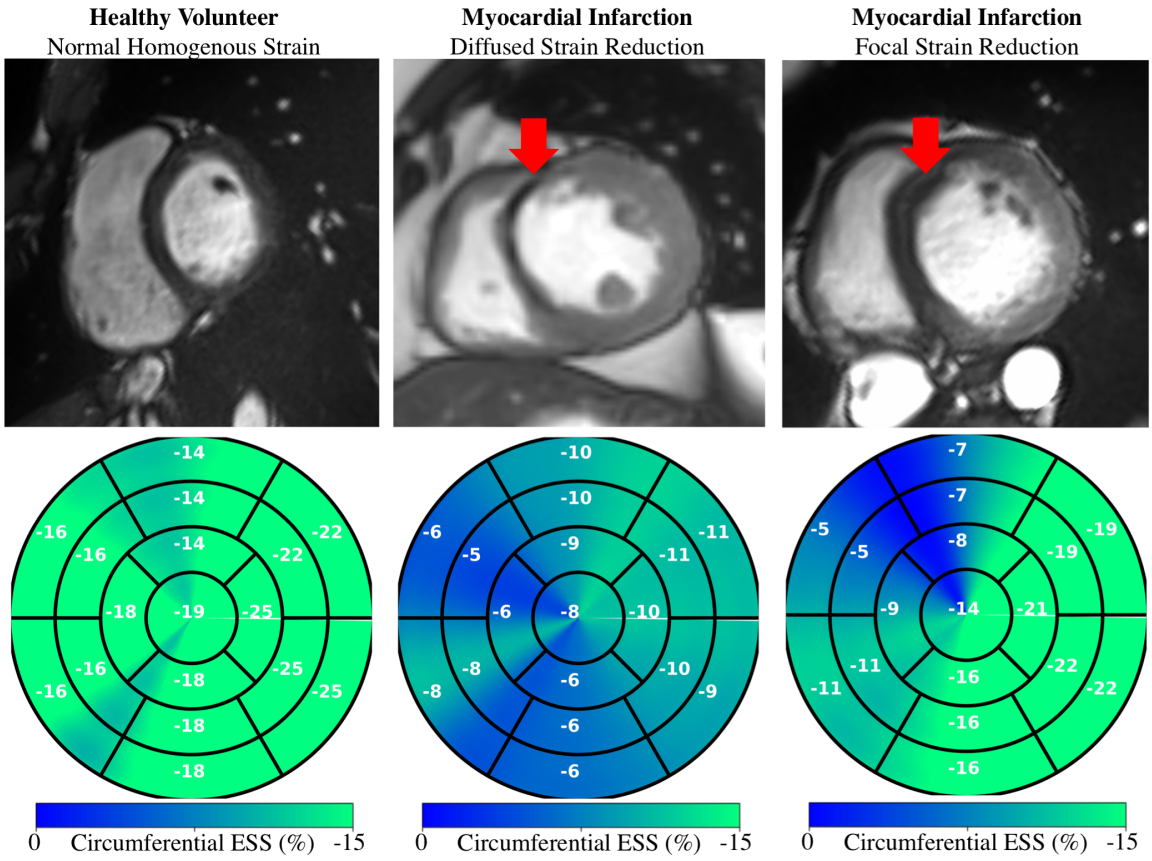

Figure 3-10: Regional strain in healthy and patients with MI. Myocardial infarction can result in diffused (center) and focal (right) strain reduction.

3.6.1 Validation

Validation of morphological and functional measures

Segmentation from MR data is a task particularly well suited for convolutional neural networks given the excellent soft-tissue contrast, thus all top performing methods on the ACDC test set were based on deep learning approaches. Isensee *et al.* [56] had remarkable success on geometric metrics, but this and other approaches resulted in a systematic overestimation of the left-ventricular end-diastolic volume and thus underestimation of the myocardium mass. In contrast, CarSON generated less biased measures of volume and mass, which were not significant. Although Simantiris *et al.* [128] obtained the most precise measures, possibly due to their extensive use of augmentation using image intensity transformations, across methods the precision of ejection fraction was within the 3-5% [49] needed when it is used as an index

of left-ventricular function in clinical trials [50]. Lastly, we showed that the mean absolute error in our measures of end-diastolic volume and mass was almost half the inter-observer (10.6 mL, 12.0 g), and comparable to the intra-observer (4.6 mL, 6.2 g) reported in [11]. Further investigations are required to assess the performance on more heterogeneous populations.

Validation of motion tracking

The CMAC dataset enabled us to compare our results to non-learning methods using a common dataset. We found that the average end-point error at end-systolic was lower with tagging-based techniques, reflecting the advantage of estimating cardiac motion from a grid of intrinsic tissue markers (i.e., grid tagging lines). Further, the tagging techniques also benefited from the fact that landmarks were placed near the center of the myocardial wall borders, whereas motion estimation from tagging data at the myocardial walls and in thin-walled regions of the left-ventricular is less accurate due to the spatial resolution of the tagging grid [3]. In addition, some of the tagging images did not enclose the whole myocardium and some contained imaging artifacts, which resulted in strain artifacts towards the end of the cardiac cycle. Nevertheless, MEVIS-based motion estimates achieved the lowest error and thus represents a reliable reference for strain measures. This performance could be a result of their image term (2.2) that penalizes phase shifts in the Fourier domain instead of intensity values, an approach that is less affected by desaturation. The UPF approach also achieved a low error using multimodal integration and four-dimensional tracking to leverage the strengths of both modalities and improve temporal consistency [18]. Specific differences in motion and strain measures between MEVIS and other techniques were thoroughly discussed by Tobon-Gomez et al. [135].

Validation of strain

Using MEVIS as the tagging reference standard, we found no significant differences in measures of circumferential of radial and end-systolic strain. Validation studies have shown similar ($\pm 1\%$, [47, 5, 94]) or worse ($\pm 11\%$ for radial, [5]) biases between

cine feature tracking and tagging strain. However, these methods required manual contouring by an expert, whereas our method is fully-automatic. We found significant differences in strain rate measures between the two techniques that could be due to drift errors in the MEVIS implementation, i.e., errors that accumulate in sequential implementations in which motion is estimated frame-by-frame [135]. Although we did not observe considerable improvements in average end-point-error compared to tagging- and cine-based methods, an important advantage of our learning-based approach is the reduced computational complexity relative to the proposed MEVIS (1-2 h), IUCL (3-6 h), UPF (6 h) and INRIA (5 h) approaches [135]. Specifically, because once trained our network does not optimize for a specific test subject (i.e., it does not iterate on the cine-data to generate the desired output), centering, segmentation, and motion estimation for the entire cardiac cycle can be accomplished much faster (<2 min in CPU). In addition, DeepStrain was trained on a relatively small dataset and was evaluated on data from different institutions and vendors, therefore its accuracy relative to non-learning methods could substantially improve through training with larger cohorts or application of data shift correction strategies. Furthermore, a joint optimization of segmentation and motion estimation networks could potentially improve the robustness of the workflow to undersampled data [112].

3.6.2 Normal range of strain in healthy subjects

The application of myocardial strain to quantify abnormal deformation in disease requires accurate definition of normal ranges. However, previously reported normal ranges vary largely between modalities and techniques, particularly for radial end-systolic strain [3]. In this study we showed DeepStrain generated strain measures with narrow confidence interval in healthy subjects across three different datasets. Although direct comparison with the literature is difficult due to differences in the datasets, our strain measures generally agreed with several reported results. Specifically, circumferential strain is in agreement with values obtained from studies in healthy participants based on tagging (-16.6%, n=129) and speckle tracking echocardiography (-18%, n=265) datasets [141, 96], as well a recently proposed (-16.7%

basal, n=386) tagging-based deep learning method [29]. Our radial strain values are in agreement with those obtained using some tagging-based studies (26.5%, n=129; 23.8% basal, n=386)[29, 141], but are lower than most reported values [3]. This is a result of the smoothing regularization used during training to prevent overfitting. However, lowering the regularization without increasing the size of the training set would lead to increased end-point error and decreased precision. Strain rate measures derived with DeepStrain were also in good agreement with previous tagging-based studies [141].

3.6.3 Repeatability

In this study we also evaluated the intra-scanner repeatability of strain measures in 10 healthy subjects, an important aspect to consider when assessing the potential clinical utility of DeepStrain. Confidence intervals in circumferential and radial end-systolic strain were 0±1% and 0±3%, better than the intra-observer variability reported using feature tracking in 10 healthy adults [73]. A more recent study in 100 healthy individuals reported intra- and inter-observer repeatability for circumferential (ICC intra: 0.88, ICC inter: 0.88) and radial (0.82, 0.79), which were comparable to our results for circumferential (0.75) and radial (0.90) despite using only 10 subjects. Finally, our repeatability of strain rate measures was good to excellent, similar to that reported for healthy (n=20) and patient (n=60) populations [84]. Thus, without requiring expert operators, DeepStrain achieved better or equal repeatability compared to feature tracking methods.

3.6.4 Potential Clinical Applications

DeepStrain could be applied in a wide range of clinical applications, e.g., automated extraction of imaging phenotypes from large-scale databases [91]. Such phenotypes include global and regional strain, which are important measures in the setting of existing dysfunction with preserved ejection fraction [129]. DeepStrain generated measures of global strain and strain rate over the entire cardiac cycle from a cohort

of 100 subjects in <2 min. These results showed that radial early-diastolic strain rate was reduced in patients with hypertrophic cardiomyopathy and abnormal right ventricle, despite having a normal or increased left-ventricular ejection fraction. Decreased early-diastolic strain rate with normal ejection fraction is suggestive of subclinical left-ventricular diastolic dysfunction, which is in agreement with previous findings [16, 87].

At an individual level, we showed that in patients with myocardial infarction, polar segments with decreased circumferential strain matched myocardial regions with infarcted tissue. Further, we showed that the changes in regional strain due to myocardial infarction can be both diffuse and focal. These abnormalities could be used to discriminate dysfunctional from functional myocardium [41], or as inputs for downstream classification algorithms [158]. More generally, DeepStrain could be used to extract interpretable features (e.g., strain and strain rate) for deep learning diagnostic algorithms [160], which would make understanding of the pathophysiological basis of classification more attainable [60].

3.6.5 Study Limitations

A limitation of our study was the absence of important patient information (e.g., age), which would be needed for a more complete interpretation of our strain analysis results, for example to assess the differences in strain values found between the healthy subjects from the ACDC and CMAC datasets. Nevertheless, using publicly available data enables the scientific community to more easily reproduce our findings, and compare our results to other techniques. Another limitation was the absence of longitudinal analyses, i.e., longitudinal strain was not reported because it is normally derived from long-axis cine data not available in the training dataset. The size of the datasets is another potential limitation. The number of patients used for training is much smaller than the number of trainable parameters, potentially resulting in some degree of overfitting. To correct this, the training set for motion estimation could be expanded by validating the proposed segmentation network on more heterogeneous populations. While our repeatability results were promising despite testing in only

a small number of subjects, repeatability in patient populations was not evaluated. Further, reproducibility across sites and vendors was not assessed. Additionally, the accuracy of the motion estimates on patient populations with regional dysfunction was not evaluated, and we did not quantify the effect of dataset shift errors that might occur when applying our method to new datasets.

3.6.6 Conclusion

We developed an end-to-end learning-based workflow for strain analysis that is fast, operator-independent, and leverages real-world data instead of making explicit assumptions about myocardial tissue properties or geometry. This approach enabled us to derive strain measures from new data that were repeatable, and comparable to those derive from dedicated tagging data. These technical and practical attributes position DeepStrain as an excellent candidate for use in routine clinical studies or data-driven research.

Chapter 4

Prospective Study in Asymptomatic Young Adults

4.1 Introduction

Worldwide shifts towards sedentary lifestyles and suboptimal diets have led to increased prevalence of global obesity and obesity-related comorbidities such as hypertension [40, 1, 48, 92]. Each condition alone is a strong independent risk factor for type 2 diabetes mellitus [21, 2] and increased cardiovascular morbidity and mortality [66, 72, 25]. Clustering of obesity, hypertension, and type 2 diabetes mellitus could further elevate rates and severity of cardiovascular disease [138, 144], and is suspected to contribute to increased incidence of heart failure in the young [39]. Heart failure could be preceded by asymptomatic left ventricular diastolic dysfunction [68], a clinically silent disease whose development and transition to symptomatic heart failure are stimulated by obesity-related comorbidities [32, 61, 152, 24]. Echocardiography strain imaging studies have further demonstrated that asymptomatic left ventricular systolic dysfunction [121] can coexist with asymptomatic left ventricular diastolic dysfunction even when ejection fraction is preserved [79], and is associated with adverse long-term prognosis [52, 98]. Thus, strain imaging tools could provide a more accurate evaluation of left-ventricular function complementary to ejection fraction, and identification of both asymptomatic left-ventricular diastolic dysfunction and

asymptomatic left-ventricular systolic dysfunction at the early onset of non-specific symptoms using these tools could represent the earliest opportunity for diagnosis and treatment [108, 68].

In non-diagnostic or cases with inconclusive echocardiography findings, cardiac MR imaging plays an important complementary role and is often requested [108] to provide the most accurate and reproducible assessment of cardiac function, structure, and tissue properties [120]. The automated DeepStrain workflow proposed in this dissertation could quickly generate advanced strain readouts from clinically-standard cine images as well. Thus, the application of DeepStrain in routine cardiac MR studies would offer additional information about the underlying biomechanical motion, making cardiac MR a one-stop-shop for a more thorough characterization of disease trajectory towards the heart failure spectrum within a single examination [107, 14, 120, 136]. Although cine based strain analysis has been used to detect asymptomatic left-ventricular diastolic dysfunction and asymptomatic left-ventricular systolic dysfunction in older adults [82, 53, 69], few strain studies have focused on young adults, and detection of left-ventricular dysfunction in these subjects is potentially more difficult compared to older populations since they are less likely to have obvious clinical or imaging sings of cardiac disease during examination [151].

The aim of this study was to test DeepStrain as a sensitive tool for the detection of asymptomatic left-ventricular diastolic dysfunction and asymptomatic left-ventricular systolic dysfunction through characterization of myocardial strain in asymptotic young adults with overweight, hypertension, and type 2 diabetes mellitus.

4.2 Study Population

This prospective cross-sectional study was approved by the local medical ethical committee and conducted in accordance with the Declaration of Helsinki. Subjects aged 18-45 years were voluntarily recruited with public advertisements and signed informed consent before participation. Exclusion criteria were history or knowledge of cardiac disease, cardiac risk factors other than overweight, hypertension or type 2 diabetes

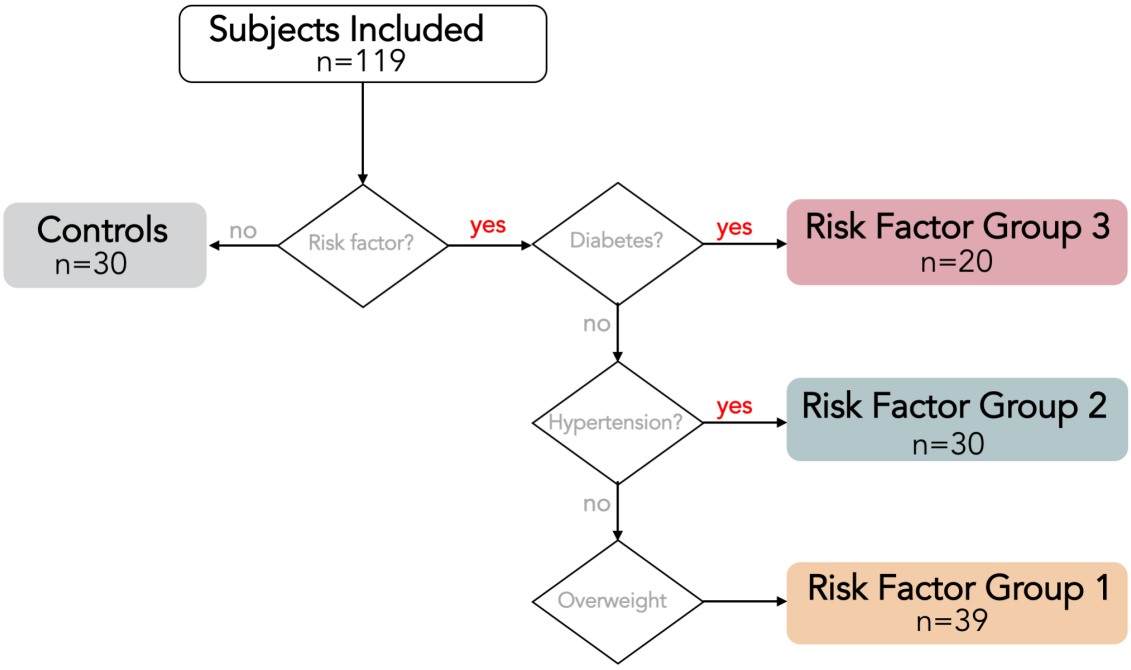

Figure 4-1: Risk Factor Group (RFG) classification decision tree.

mellitus, exercising $\geq$ 3 hours/week [109], and contraindications for cardiac MR. Presence of cardiac risk factors was checked using a medical questionnaire, and measurements of weight, blood pressure and hemoglobin A1c. Overweight was defined as body mass index $\geq$ 25 kg/m^2; hypertension was identified as either actively under clinical treatment or three consecutive blood pressure measurements $\geq$ 140/90 mmHg; type 2 diabetes mellitus was identified as either actively under treatment or a measure of hemoglobin A1c $\geq$ 48 mmol/mol measured prior to the cardiac MR exam.

All subjects were classified into one of the following groups: controls, risk factor group 1 (RFG1) including all overweight subjects with neither hypertension nor type 2 diabetes mellitus; RFG2 including all hypertensive subjects without type 2 diabetes mellitus, regardless of the presence or absence of additional overweight risk factor; RFG3 including all subjects with type 2 diabetes mellitus, regardless of the presence or absence of additional overweight or hypertension risk factors (Fig. 4-1).

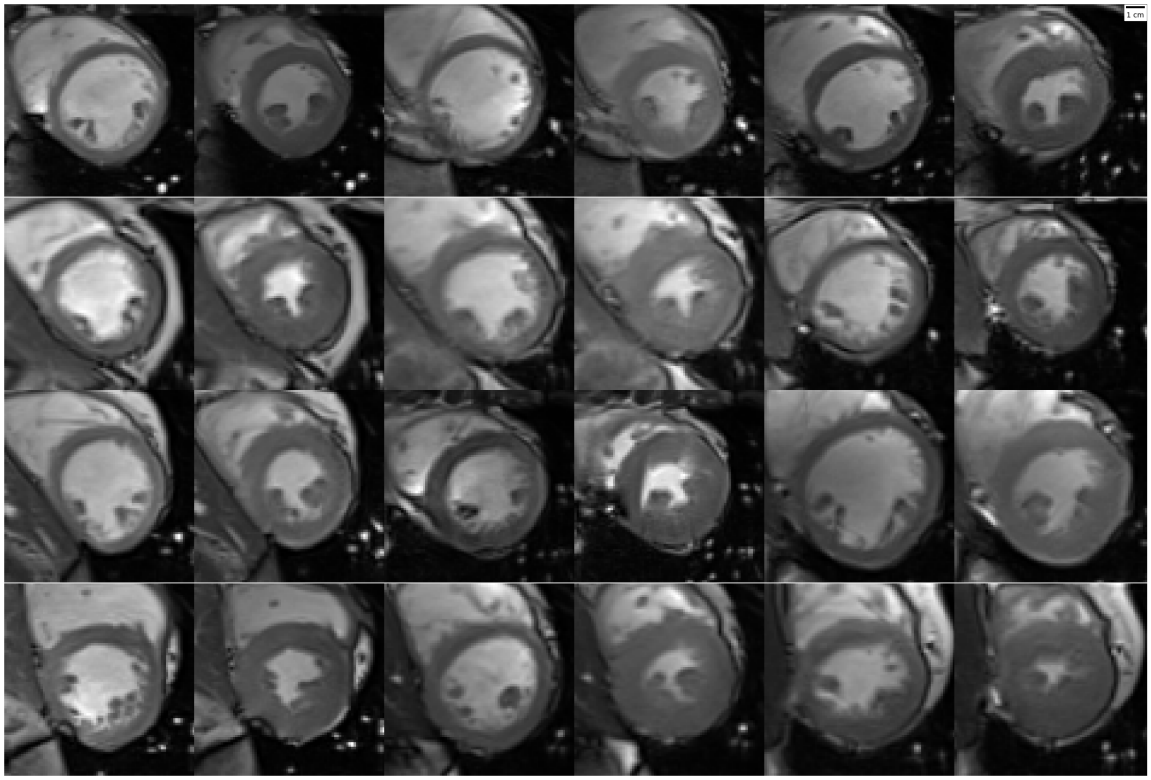

Figure 4-2: Representative cine images of 3 subjects for each risk factor group (RFG). Images are shown at mid-ventricle at both end-diastole (left) and end-systole (right). Top to bottom: controls, RFG1, RFG2, and RFG3.

4.2.1 Cardiac MR Data Acquisition

All subjects underwent cardiac MR with a 3 Tesla scanner (MAGNETOM Prisma, Siemens Healthineers, Erlangen, Germany) using a 60-element phased-array body coil. Experienced operators used a steady-state free precession sequence to acquire cine images using electrocardiographic gating during a series of breath-holds. Short-axis cines covering the entire heart from atria to ventricular apex were obtained. Each cine contained 25 cardiac phases with 6 mm slice thickness, and 4 mm interslice gaps. Short-axis acquisition parameters were: repetition time 38.92-44.52 ms, echo time 1.15-1.31 ms, flip angle 43-46°, field of view 300-453 mm×225-453 mm, acquisition matrix 256×192-256. Representative MR images of each RFG are shown in Fig. 4-2.

4.3 Method

4.3.1 DeepStrain Analysis

The final DeepStrain model described in Chapter 3 was used to derive the following parameters of circumferential and radial strain: global end-systolic strain, global systolic and early-diastolic strain rate, and regional end-systolic strain for each ventricular wall, i.e., anterior, septal, inferior, and lateral.

4.3.2 Statistical Analysis

Demographic variables were expressed as mean standard deviation, and strain-related variables as mean [95% confidence interval]. Variables were tested for normal distribution with a Shapiro-Wilk test and for homogeneity of variance using Levene's test. One-way analysis of variance (ANOVA) with post-hoc test by Bonferroni was used to examine differences among groups. Multivariate linear regression analysis was used to identify the independent association of the clinical variables body surface area, mean arterial pressure, and hemoglobin A1c on strain measures. A p-value < 0.05 was considered statistically significant. Data were analyzed using Python (version 3.5, Python Software Foundation, www.python.org).

4.4 Results

The study cohort consisted of 119 participants (35 $\pm$ 5 years, 50% male) including the control group with 30 subjects; RFG1 with 39 overweight subjects; RFG2 with 30 hypertensive subjects, including 13 (43%) with additional overweight; RFG3 with 20 type 2 diabetes mellitus subjects, including 11 (55%) with additional overweight, 1 (5%) with additional hypertension and 8 (40%) with both. Age, gender, and height were not significantly different between groups (Table 4.1), however, the mean heart rate of RFG3 was significantly higher compared to controls. Furthermore, there were no significant differences in left-ventricular mass, volumes, and ejection fraction between groups (supplementary Table A.2).

Table 4.1: Clinical characteristics of controls and risk factor groups (RFG).

	Control ($n = 30$)	RFG1 ($n = 39$)	RFG2 ($n = 30$)	RFG3 ($n = 20$)	ANOVA
Age (years)	34 ± 3	33 ± 6	36 ± 5	37 ± 5	0.051
Gender, male n (%)	16 (53)	19 (49)	14 (47)	10 (50)	0.964
Height (cm)	178 ± 7	175 ± 8	178 ± 10	174 ± 10	0.206
Weight (kg)	70 ± 9	94 ± 13‡	82 ± 16*	98 ± 19‡	<0.001
Body mass index (kg/m^2)	22 ± 2	30 ± 3‡	25 ± 5‡	32 ± 5‡	<0.001
Body surface area (m^2)	1.9 ± 0.2	2.1 ± 0.2‡	2.0 ± 0.2	2.2 ± 0.3‡	<0.001
Heart rate (bpm)	61 ± 9	67 ± 11	68 ± 8	77 ± 8‡	<0.001
Systolic blood pressure (mmHg)	117 ± 8	122 ± 8	138 ± 18‡	136 ± 12‡	<0.001
Diastolic blood pressure (mmHg)	78 ± 5	81 ± 6	92 ± 11‡	89 ± 8‡	<0.001
HbA1c (mmol/mol)	33 ± 3	34 ± 3	32 ± 3	61 ± 17‡	<0.001
Hypertension Medicine, n (%)		-	24 (80)	4 (20)	-

HbA1c: Hemoglobin A1c. ANOVA p value shows the one-way ANOVA test value between groups. Post-hoc test by Bonferroni: * $P < 0.05$; † $P < 0.01$; ‡ $P < 0.001$ versus controls.

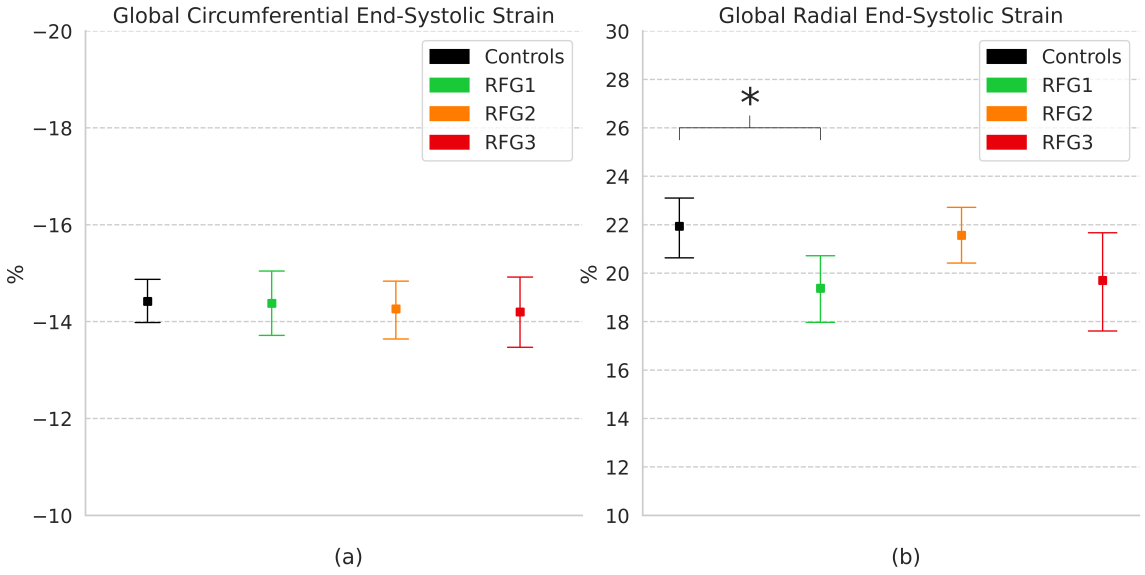

Figure 4-3: Global measures of (a) circumferential and (b) radial end-systolic strain in controls and risk factor groups (RFG). Data are reported as mean [95% confidence interval]. * $P < 0.05$ Post-hoc test by Bonferroni.

4.4.1 Global Strain and Strain Rate

Comparisons of global end-systolic strain showed that there were no significant differences in circumferential or radial strains between groups, except for a significantly decreased radial strain in RFG1 (19.4% [18.0 20.8]; p<0.05) relative to controls (21.9% [20.7 23.1]) (Fig. 4-3b and Table A.3).

Global circumferential early-diastolic strain rate was significantly reduced in RFG1

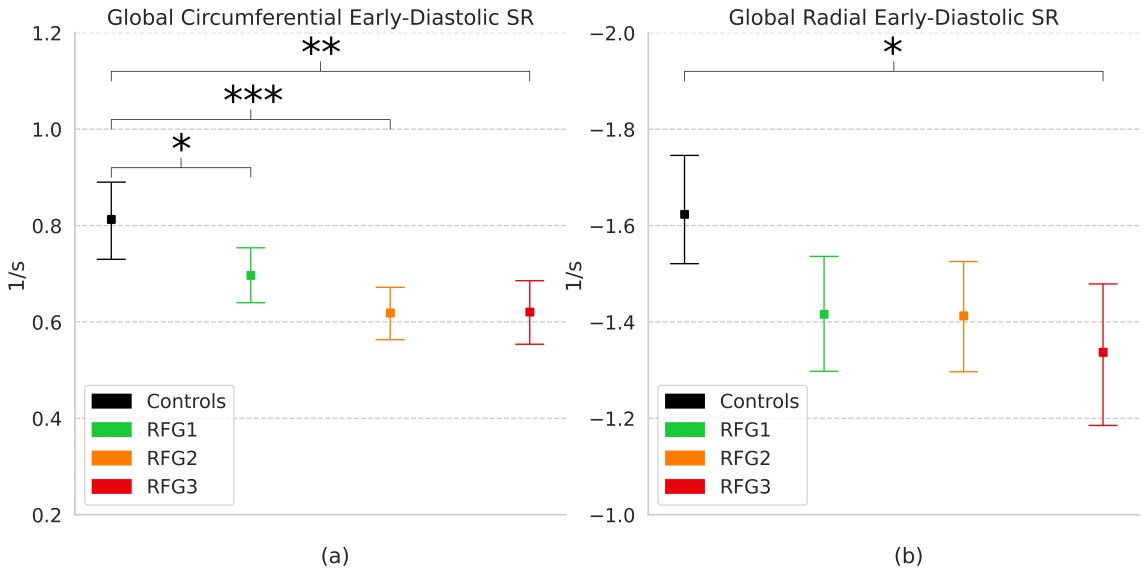

Figure 4-4: Global measures of (a) circumferential and (b) radial end-systolic strain rate (SR) in controls and risk factor groups (RFG). Data are reported as mean [95% confidence interval]. * $P < 0.05$; ** $P < 0.01$; *** $P < 0.001$ Post-hoc test by Bonferroni.

(0.70 s^{-1} [0.64 0.75]; p<0.05), RFG2 (0.62 s^{-1} [0.56 0.67]; p<0.001), and RFG3 (0.62 s^{-1} [0.55 0.68]; p<0.01) relative to controls (0.81 s^{-1} [0.74 0.89]) (Fig. 4-4a). Radial early-diastolic strain rate was also significantly reduced in RFG3 (-1.34 s^{-1} [-1.48 -1.19]; p<0.05) compared to controls (-1.62 s^{-1} [-1.74 -1.51]) (Fig. 4-4b). We found no significant differences between controls and RFGs in global systolic strain rate.

Body surface area correlated negatively with both circumferential and radial end-systolic strain (p<0.001; p<0.001), as well as early-diastolic strain rate (p<0.001; p=0.009) and systolic strain rate (p<0.001; p=0.002). Mean arterial pressure was a negative correlate of early-diastolic circumferential strain rate (p=0.007). We found no significant correlation between hemoglobin A1c and strain measures (Table 4.2).

4.4.2 Regional Strain

Regional comparisons of end-systolic strain by wall showed significantly lower circumferential strain in the septal wall of RFG1 (-13.7% [-14.2 -13.3]; p<0.001), RFG2 (-14.1% [-14.7 -13.5]; p<0.05), and RFG3 (-12.9% [-13.6 -12.1]; p<0.001) compared to controls (-15.1% [-15.6 -14.7]) (Fig. 4-5a and Table A.3). Notably, circumfer-

Table 4.2: Independent correlates of strain measures.

	End-Systolic Strain		Early-Diastolic Strain Rate		Systolic Strain Rate	
	β	*p-value*	*β*	*p-value*	*β*	*p-value*
Circumferential						
Body Surface Area	**-0.691**	<0.0001	**-0.067**	<0.0001	**-0.090**	<0.0001
Mean Arterial Pressure	-0.106	0.4712	**-0.046**	0.0072	0.020	0.3834
Hemoglobin A1c	0.168	0.2611	0.002	0.9014	0.024	0.3025
Radial						
Body Surface Area	**-1.404**	0.0002	**-0.088**	0.0090	**-0.112**	0.0026
Mean Arterial Pressure	0.407	0.2635	-0.023	0.4813	0.046	0.2074
Hemoglobin A1c	-0.016	0.9664	-0.013	0.6908	-0.018	0.6286

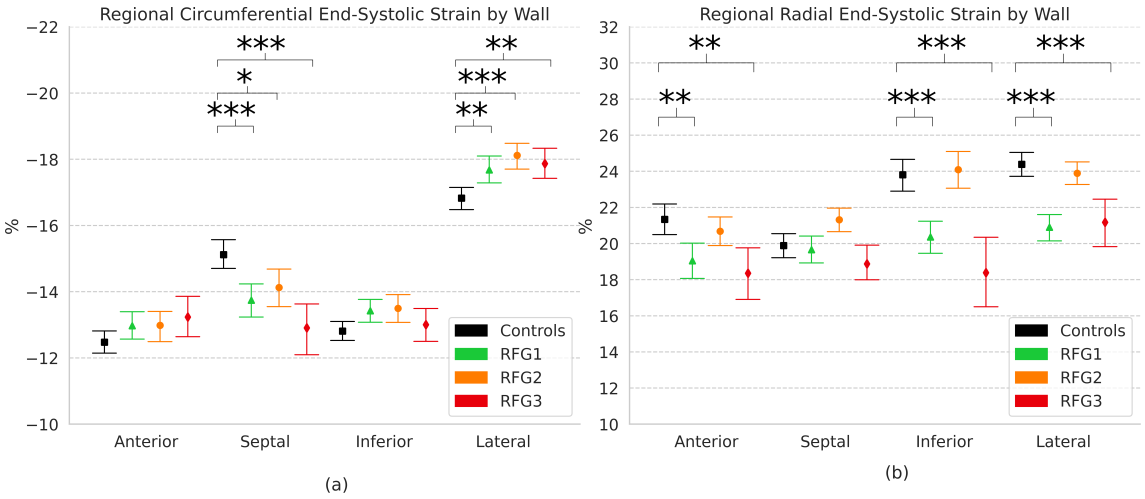

Figure 4-5: Regional measures of (a) circumferential and (b) radial end-systolic strain by wall (i.e., anterior, septal, inferior, and lateral) in controls and risk factor groups (RFG). Data are reported as mean [95% confidence interval].* $P < 0.05$; ** $P < 0.01$; *** $P < 0.001$ Post-hoc test by Bonferroni.

ential strain was significantly increased in the lateral wall of RFG1 (-17.7% [-18.1 -17.3]; p<0.01), RFG2 (-18.1% [-18.5 -17.7]; p<0.001), and RFG3 (-17.9% [-18.3 -17.4]; p<0.01) compared to controls (-16.8% [-17.2 -16.5]). Radial strain was decreased in the anterior (p<0.01), inferior (p<0.001), and lateral (p<0.001) walls of RFG1 and RFG3 compared to controls (Fig. 4-5b).

4.5 Discussion

Cardiac MR DeepStrain analysis of standard cine images identified evidence of asymptomatic left-ventricular diastolic dysfunction and asymptomatic left-ventricular sys-

tolic dysfunction in asymptomatic otherwise healthy, young subjects without knowledge or history of cardiovascular disease, but with at least one cardiovascular risk factor from overweight, hypertension, and type 2 diabetes mellitus. Despite comparable left-ventricular mass, volumes, and ejection fraction to controls, all RFGs showed impairment of left-ventricular circumferential early-diastolic strain rate as well as regional circumferential end-systolic strain. On multivariate linear regression analysis, body surface area correlated negatively with all strain measures, and mean arterial pressure was a negative correlate of circumferential early-diastolic strain rate.

4.5.1 Asymptomatic diastolic dysfunction

The link from obesity, hypertension, and type 2 diabetes mellitus to diastolic dysfunction has been well established in multiple echocardiography studies [54, 103, 106, 13, 147, 114, 130, 97, 166, 102, 104, 38]. Early-diastolic SR has also been used to identify asymptomatic left-ventricular diastolic dysfunction in older healthy adults (i.e., >45 years old) [146, 64]. Few studies have been applied to young adults, including obesity, severe obesity [149, 22], and type 2 diabetes mellitus [153, 43]. A recent study reported reduced early-diastolic strain rate in hypertension [126], and more recently, a progressive decline was demonstrated from lean to obese to type 2 diabetes mellitus in adolescents and young adults [43]. Liu et al. also showed progressive deterioration in cardiac MR-based circumferential and radial early-diastolic strain rate from controls to newly diagnosed to longstanding type 2 diabetes mellitus, corroborating previous findings about the cumulative effect of type 2 diabetes mellitus in early adulthood [64]. In this study we identified asymptomatic left ventricular diastolic dysfunction in all RFGs as indicated by significantly reduced early-diastolic circumferential and radial strain rate, and we found mean arterial pressure as independent predictor for circumferential early-diastolic strain rate, providing additional evidence of the existence of asymptomatic left-ventricular diastolic dysfunction even at a relatively young age. Our results indicate that DeepStrain could become a practical tool in the evaluation of underlying etiologies of suspected diastolic dysfunction, which in obesity-related comorbidities is challenging since coexistence of multiple risks factors

does not always yield uniform features but instead can present as multiple overlapping phenotypes [101].

4.5.2 Asymptomatic systolic dysfunction

The first asymptomatic manifestation of disease has traditionally believed to be diastolic dysfunction, as nearly all patients with systolic dysfunction already have some degree of concomitant diastolic dysfunction [116]. However, some authors suggested development of asymptomatic systolic dysfunction irrespective of diastolic dysfunction [28, 93], and reported that detection of systolic dysfunction using strain provides incremental prognostic value [52, 79, 98]. Multiple studies have reported reduced systolic strain with preserved ejection fraction in obesity and obesity-related risk factors using echocardiography [153, 145, 149] and more recently cardiac MR [82]. Although the majority have focused on global longitudinal strain, a recent study in hypertensive and heart failure patients with preserved ejection fraction reported that the predictive performance of global circumferential strain for heart failure was greater than longitudinal or radial strain [63]. Cardiac MR studies have also reported reduced circumferential strain in obese [53] and hypertensive subjects with type 2 diabetes mellitus [69], and in the latter all global strain measures were preserved in hypertensive subjects without type 2 diabetes mellitus, suggesting additional burden of type 2 diabetes mellitus to left-ventricular impairment [69]. In our study global measures of systolic function were reduced, albeit to a lesser extent than diastolic. Circumferential strain and systolic SR were comparable between groups, and radial strain was only significantly reduced in RFG1. This result may be explained by the small sample sizes and inability to achieve statistical significance in post-hoc analyses, but could also imply global measures are less sensitive than regional to subtle systolic dysfunction, as previously shown for mild hypertension [6]. Similarly, we found significant regional alterations in circumferential end-systolic strain in all RFGs characterized by reduced septal strain and increased lateral strain. Asymmetric septal hypertrophy due to afterload was long considered to be a consequence of increased wall stress on the septum compared to the free wall [50], and similar alterations in longitudi-

nal strain have also been reported in mild to moderate hypertension compared to controls, namely decreased values in the basal septal wall and increased values in the lateral wall [6]. A recent pig banding study similarly reported that longitudinal strain in chronic afterload was significantly more reduced in the septal wall relative to the lateral [115], and in a more recent animal banding study it was reported that decreases in septal circumferential strain during afterload augmentation was larger than in the free wall, a finding that could potentially be explained by a larger compensatory preload recruitment in the free wall compared to the septum [95]. Thus, our results demonstrate that regional analysis could provide additional insights in the early disease process.

4.5.3 Conclusion

In young adults with overweight, hypertension, and type 2 diabetes mellitus risks factors early-diastolic SR suggested asymptomatic left-ventricular diastolic dysfunction, and regional alterations in end-systolic strain indicated asymptomatic left-ventricular systolic dysfunction despite preserved ejection fraction. These changes could reflect early signs of cardiac disease, demonstrating that cardiac MR DeepStrain analysis could be a valuable tool in early detection and characterization of left-ventricular dysfunction in these populations.

Chapter 5

Concluding Remarks and Future Directions

Deep learning characterization of cardiovascular disease from cardiac MR data has clinical potential at many levels. The presented dissertation aimed to address most of the technical challenges related to cine strain analysis to demonstrate the potential at the quantification level. We showed that the sequential use of the VCN and CarSON networks accurately and automatically generates measures of cardiac function that are normally reported in standard cardiac MR protocols. CarMEN was proposed as a novel three-dimensional network for cardiac motion tracking and was later integrated with VCN and CarSON into the DeepStrain workflow, enabling accurate and precise measures of myocardial strain from cine data. We also showed that in healthy subjects these strain measures were repeatable and comparable to those derived from more complex tagging methods. In asymptomatic young adults with modern-age cardiovascular disease risk factors, these strain measures were more sensitive than standard metrics to detect left-ventricular dysfunction. This preliminary study in asymptomatic cardiac disease suggests DeepStrain is able to extract useful information not commonly reported in existing protocols using standard images, presenting cardiologists more advance readouts about the mechanical status of the heart. Furthermore, processing time from raw data to strain readouts took less than 3 minutes in a standard computer, and less than 2 seconds using a basic graphic

processing unit, which is dramatically faster than current technology (i.e., 1-6 hours). Thus, implementation of DeepStrain in routine cardiac MR protocols would speed up the radiology report and increase the overall value of the imaging study.

A summary of the technical developments that enabled us to deliver DeepStrain is provided in section 5.1. In section 5.2, we conclude this thesis by presenting potential and ongoing future innovations related to DeepStrain.

5.1 Summary of Technological Developments

In section 1.4, we summarized the various sources of error influencing strain measurements, and we argued that these sources could lead to inaccurate, imprecise, and ultimately implausibly wide ranges of normal strain. Several innovations were presented to provide a method with tagging-level accuracy and precision, yet using exclusively cine data.

In chapter 2, we developed a three-dimensional convolutional neural network to reduce overestimation of in-plane motion, a common limitation of two-dimensional techniques. In chapter 3, we designed an end-to-end learning-based workflow for automated myocardial tissue detection, labeling, and motion tracking. To accurately calibrate the design of the networks, we re-designed CarMEN such that all networks in the DeepStrain workflow had a common encoder-decoder architecture. This approach was key to efficiently inspecting potential sources of error from each task independently, and resulted in a more general architecture for cine data tasks. The presented design is also more optimal than conventional or off-the-shelf networks for other cardiac MR tasks, which we demonstrate at the conclusion of this thesis in section 5.2.3.

We additionally implemented an anatomical constrain to train CarMEN with the aim of minimizing the standard deviation in strain values within healthy individuals, as well as the differences between training and testing healthy subjects. We also identified the optimal balance between all the various motion constrains using simulated motion that was modeled from tagging data, enabling us to find a combination that

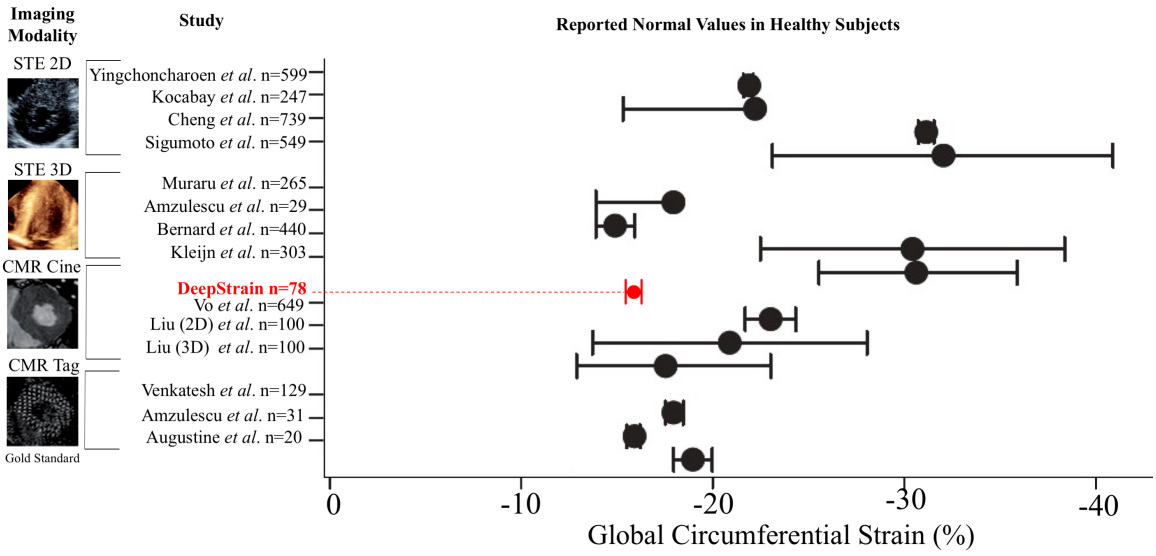

Figure 5-1: Reported normal (mean and 95% confidence interval) global circumferential strain in healthy subjects for different imaging modalities and methods compared to DeepStrain. Adapted from Amzulescu et al. [3].

generates both realistic and accurate motion and strain measures. The end result of the presented innovations can be seen in Fig. 5-1. In healthy subjects (n=78), DeepStrain generated precise measures of global circumferential strain from cine data that were comparable to those from tagging methods, evident by small width 95% confidence interval. The healthy subjects were imaged at different institutions using scanners from different vendors (n=78).

5.2 Future Innovation

5.2.1 Cardiac Mechanics in Humans and Animals

DeepStrain extension to right-ventricular strain

Non-learning techniques have primarily been applied to two-dimensional tracking of pixels along the myocardial borders in the past, mainly because tracking every pixel in the image or even just within the myocardium is very computationally demanding, and even more so in three dimensions. This means simultaneous tracking of both left and right ventricles is not easily achieved, and most commercial motion

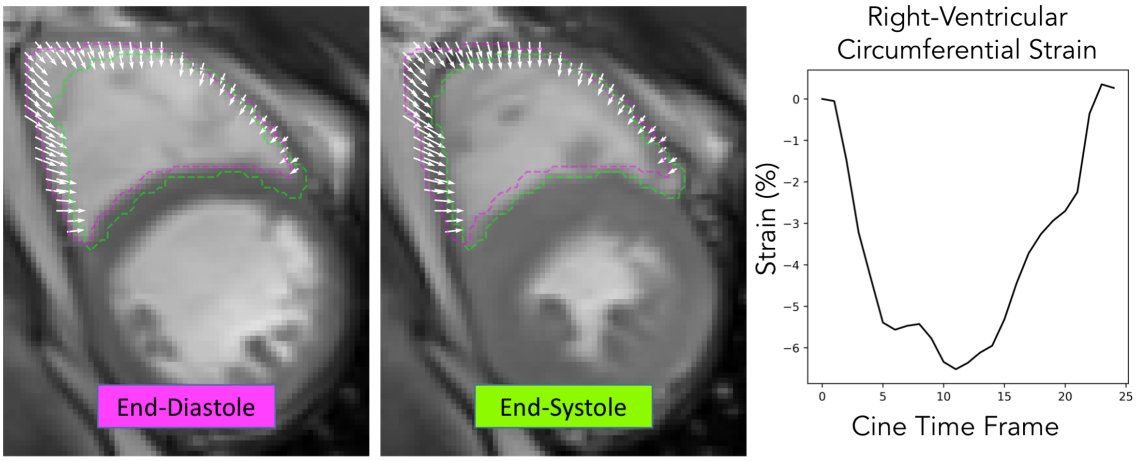

Figure 5-2: DeepStrain based right-ventricular strain

tracking applications have remained focused on the left ventricle. For this and other reasons, such as a complicated geometry and high load dependence, few studies have focused on right-ventricular morphological, functional, and strain analysis; yet right-ventricular function plays a critical role in the prediction of adverse cardiovascular outcomes [51]. In contrast, CarMEN was trained using both right- and left-ventricular anatomical constrains as described in (3.5), and can quickly track the motion of every voxel within the cine frame. Thus, the most immediate extension of DeepStrain is the evaluation of right-ventricular radial and circumferential strain. From an instrumentation perspective, improving scanner technology to increase the resolution of the cine data would provide more anatomically precise features, enabling more accurate motion tracking of an otherwise relatively thin wall. On the deep learning side, few labeled data of the right ventricle are currently available for training, limiting learning in both segmentation and motion tracking tasks. A data-centric approach should be taken here, i.e., DeepStrain should be trained with large amounts of data that in most cases contain high-quality labels of the right ventricle. Nevertheless, most of the challenges related to right-ventricular segmentation occur at the apex and base of the heart, therefore DeepStrain could be tested now for the evaluation of mid-ventricle right-ventricular strain (5-2).

DeepStrain extension to longitudinal strain

One of the main technical challenges of cine-based strain analysis is the anisotropic resolution of the data, which typically have 1.5 mm resolution in the x-y-plane and between 5-10 mm along the z direction. This complicates the design of three-dimensional neural networks by introducing ambiguity in what a convolution with a given kernel size k_x, k_y, k_z is actually learning. This is particularly problematic for motion-related tasks since these require accurately scaled motion features. One simple solution is resampling the input cine data to isotropic resolution, but this creates very large four-dimensional volumes which at the moment only few advanced graphical processing units can process. Further, it is not clear that we can accurately capture longitudinal motion (i.e., motion along the z direction) even from resampled data, which limits the ability of DeepStrain to evaluate longitudinal strain. From a data acquisition perspective, new sequences are pushing the resolution along the z dimension, and deep learning methods could accelerate this progress [71]. Another interesting approach is to leverage multi-task techniques to combine long axis (i.e., base-to-apex) and short axis (i.e., cross-sectional) images into a unified model of motion, enabling learning of a more complete model of three-dimensional cardiac motion.

CarSON extension to swine animal study

We have described four levels of clinical potential throughout this thesis, i.e., instrumentation, quantification, patient-cohort, and aggregate medicine (Fig. 1-9). DeepStrain could find applications in large animal models of cardiovascular disease as well, which are important for discerning the pathogenesis of human diseases with the purpose of developing novel therapeutic treatments [137]. For instance, Nguyen *et al.* used diffusion tensor CMR imaging in swine models of myocardial infarction to study the myocardial fiber architecture after injury [99], and other swine banding models of hypertension have been used to study the effects of increased afterload on myocardial hypertrophy and strain [115, 95]. One challenging aspect of applying deep learning methods to animal studies is that these studies are usually highly heterogeneous

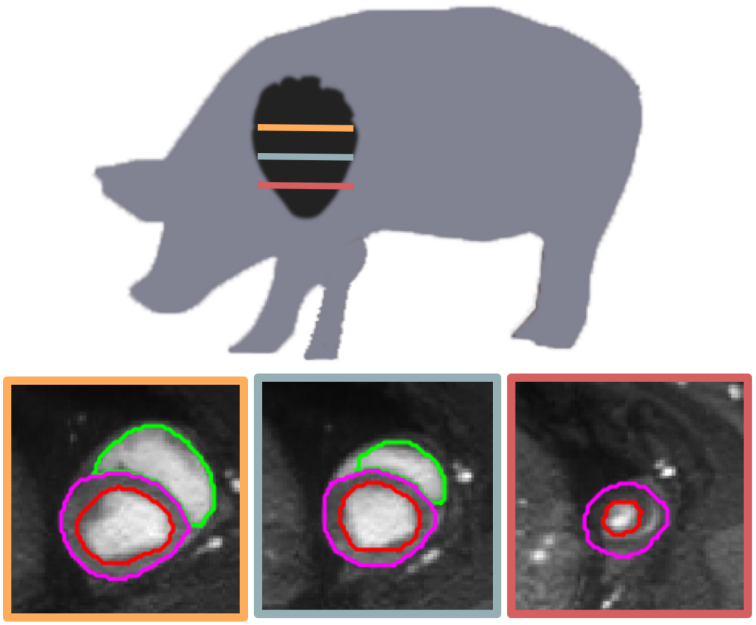

Figure 5-3: CarSON model trained with human data directly applied to automated tissue labeling of a pig's myocardium.

and include only a small number of animals. Thus, training a deep learning algorithm from scratch using only animal data would be very difficult. Interestingly, deep learning networks trained with human data could potentially be applied directly to animal studies. In collaboration with Maaike van den Boomen, PhD, and Christopher Nguyen, PhD, DeepStrain was tested in cine data from swines to enable automated myocardial segmentation and strain analysis. As shown in Fig. 5-3, CarSON is able to accurately delineate all cardiac structures. While these preliminary results require further validation, CarSON could at the very least generate initial contours that could then be manually corrected by an operator. More generally, transfer learning techniques requiring only a small set of animals for training could enable translation of human-based models to animal studies.

5.2.2 Positron Emission Tomography

PET is a noninvasive nuclear imaging modality that uses radioactive tracers to generate images with many clinical applications across the disease spectrum [140], including cardiovascular disease [7]. Patient-cohort level deep learning applications have been

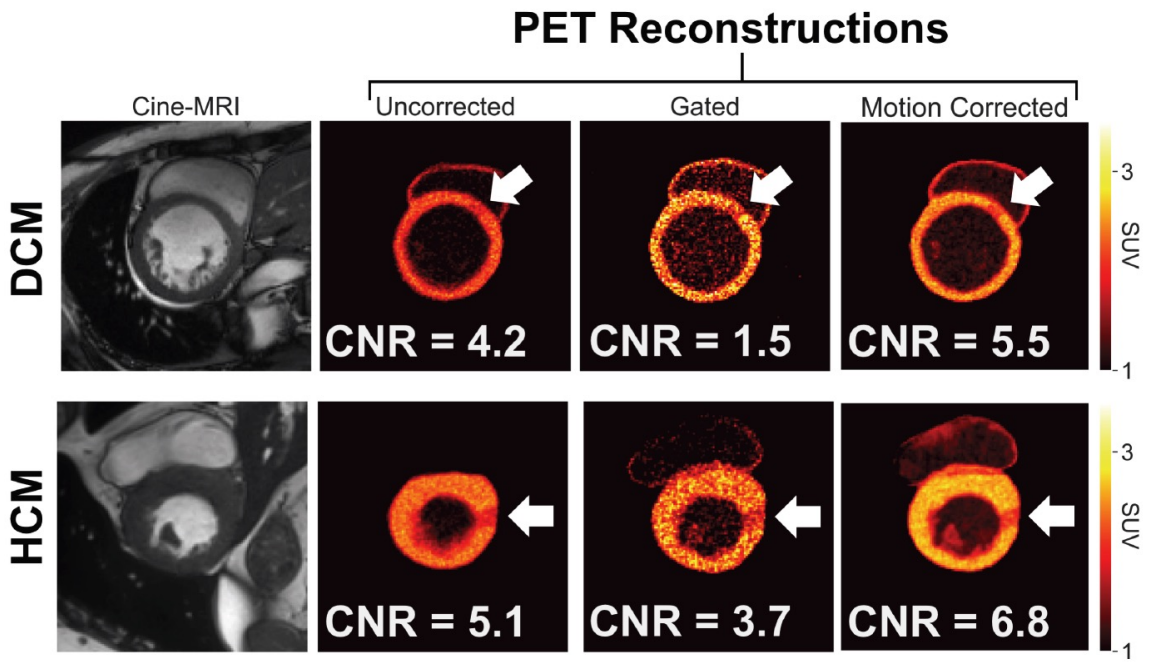

Figure 5-4: Effect of motion correction using CMR-based, CarMEN-derived motion estimates on lesion quantification in a patient with dilated (DCM) and hypertrophic (HCM) cardiomyopathy.

demonstrated for direct evaluation and classification of quantitative myocardial perfusion polar maps [59], and others have proposed novel combinations with MR features [58]. Integrated cardiac MR and PET scanners offer a unique set of features characterizing the myocardium from the most basic epigenetic level, to the most macro structural and functional level. Below we discus how DeepStrain could be translated to PET studies at the instrumentation and reading & recording levels, with a special emphasis on integrated scanners.

CarMEN extension to motion-aware PET correction

Image degradation due to cardiac motion remains a challenge that could hinder the value PET images in wider clinical practice. For PET data acquired simultaneously in scanners integrated with MR, CarMEN-based motion estimates could be used to minimize the unwanted effects of motion on images. As proof-of-concept we performed a simulation study. Cine data from subjects with dilated (n=10) and hypertrophic (n=10) cardiomyopathy were used to generate simulated PET acquisitions and re-

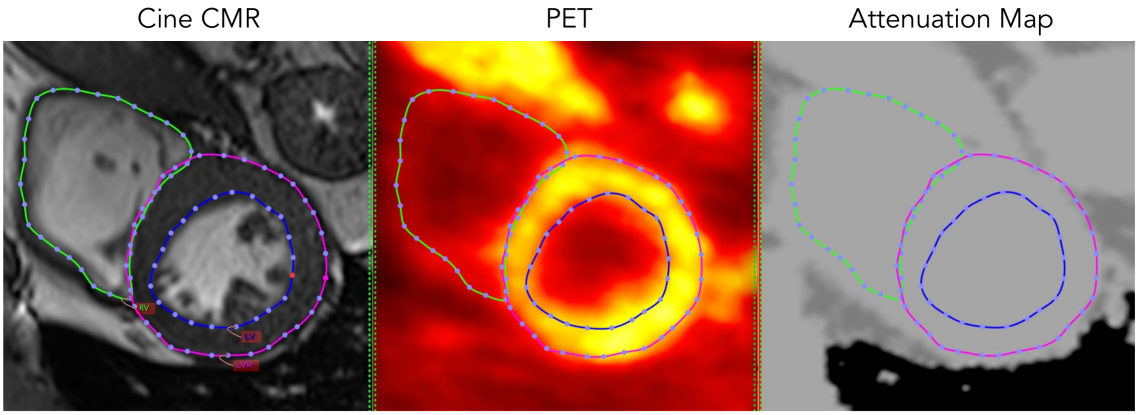

Figure 5-5: CarSON-enabled automated PET analysis.

constructions, and the CarMEN-derived motion estimates from these data were used for motion-aware reconstructions. Three reconstruction methods (i.e., uncorrected, gated and CarMEN-based motion corrected) were evaluated on their ability to quantify small perfusion lesions using the contrast-to-noise ratio metric. Relative to non-corrected reconstruction methods, the contrast-to-noise ratio of a lesion with 20% activity decrease is significantly ($p<0.01$) higher in the motion corrected images for both cardiomyopathy groups (Fig. 5-4). These preliminary results pave the way for a new DeepStrain-related motion correction approaches that, when integrated in the PET reconstruction pipeline, improve the quality of cardiac PET images. However, as discussed in section 5.2.1, this requires the accurate scaling of motion along all three dimensions that is matched to the resolution of the PET data - a challenging technical problem.

CarSON extension to automated PET analysis

Accurate segmentation of cardiac PET images is very challenging due to their lower spatial resolution and blurred myocardial wall borders boundaries. Several factors contribute to the overall ambiguity of what constitutes myocardial tissue in these images, including partial volume effects, respiratory and cardiac motion, and reconstruction noise and smoothing. In integrated scanners, cine delineation of the cardiac boundaries could enable more accurate and automated analysis of PET images. In

collaboration with David Izquierdo, PhD, and David Sosnovik, MD, we have begun to test the accuracy and usefulness of CarSON-based segmentations in cardiac PET imaging studies. The general workflow consists of first delineating the myocardial wall boundaries in the cine data, and then registering the PET images to the cine coordinates. As shown in 5-5, this is a promising approach that could be used to streamline the analysis pipeline. In principle, this information could also to be used to improve the 511 keV photon attenuation map derived from the MR data by offering a more accurate representation of the cardiac borders.

5.2.3 Evaluate Pulmonary Artery Area: a UK Biobank Study

We conclude our discussion with an example of application of DeepStrain at the patient-centric and aggregate medicine levels. This project is a collaboration with Adam Lee Johnson, M.D, Christopher Nguyen, PhD, and Rajeev Malhotra, MD. The application is aimed at discovering associations between genetic and vascular markers using the UK Biobank cardiovascular database, which includes more than 40,000 cases with various types of cardiac MR data. Specifically, we would like to apply CarSON (and in later studies CarMEN) to cardiac MR images of the pulmonary artery to evaluate its cross-sectional area. A subset of the database (<1,000 cases) is selected for development, and is manually labeled by operators following a set of annotation instructions.

Model-centric

From a model-centric perspective, we would like to tailor the design of CarSON to vessel segmentation. We will also compare its accuracy to that of nnUNet, an open-source tool that can effectively be used out-of-the-box and represents the state-of-the-art for several segmentation tasks [57].

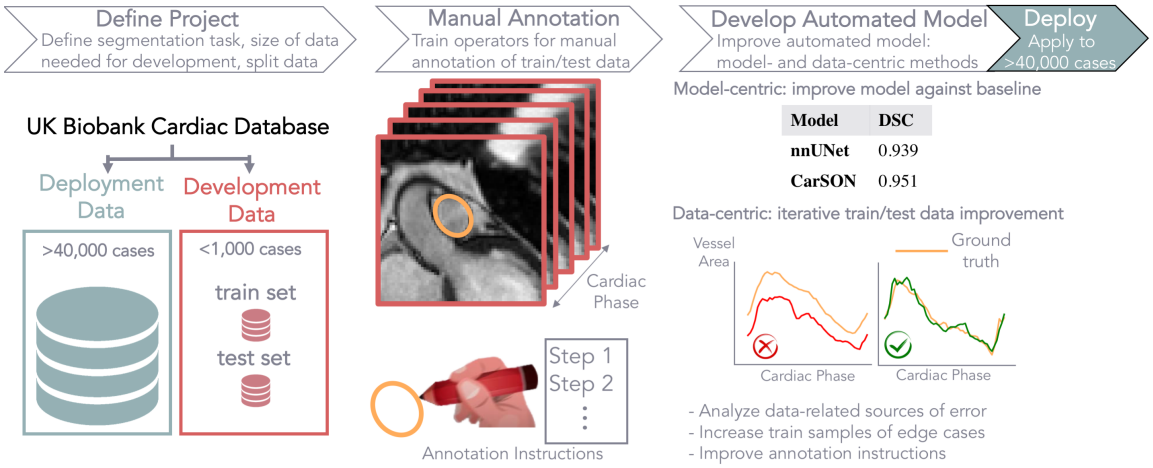

Figure 5-6: CarSON-enabled automated PET analysis.

Data-centric

We also take a data-centric approach by testing both CarSON and nnUNet to detect any potential difficult or edge cases. To achieve this, labeling and training is done through phases. In each phase, manual labeling is performed in subsets of the development data. Training and testing results are analyzed by both annotators and deep learning developers. The purpose of this iterative process is to improve the annotation instructions (if required), and to determine whether new data-augmentation approaches are needed.

As shown in Fig. 5-6, preliminary results suggest CarSON outperforms nnUNet in the vessel segmentation task. Once the final model is trained, CarSON can be applied to automatically and quickly evaluate several metrics of vessel morphology and function, and these can then be combined with genetic information available in database to provide a more complete picture of disease.

5.2.4 The Future of DeepStrain

We have shown DeepStrain has many *quantification level* applications: automated evaluation of myocardial morphology and function; automated, fast, accurate, and precise quantification of left-ventricular strain; automated PET analysis; and many more. Many of these applications could come together in a synergistic form and be

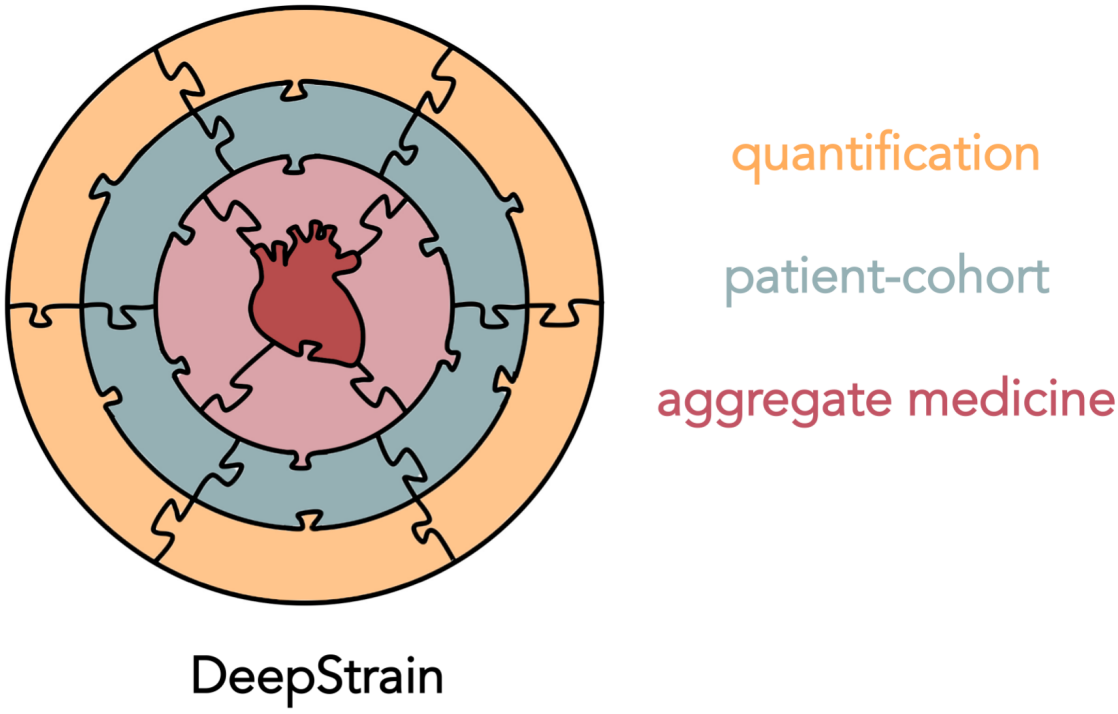

Figure 5-7: DeepStrain applications across different levels of cardiac medicine.

applied to large scale studies (Fig. 5-7). Indeed, the development and validation of this fast and automated tool paves the way for further innovations at other interesting levels. At the *patient-cohort level*, DeepStrain could quickly and automatically generate morphological, functional, and strain measures of cardiac mechanics from tens of thousands of subjects. Pulmonary artery area quantification in subjects in the UK Biobank was shown as an example in a current study. At a *aggregate medicine level*, ambitious undertakings to integrate clinical and laboratory results with DeepStrain and genetic features could elucidate novel therapeutic targets and research directions, making DeepStrain an ideal tool to characterize cardiac disease in the 21st century.

Appendix A

Tables

Table A.1: Metrics Comparison for the pediatric dataset. Data are medians, with interquartile ranges in parentheses. Image metrics included the Dice Similarity Coefficient (DSC), peak signal-to-noise ratio (PSNR), normalized cross-correlation (NCC), and the multiscale structural similarity metric index (MS-SSIM). High values of DSC, PSNR, NCC, and MS-SSIM are considered good. P values are relative to CarMEN and were obtained by using two-sided Wilcoxon signed-rank tests. ITK = Insight Segmentation and Registration Toolkit.

Elastix B-Spline	ITK B-Spline 1	ITK B-Spline 2	Diffeomorphic	Vampire	**CarMEN**
Dice Similarity Coefficient					
0.78 [0.75-0.81]; p=0.3423	0.77 [0.73-0.80]; p=0.7910	0.76 [0.71-0.80]; p=0.0005	0.74 [0.69-0.78]; p<0.0001	0.71 [0.58-0.80]; p<0.0001	0.77 [0.72-0.81]
Peak Signal-to-Noise Ratio					
27.2 [22.8-30.5]; p<0.0001	24.5 [22.9-27.3]; p<0.0001	26.1 [23.8-28.2]; p<0.0001	28.4 [25.2-32.4]; p<0.0001	38.2 [32.9-40.2]; p<0.0001	30.2 [27.5-33.8]
Normalized Cross-Correlation					
0.98 [0.97-0.98]; p<0.0001	0.96 [0.95-0.97]; p<0.0001	0.98 [0.98-0.98]; p<0.0001	0.98 [0.97-0.98]; p<0.0001	1.00 [0.99-1.00]; p<0.0001	0.99 [0.99-0.99]
Multiscale Structural Similarity Metric Index					
0.92 [0.89-0.95]; p<0.0001	0.89 [0.82-0.95]; p<0.0001	0.90 [0.86-0.94]; p<0.0001	0.94 [0.91-0.97]; p<0.0001	0.99 [0.99-1.00]; p<0.0001	0.96 [0.95-0.98]

Table A.2: Left ventricular parameters of controls and risk factor groups (RFG).

	Control	RFG 1	RFG 2	RFG 3	ANOVA
End-diastolic mass (g)	111 ± 24	119 ± 24	128 ± 28	123 ± 29	0.098
End-diastolic volume (ml)	176 ± 30	166 ± 31	166 ± 39	151 ± 34	0.091
End-systolic volume (ml)	68 ± 15	62 ± 19	63 ± 19	56 ± 15	0.167
Ejection fraction (%)	61 ± 5	62 ± 5	61 ± 5	62 ± 5	0.641
ANOVA *p* value shows the one-way ANOVA test value between groups.					

Table A.3: Left-ventricular strain measures of controls and risk factor groups (RFG) as mean [95% confidence interval].

	Control	RFG1	RFG2	RFG3	ANOVA
Circumferential					
Global End-Systolic Strain (%)	-14.4 [-14.9 -14.0]	-14.4 [-15.0 -13.7]	-14.3 [-14.8 -13.7]	-14.2 [-14.9 -13.5]	0.964
Global Early-Diastolic Strain Rate (s^{-1})	0.81 [0.74 0.89]	**0.70** [0.64 0.75]*	**0.62** [0.56 0.67]‡	**0.62** [0.55 0.68]†	<0.001
Global Systolic Strain Rate (s^{-1})	-1.00 [-1.09 -0.92]	-0.98 [-1.06 -0.90]	-0.99 [-1.10 -0.89]	-0.97 [-1.06 -0.88]	0.979
Regional End-Systolic Strain (%)					
Anterior	-12.5 [-12.8 -12.1]	-13.0 [-13.4 -12.5]	-13.0 [-13.4 -12.5]	-13.2 [-13.9 -12.6]	0.158
Septal	-15.1 [-15.6 -14.7]	**-13.7** [-14.2 -13.3]‡	**-14.1** [-14.7 -13.5]*	**-12.9** [-13.6 -12.1]‡	<0.001
Inferior	-12.8 [-13.1 -12.5]	-13.4 [-13.8 -13.1]	-13.5 [-13.9 -13.1]	-13.0 [-13.5 -12.5]	0.058
Lateral	-16.8 [-17.2 -16.5]	**-17.7** [-18.1 -17.3]†	**-18.1** [-18.5 -17.7]‡	**-17.9** [-18.3 -17.4]†	<0.001
Radial					
Global End-Systolic Strain (%)	21.9 [20.7 23.1]	**19.4** [18.0 20.8]*	21.6% [20.4 22.6]	19.7 [17.7 21.7]	0.021
Global Early-Diastolic Strain Rate (s^{-1})	-1.62 [-1.74 -1.51]	-1.42 [-1.54 -1.30]	-1.41 [-1.52 -1.30]	**-1.34** [-1.48 -1.19]*	0.021
Global Systolic Strain Rate (s^{-1})	1.51 [1.39 1.63]	1.32 [1.19 1.47]	1.52 [1.39 1.66]	1.34 [1.20 1.47]	0.088
Regional End-Systolic Strain (%)					
Anterior	21.3 [20.5 22.2]	**19.0** [18.1 20.0]†	20.7 [19.9 21.5]	**18.4** [16.9 19.7]†	<0.001
Septal	19.9 [19.2 20.6]	19.7 [18.9 20.4]	21.3 [20.6 22.0]	18.9 [17.9 19.9]	<0.001
Inferior	23.8 [22.9 24.8]	**20.4** [19.5 21.3]‡	24.1 [23.1 25.1]	**18.4** [16.5 20.3]‡	<0.001
Lateral	24.4 [23.7 25.0]	**20.9** [20.1 21.7]‡	23.9 [23.3 24.5]	**21.2** [19.8 22.6]‡	<0.001
ANOVA *p* value shows the one-way ANOVA test value between groups. Post-hoc test by Bonferroni: * $P < 0.05$; † $P < 0.01$; ‡ $P < 0.001$ versus controls.					

Bibliography

[1] Ashkan Afshin, Patrick John Sur, Kairsten A. Fay, Leslie Cornaby, Giannina Ferrara, Joseph S Salama, Erin C Mullany, Kalkidan Hassen Abate, Cristiana Abbafati, Zegeye Abebe, Mohsen Afarideh, Anju Aggarwal, Sutapa Agrawal, Tomi Akinyemiju, Fares Alahdab, Umar Bacha, Victoria F Bachman, Hamid Badali, Alaa Badawi, Isabela M Bensenor, Eduardo Bernabe, Sibhatu Kassa K Biadgilign, Stan H Biryukov, Leah E Cahill, Juan J Carrero, Kelly M. Cercy, Lalit Dandona, Rakhi Dandona, Anh Kim Dang, Meaza Girma Degefa, Maysaa El Sayed Zaki, Alireza Esteghamati, Sadaf Esteghamati, Jessica Fanzo, Carla Sofia e Sá Farinha, Maryam S Farvid, Farshad Farzadfar, Valery L. Feigin, Joao C Fernandes, Luisa Sorio Flor, Nataliya A. Foigt, Mohammad H Forouzanfar, Morsaleh Ganji, Johanna M. Geleijnse, Richard F Gillum, Alessandra C Goulart, Giuseppe Grosso, Idris Guessous, Samer Hamidi, Graeme J. Hankey, Sivadasanpillai Harikrishnan, Hamid Yimam Hassen, Simon I. Hay, Chi Linh Hoang, Masako Horino, Farhad Islami, Maria D. Jackson, Spencer L. James, Lars Johansson, Jost B. Jonas, Amir Kasaeian, Yousef Saleh Khader, Ibrahim A. Khalil, Young-Ho Khang, Ruth W Kimokoti, Yoshihiro Kokubo, G Anil Kumar, Tea Lallukka, Alan D Lopez, Stefan Lorkowski, Paulo A. Lotufo, Rafael Lozano, Reza Malekzadeh, Winfried März, Toni Meier, Yohannes A Melaku, Walter Mendoza, Gert B.M. Mensink, Renata Micha, Ted R Miller, Mojde Mirarefin, Viswanathan Mohan, Ali H Mokdad, Dariush Mozaffarian, Gabriele Nagel, Mohsen Naghavi, Cuong Tat Nguyen, Molly R Nixon, Kanyin L Ong, David M. Pereira, Hossein Poustchi, Mostafa Qorbani, Rajesh Kumar Rai, Christian Razo-García, Colin D Rehm, Juan A Rivera, Sonia Rodríguez-Ramírez, Gholamreza Roshandel, Gregory A Roth, Juan Sanabria, Tania G Sánchez-Pimienta, Benn Sartorius, Josef Schmidhuber, Aletta Elisabeth Schutte, Sadaf G. Sepanlou, Min-Jeong Shin, Reed J.D. Sorensen, Marco Springmann, Lucjan Szponar, Andrew L Thorne-Lyman, Amanda G Thrift, Mathilde Touvier, Bach Xuan Tran, Stefanos Tyrovolas, Kingsley Nnanna Ukwaja, Irfan Ullah, Olalekan A Uthman, Masoud Vaezghasemi, Tommi Juhani Vasankari, Stein Emil Vollset, Theo Vos, Giang Thu Vu, Linh Gia Vu, Elisabete Weiderpass, Andrea Werdecker, Tissa Wijeratne, Walter C Willett, Jason H Wu, Gelin Xu, Naohiro Yonemoto, Chuanhua Yu, and Christopher J L Murray. Health effects of dietary risks in 195 countries, 1990–2017: a systematic analysis for the Global Burden of Disease Study 2017. *The Lancet*, 393(10184):1958–1972, May 2019.

[2] Abdullah Algoblan, Mohammed Alalfi, and Muhammad Khan. Mechanism linking diabetes mellitus and obesity. *Diabetes, Metabolic Syndrome and Obesity: Targets and Therapy*, page 587, December 2014.

[3] M S Amzulescu, M De Craene, H Langet, A Pasquet, D Vancraeynest, A C Pouleur, J L Vanoverschelde, and B L Gerber. Myocardial strain imaging: review of general principles, validation, and sources of discrepancies. *European Heart Journal - Cardiovascular Imaging*, March 2019.

[4] Alexander Andreopoulos and John K Tsotsos. Efficient and generalizable statistical models of shape and appearance for analysis of cardiac mri. *Medical Image Analysis*, 12(3):335–357, 2008.

[5] Daniel Augustine, Adam J Lewandowski, Merzaka Lazdam, Aitzaz Rai, Jane Francis, Saul Myerson, Alison Noble, Harald Becher, Stefan Neubauer, Steffen E Petersen, and Paul Leeson. Global and regional left ventricular myocardial deformation measures by magnetic resonance feature tracking in healthy volunteers: comparison with tagging and relevance of gender. *Journal of Cardiovascular Magnetic Resonance*, 15(1):8, 2013.

[6] A Baltabaeva, M Marciniak, B Bijnens, J Moggridge, F He, T Antonios, G Macgregor, and G Sutherland. Regional left ventricular deformation and geometry analysis provides insights in myocardial remodelling in mild to moderate hypertension. *European Journal of Echocardiography*, page S1525216707002326, October 2007.

[7] Frank M Bengel, Takahiro Higuchi, Mehrbod S Javadi, and Riikka Lautamäki. Cardiac positron emission tomography. *Journal of the American College of Cardiology*, 54(1):1–15, 2009.

[8] E. J. Benjamin, P. Muntner, A. Alonso, M. S. Bittencourt, C. W. Callaway, A. P. Carson, A. M. Chamberlain, A. R. Chang, S. Cheng, S. R. Das, F. N. Delling, L. Djousse, M. Elkind, J. F. Ferguson, M. Fornage, L. C. Jordan, S. S. Khan, B. M. Kissela, K. L. Knutson, and T. W. Kwan. Heart disease and stroke statistics-2019 update: A report from the american heart association. *Circulation*, 139(10).

[9] Mitchel Benovoy, Matthew Jacobs, Farida Cheriet, Nagib Dahdah, Andrew E. Arai, and Li-Yueh Hsu. Automatic nonrigid motion correction for quantitative first-pass cardiac MR perfusion imaging. In *2015 IEEE 12th International Symposium on Biomedical Imaging (ISBI)*, pages 1588–1591, Brooklyn, NY, USA, April 2015. IEEE.

[10] O. Bernard, A. Lalande, C. Zotti, F. Cervenansky, X. Yang, P. A. Heng, I. Cetin, K. Lekadir, O. Camara, M. A. Gonzalez Ballester, G. Sanroma, S. Napel, S. Petersen, G. Tziritas, E. Grinias, M. Khened, V. A. Kollerathu, G. Krishnamurthi, M. M. Rohé, X. Pennec, M. Sermesant, F. Isensee, P. Jäger, K. H. Maier-Hein, P. M. Full, I. Wolf, S. Engelhardt, C. F. Baumgartner, L. M. Koch,

J. M. Wolterink, I. Išgum, Y. Jang, Y. Hong, J. Patravali, S. Jain, O. Humbert, and P. M. Jodoin. Deep learning techniques for automatic mri cardiac multi-structures segmentation and diagnosis: Is the problem solved? *IEEE Transactions on Medical Imaging*, 37(11):2514–2525, 2018.

[11] Olivier Bernard, Alain Lalande, Clement Zotti, Frederick Cervenansky, Xin Yang, Pheng-Ann Heng, Irem Cetin, Karim Lekadir, Oscar Camara, Miguel Angel Gonzalez Ballester, Gerard Sanroma, Sandy Napel, Steffen Petersen, Georgios Tziritas, Elias Grinias, Mahendra Khened, Varghese Alex Kollerathu, Ganapathy Krishnamurthi, Marc-Michel Rohe, Xavier Pennec, Maxime Sermesant, Fabian Isensee, Paul Jager, Klaus H. Maier-Hein, Peter M. Full, Ivo Wolf, Sandy Engelhardt, Christian F. Baumgartner, Lisa M. Koch, Jelmer M. Wolterink, Ivana Isgum, Yeonggul Jang, Yoonmi Hong, Jay Patravali, Shubham Jain, Olivier Humbert, and Pierre-Marc Jodoin. Deep Learning Techniques for Automatic MRI Cardiac Multi-Structures Segmentation and Diagnosis: Is the Problem Solved? *IEEE Transactions on Medical Imaging*, 37(11):2514–2525, November 2018.

[12] Maria Baldeon Calisto and Susana K Lai-Yuen. Adaen-net: An ensemble of adaptive 2d–3d fully convolutional networks for medical image segmentation. *Neural Networks*, 126:76–94, 2020.

[13] Davinder S. Chadha, Nidhi Gupta, Kashish Goel, Ravindra M. Pandey, Dimple Kondal, R.K. Ganjoo, and Anoop Misra. Impact of Obesity on the Left Ventricular Functions and Morphology of Healthy Asian Indians. *Metabolic Syndrome and Related Disorders*, 7(2):151–158, April 2009.

[14] Mohammed A. Chamsi-Pasha, Yang Zhan, Dany Debs, and Dipan J. Shah. CMR in the Evaluation of Diastolic Dysfunction and Phenotyping of HFpEF. *JACC: Cardiovascular Imaging*, 13(1):283–296, January 2020.

[15] Pingjun Chen, Xiao Chen, Eric Z. Chen, Hanchao Yu, Terrence Chen, and Shanhui Sun. Anatomy-Aware Cardiac Motion Estimation. *arXiv:2008.07579 [cs, eess]*, August 2020. arXiv: 2008.07579.

[16] Shi Chen, Jiansong Yuan, Shubin Qiao, Fujian Duan, Jiafen Zhang, and Hao Wang. Evaluation of Left Ventricular Diastolic Function by Global Strain Rate Imaging in Patients with Obstructive Hypertrophic Cardiomyopathy: A Simultaneous Speckle Tracking Echocardiography and Cardiac Catheterization Study. *Echocardiography*, 31(5):615–622, May 2014.

[17] Nathalie Conrad, Andrew Judge, Jenny Tran, Hamid Mohseni, Deborah Hedgecott, Abel Perez Crespillo, Moira Allison, Harry Hemingway, John G Cleland, John JV McMurray, et al. Temporal trends and patterns in heart failure incidence: a population-based study of 4 million individuals. *The Lancet*, 391(10120):572–580, 2018.

[18] Mathieu De Craene, Gemma Piella, Oscar Camara, Nicolas Duchateau, Etelvino Silva, Adelina Doltra, Jan D'hooge, Josep Brugada, Marta Sitges, and Alejandro F. Frangi. Temporal diffeomorphic free-form deformation: Application to motion and strain estimation from 3D echocardiography. *Medical Image Analysis*, 16(2):427–450, February 2012.

[19] Mathieu De Craene, Gemma Piella, Oscar Camara, Nicolas Duchateau, Etelvino Silva, Adelina Doltra, Jan D'hooge, Josep Brugada, Marta Sitges, and Alejandro F Frangi. Temporal diffeomorphic free-form deformation: Application to motion and strain estimation from 3d echocardiography. *Medical image analysis*, 16(2):427–450, 2012.

[20] Bob D. de Vos, Floris F. Berendsen, Max A. Viergever, Marius Staring, and Ivana Išgum. End-to-End Unsupervised Deformable Image Registration with a Convolutional Neural Network. *arXiv:1704.06065 [cs]*, 10553:204–212, 2017. arXiv: 1704.06065.

[21] Vincent G. DeMarco, Annayya R. Aroor, and James R. Sowers. The pathophysiology of hypertension in patients with obesity. *Nature Reviews Endocrinology*, 10(6):364–376, June 2014.

[22] V Di Bello, F Santini, A Di Cori, A Pucci, C Palagi, M G Delle Donne, M Giannetti, E Talini, C Nardi, G Pedrizzetti, P Fierabracci, P Vitti, A Pinchera, and A Balbarini. Relationship between preclinical abnormalities of global and regional left ventricular function and insulin resistance in severe obesity: a Color Doppler Imaging Study. *International Journal of Obesity*, 30(6):948–956, June 2006.

[23] Peng Dong, Benjamin Provencher, Nabil Basim, Nicolas Piché, and Mike Marsh. Forget About Cleaning up Your Micrographs: Deep Learning Segmentation Is Robust to Image Artifacts. *Microscopy and Microanalysis*, pages 1–2, July 2020.

[24] Justin B. Echouffo-Tcheugui, Sebhat Erqou, Javed Butler, Clyde W. Yancy, and Gregg C. Fonarow. Assessing the Risk of Progression From Asymptomatic Left Ventricular Dysfunction to Overt Heart Failure. *JACC: Heart Failure*, 4(4):237–248, April 2016.

[25] Thomas R. Einarson, Annabel Acs, Craig Ludwig, and Ulrik H. Panton. Prevalence of cardiovascular disease in type 2 diabetes: a systematic literature review of scientific evidence from across the world in 2007–2017. *Cardiovascular Diabetology*, 17(1):83, December 2018.

[26] Tilman Emrich, Moritz Halfmann, U Joseph Schoepf, and Karl-Friedrich Kreitner. Cmr for myocardial characterization in ischemic heart disease: state-of-the-art and future developments. *European Radiology Experimental*, 5(1):1–13, 2021.

[27] Laura Ernande, Cyrille Bergerot, Nicolas Girerd, Hélène Thibault, Einar Skulstad Davidsen, Pierre Gautier Pignon-Blanc, Camille Amaz, Pierre Croisille, Marc L. De Buyzere, Ernst R. Rietzschel, Thierry C. Gillebert, Philippe Moulin, Mikhael Altman, and Geneviève Derumeaux. Longitudinal Myocardial Strain Alteration Is Associated with Left Ventricular Remodeling in Asymptomatic Patients with Type 2 Diabetes Mellitus. *Journal of the American Society of Echocardiography*, 27(5):479–488, May 2014.

[28] Laura Ernande, Cyrille Bergerot, Ernst R. Rietzschel, Marc L. De Buyzere, Hélène Thibault, Pierre Gautier PignonBlanc, Pierre Croisille, Michel Ovize, Laure Groisne, Philippe Moulin, Thierry C. Gillebert, and Geneviève Derumeaux. Diastolic Dysfunction in Patients with Type 2 Diabetes Mellitus: Is It Really the First Marker of Diabetic Cardiomyopathy? *Journal of the American Society of Echocardiography*, 24(11):1268–1275.e1, November 2011.

[29] Edward Ferdian, Avan Suinesiaputra, Kenneth Fung, Nay Aung, Elena Lukaschuk, Ahmet Barutcu, Edd Maclean, Jose Paiva, Stefan K. Piechnik, Stefan Neubauer, Steffen E. Petersen, and Alistair A. Young. Fully Automated Myocardial Strain Estimation from Cardiovascular MRI–tagged Images Using a Deep Learning Framework in the UK Biobank. *Radiology: Cardiothoracic Imaging*, 2(1):e190032, February 2020.

[30] Philipp Fischer, Alexey Dosovitskiy, Eddy Ilg, Philip Häusser, Caner Hazırbaş, Vladimir Golkov, Patrick Van der Smagt, Daniel Cremers, and Thomas Brox. Flownet: Learning optical flow with convolutional networks. *arXiv preprint arXiv:1504.06852*, 2015.

[31] National Center for Health Statistics, Centers for Disease Control, Prevention (CDC), et al. Leading causes of death, 1900-1998. cdc web site, 2012.

[32] Aaron M. From, Christopher G. Scott, and Horng H. Chen. The Development of Heart Failure in Patients With Diabetes Mellitus and Pre-Clinical Diastolic Dysfunction. *Journal of the American College of Cardiology*, 55(4):300–305, January 2010.

[33] Jérôme Garot, David A. Bluemke, Nael F. Osman, Carlos E. Rochitte, Elliot R. McVeigh, Elias A. Zerhouni, Jerry L. Prince, and João A. C. Lima. Fast Determination of Regional Myocardial Strain Fields From Tagged Cardiac Images Using Harmonic Phase MRI. *Circulation*, 101(9):981–988, March 2000.

[34] Mihai Gheorghiade and Robert O Bonow. Chronic heart failure in the united states: a manifestation of coronary artery disease. *Circulation*, 97(3):282–289, 1998.

[35] Fabian Gigengack, Lars Ruthotto, Martin Burger, Carsten H Wolters, Xiaoyi Jiang, and Klaus P Schafers. Motion correction in dual gated cardiac pet using mass-preserving image registration. *IEEE transactions on medical imaging*, 31(3):698–712, 2011.

[36] Holly C Gooding, Samuel S Gidding, Andrew E Moran, Nicole Redmond, Norrina B Allen, Fida Bacha, Trudy L Burns, Janet M Catov, Michael A Grandner, Kathleen Mullan Harris, et al. Challenges and opportunities for the prevention and treatment of cardiovascular disease among young adults: Report from a national heart, lung, and blood institute working group. *Journal of the American Heart Association*, 9(19):e016115, 2020.

[37] Neil L. Greenberg, Michael S. Firstenberg, Peter L. Castro, Michael Main, Agnese Travaglini, Jill A. Odabashian, Jeanne K. Drinko, L. Leonardo Rodriguez, James D. Thomas, and Mario J. Garcia. Doppler-Derived Myocardial Systolic Strain Rate Is a Strong Index of Left Ventricular Contractility. *Circulation*, 105(1):99–105, January 2002.

[38] Elena-Daniela Grigorescu, Cristina-Mihaela Lacatusu, Mariana Floria, Bogdan-Mircea Mihai, Ioana Cretu, and Laurentiu Sorodoc. Left Ventricular Diastolic Dysfunction in Type 2 Diabetes—Progress and Perspectives. *Diagnostics*, 9(3):121, September 2019.

[39] Amy Groenewegen, Frans H. Rutten, Arend Mosterd, and Arno W. Hoes. Epidemiology of heart failure. *European Journal of Heart Failure*, 22(8):1342–1356, August 2020.

[40] Regina Guthold, Gretchen A Stevens, Leanne M Riley, and Fiona C Bull. Worldwide trends in insufficient physical activity from 2001 to 2016: a pooled analysis of 358 population-based surveys with 1·9 million participants. *The Lancet Global Health*, 6(10):e1077–e1086, October 2018.

[41] Marco J.W Götte, Albert C van Rossum, Jos W.R Twisk, Joost P.A Kuijer, J.Tim Marcus, and Cees A Visser. Quantification of regional contractile function after infarction: strain analysis superior to wall thickening analysis in discriminating infarct from remote myocardium. *Journal of the American College of Cardiology*, 37(3):808–817, March 2001.

[42] Hassan Haji-Valizadeh, Rui Guo, Selcuk Kucukseymen, Amanda Paskavitz, Xiaoying Cai, Jennifer Rodriguez, Patrick Pierce, Beth Goddu, Daniel Kim, Warren Manning, et al. Highly accelerated free-breathing real-time phase contrast cardiovascular mri via complex-difference deep learning. *Magnetic Resonance in Medicine*, 2021.

[43] Jessica E Haley, Gao Zhiqian, Khoury R Philip, Madsen L Nicolas, Kimball R Thomas, Dolan M Lawrence, and Urbina M Elaine. Reduction in myocardial strain is evident in adolescents and young adults with obesity and type 2 diabetes. *Pediatric Diabetes*, 21(2):243–250, March 2020.

[44] Kerstin Hammernik, Teresa Klatzer, Erich Kobler, Michael P Recht, Daniel K Sodickson, Thomas Pock, and Florian Knoll. Learning a variational network for reconstruction of accelerated mri data. *Magnetic resonance in medicine*, 79(6):3055–3071, 2018.

[45] K. Hammouda, F. Khalifa, H. Abdeltawab, A. Elnakib, G. A. Giridharan, M. Zhu, C. K. Ng, S. Dassanayaka, M. Kong, H. E. Darwish, T. M. A. Mohamed, S. P. Jones, and A. El-Baz. A New Framework for Performing Cardiac Strain Analysis from Cine MRI Imaging in Mice. *Scientific Reports*, 10(1):7725, December 2020.

[46] Tarek N Hanna, Matthew E Zygmont, Ryan Peterson, David Theriot, Haris Shekhani, Jamlik-Omari Johnson, and Elizabeth A Krupinski. The effects of fatigue from overnight shifts on radiology search patterns and diagnostic performance. *Journal of the American College of Radiology*, 15(12):1709–1716, 2018.

[47] David M. Harrild, Yuchi Han, Tal Geva, Jing Zhou, Edward Marcus, and Andrew J. Powell. Comparison of cardiac MRI tissue tracking and myocardial tagging for assessment of regional ventricular strain. *The International Journal of Cardiovascular Imaging*, 28(8):2009–2018, December 2012.

[48] Rohana N. Haththotuwa, Chandrika N. Wijeyaratne, and Upul Senarath. Worldwide epidemic of obesity. In *Obesity and Obstetrics*, pages 3–8. Elsevier, 2020.

[49] Paul A Heidenreich, Justin G Trogdon, Olga A Khavjou, Javed Butler, Kathleen Dracup, Michael D Ezekowitz, Eric Andrew Finkelstein, Yuling Hong, S Claiborne Johnston, Amit Khera, et al. Forecasting the future of cardiovascular disease in the united states: a policy statement from the american heart association. *Circulation*, 123(8):933–944, 2011.

[50] Ming K. Heng, Ronald F. Janz, and Jean Jobin. Estimation of regional stress in the left ventricular septum and free wall: An echocardiographic study suggesting a mechanism for asymmetric septal hypertrophy. *American Heart Journal*, 110(1):84–90, July 1985.

[51] Brian D Hoit. Right ventricular strain comes of age, 2018.

[52] David J Holland, Thomas H Marwick, Brian A Haluska, Rodel Leano, Matthew D Hordern, James L Hare, Zhi You Fang, Johannes B Prins, and Tony Stanton. Subclinical LV dysfunction and 10-year outcomes in type 2 diabetes mellitus. *Heart*, 101(13):1061–1066, July 2015.

[53] Rami Homsi, Seyrani Yuecel, Ulrike Schlesinger-Irsch, Michael Meier-Schroers, Daniel Kuetting, Julian Luetkens, Alois Sprinkart, Hans H. Schild, and Daniel K Thomas. Epicardial fat, left ventricular strain, and T1-relaxation times in obese individuals with a normal ejection fraction. *Acta Radiologica*, 60(10):1251–1257, October 2019.

[54] Gianluca Iacobellis, Maria Cristina Ribaudo, Gaetano Leto, Alessandra Zappaterreno, Elio Vecci, Umberto Di Mario, and Frida Leonetti. Influence of Excess

Fat on Cardiac Morphology and Function: Study in Uncomplicated Obesity. *Obesity Research*, 10(8):767–773, August 2002.

[55] El-Sayed H Ibrahim, V Emre Arpinar, L Tugan Muftuler, Jadranka Stojanovska, Andrew S Nencka, and Kevin M Koch. Cardiac functional magnetic resonance imaging at 7t: Image quality optimization and ultra-high field capabilities. *World Journal of Radiology*, 12(10):231, 2020.

[56] Fabian Isensee, Paul F Jaeger, Peter M Full, Ivo Wolf, Sandy Engelhardt, and Klaus H Maier-Hein. Automatic cardiac disease assessment on cine-mri via time-series segmentation and domain specific features. In *International workshop on statistical atlases and computational models of the heart*, pages 120–129. Springer, 2017.

[57] Fabian Isensee, Paul F Jaeger, Simon AA Kohl, Jens Petersen, and Klaus H Maier-Hein. nnu-net: a self-configuring method for deep learning-based biomedical image segmentation. *Nature Methods*, 18(2):203–211, 2021.

[58] Luis Eduardo Juarez-Orozco, Octavio Martinez-Manzanera, Sergey V Nesterov, Sami Kajander, and Juhani Knuuti. The machine learning horizon in cardiac hybrid imaging. *European Journal of Hybrid Imaging*, 2(1):1–15, 2018.

[59] Luis Eduardo Juarez-Orozco, Octavio Martinez-Manzanera, Friso M van der Zant, Remco JJ Knol, and Juhani Knuuti. Deep learning in quantitative pet myocardial perfusion imaging: a study on cardiovascular event prediction. *Cardiovascular Imaging*, 13(1_Part_1):180–182, 2020.

[60] Polydoros N. Kampaktsis and Manolis Vavuranakis. Diastolic Function Evaluation. *JACC: Cardiovascular Imaging*, 13(1):336–337, January 2020.

[61] Garvan C. Kane, Barry L. Karon, Douglas W. Mahoney, Margaret M. Redfield, Veronique L. Roger, John C. Burnett, Steven J. Jacobsen, and Richard J. Rodeheffer. Progression of Left Ventricular Diastolic Dysfunction and Risk of Heart Failure. *JAMA*, 306(8), August 2011.

[62] Jamal Nasir Khan, Emma Gwyn Wilmot, Melanie Leggate, Anvesha Singh, Thomas Yates, Myra Nimmo, Kamlesh Khunti, Mark A. Horsfield, John Biglands, Patrick Clarysse, Pierre Croisille, Melanie Davies, and Gerry Patrick McCann. Subclinical diastolic dysfunction in young adults with Type 2 diabetes mellitus: a multiparametric contrast-enhanced cardiovascular magnetic resonance pilot study assessing potential mechanisms. *European Heart Journal - Cardiovascular Imaging*, 15(11):1263–1269, November 2014.

[63] Hyung Yoon Kim, Sung-Ji Park, Sang-Chol Lee, Shin Yi Chang, Eun-Kyoung Kim, Sung-A Chang, Jin-Oh Choi, Seung Woo Park, Sung-Mok Kim, Yeon Hyeon Choe, and Jae K. Oh. Comparison of global and regional myocardial strains in patients with heart failure with a preserved ejection fraction

vs hypertension vs age-matched control. *Cardiovascular Ultrasound*, 18(1):44, December 2020.

[64] Satoru Kishi, Samuel S. Gidding, Jared P. Reis, Laura A. Colangelo, Bharath A. Venkatesh, Anderson C. Armstrong, Akihiro Isogawa, Cora E. Lewis, Colin Wu, David R. Jacobs, Kiang Liu, and João A.C. Lima. Association of Insulin Resistance and Glycemic Metabolic Abnormalities With LV Structure and Function in Middle Age. *JACC: Cardiovascular Imaging*, 10(2):105–114, February 2017.

[65] Christoph Kolbitsch, Mark A. Ahlman, Cynthia Davies-Venn, Robert Evers, Michael Hansen, Devis Peressutti, Paul Marsden, Peter Kellman, David A. Bluemke, and Tobias Schaeffter. Cardiac and Respiratory Motion Correction for Simultaneous Cardiac PET/MR. *Journal of Nuclear Medicine*, 58(5):846–852, May 2017.

[66] Chrysi Koliaki, Stavros Liatis, and Alexander Kokkinos. Obesity and cardiovascular disease: revisiting an old relationship. *Metabolism*, 92:98–107, March 2019.

[67] Marvin A Konstam and François M Abboud. Ejection fraction: misunderstood and overrated (changing the paradigm in categorizing heart failure). *Circulation*, 135(8):717–719, 2017.

[68] Wojciech Kosmala and Thomas H. Marwick. Asymptomatic Left Ventricular Diastolic Dysfunction. *JACC: Cardiovascular Imaging*, 13(1):215–227, January 2020.

[69] Christian Kropidlowski, Michael Meier-Schroers, Daniel Kuetting, Alois Sprinkart, Hans Schild, Daniel Thomas, and Rami Homsi. CMR based measurement of aortic stiffness, epicardial fat, left ventricular myocardial strain and fibrosis in hypertensive patients. *IJC Heart & Vasculature*, 27:100477, April 2020.

[70] Vinayak Kumar, Alexander J. Ryu, Armando Manduca, Chaitanya Rao, Raymond J. Gibbons, Bernard J. Gersh, Krishnaswamy Chandrasekaran, Samuel J. Asirvatham, Philip A. Araoz, Jae K. Oh, Alexander C. Egbe, Atta Behfar, Barry A. Borlaug, and Nandan S. Anavekar. Cardiac MRI demonstrates compressibility in healthy myocardium but not in myocardium with reduced ejection fraction. *International Journal of Cardiology*, 322:278–283, January 2021.

[71] Thomas Küstner, Niccolo Fuin, Kerstin Hammernik, Aurelien Bustin, Haikun Qi, Reza Hajhosseiny, Pier Giorgio Masci, Radhouene Neji, Daniel Rueckert, René M Botnar, et al. Cinenet: deep learning-based 3d cardiac cine mri reconstruction with multi-coil complex-valued 4d spatio-temporal convolutions. *Scientific reports*, 10(1):1–13, 2020.

[72] Julio A. Lamprea-Montealegre, Leila R. Zelnick, Yoshio N. Hall, Nisha Bansal, and Ian H. de Boer. Prevalence of Hypertension and Cardiovascular Risk

According to Blood Pressure Thresholds Used for Diagnosis. *Hypertension*, 72(3):602–609, September 2018.

[73] Jerome Lamy, Gilles Soulat, Alban Redheuil, Morgane Evin, Elie Mousseaux, and Nadjia Kachenoura. Inter-study repeatability of left ventricular strain measurement using feature tracking on MRI cine images. In *2015 Computing in Cardiology Conference (CinC)*, pages 173–176, Nice, September 2015. IEEE.

[74] Hava Lester and Simon R Arridge. A survey of hierarchical non-linear medical image registration. *Pattern recognition*, 32(1):129–149, 1999.

[75] Leonard S Lilly. *Pathophysiology of heart disease: a collaborative project of medical students and faculty*. Lippincott Williams & Wilkins, 2012.

[76] Carolin Lim, Edyta Blaszczyk, Leili Riazy, Stephanie Wiesemann, Johannes Schüler, Florian von Knobelsdorff-Brenkenhoff, and Jeanette Schulz-Menger. Quantification of myocardial strain assessed by cardiovascular magnetic resonance feature tracking in healthy subjects—influence of segmentation and analysis software. *European Radiology*, December 2020.

[77] Joao A.C. Lima, Richmond Jeremy, William Guier, Sophie Bouton, Elias A. Zerhouni, Elliot McVeigh, Maurice B. Buchalter, Myron L. Weisfeldt, Edward P. Shapiro, and James L. Weiss. Accurate systolic wall thickening by nuclear magnetic resonance imaging with tissue tagging: Correlation with sonomicrometers in normal and ischemic myocardium. *Journal of the American College of Cardiology*, 21(7):1741–1751, June 1993.

[78] Boyang Liu, Ahmed M. Dardeer, William E. Moody, Manvir K. Hayer, Shanat Baig, Anna M. Price, Francisco Leyva, Nicola C. Edwards, and Richard P. Steeds. Reference ranges for three-dimensional feature tracking cardiac magnetic resonance: comparison with two-dimensional methodology and relevance of age and gender. *The International Journal of Cardiovascular Imaging*, November 2017.

[79] Huina Liu, Jiajia Wang, Yukun Pan, Yinghui Ge, Zhiping Guo, and Shihua Zhao. Early and Quantitative Assessment of Myocardial Deformation in Essential Hypertension Patients by Using Cardiovascular Magnetic Resonance Feature Tracking. *Scientific Reports*, 10(1):3582, December 2020.

[80] Ju-Hua Liu, Yan Chen, Michele Yuen, Zhe Zhen, Carmen Wing-Sze Chan, Karen Siu-Ling Lam, Hung-Fat Tse, and Kai-Hang Yiu. Incremental prognostic value of global longitudinal strain in patients with type 2 diabetes mellitus. *Cardiovascular Diabetology*, 15(1):22, December 2016.

[81] Wei Liu, Junjie Chen, Songbai Ji, J. Stacy Allen, Philip V. Bayly, Samuel A. Wickline, and Xin Yu. Harmonic phase MR tagging for direct quantification of lagrangian strain in rat hearts after myocardial infarction. *Magnetic Resonance in Medicine*, 52(6):1282–1290, December 2004.

[82] Xi Liu, Zhi-gang Yang, Yue Gao, Lin-jun Xie, Li Jiang, Bi-yue Hu, Kai-yue Diao, Ke Shi, Hua-yan Xu, Meng-ting Shen, Yan Ren, and Ying-kun Guo. Left ventricular subclinical myocardial dysfunction in uncomplicated type 2 diabetes mellitus is associated with impaired myocardial perfusion: a contrast-enhanced cardiovascular magnetic resonance study. *Cardiovascular Diabetology*, 17(1):139, December 2018.

[83] Bradley Christopher Lowekamp, David T Chen, Luis Ibáñez, and Daniel Blezek. The design of simpleitk. *Frontiers in neuroinformatics*, 7:45, 2013.

[84] Alicia M. Maceira, Luis Tuset-Sanchis, Miguel López-Garrido, Marta San Andres, M. Pilar López-Lereu, Jose V. Monmeneu, M. Pilar García-González, and Laura Higueras. Feasibility and reproducibility of feature-tracking-based strain and strain rate measures of the left ventricle in different diseases and genders: MR-FT Measures of Myocardial Strain. *Journal of Magnetic Resonance Imaging*, 47(5):1415–1425, May 2018.

[85] Tommaso Mansi, Xavier Pennec, Maxime Sermesant, Hervé Delingette, and Nicholas Ayache. ilogdemons: A demons-based registration algorithm for tracking incompressible elastic biological tissues. *International journal of computer vision*, 92(1):92–111, 2011.

[86] Tommaso Mansi, Xavier Pennec, Maxime Sermesant, Hervé Delingette, and Nicholas Ayache. iLogDemons: A Demons-Based Registration Algorithm for Tracking Incompressible Elastic Biological Tissues. *International Journal of Computer Vision*, 92(1):92–111, March 2011.

[87] Ali J. Marian and Eugene Braunwald. Hypertrophic Cardiomyopathy: Genetics, Pathogenesis, Clinical Manifestations, Diagnosis, and Therapy. *Circulation Research*, 121(7):749–770, September 2017.

[88] Thomas H. Marwick. Ejection Fraction Pros and Cons. *Journal of the American College of Cardiology*, 72(19):2360–2379, November 2018.

[89] Kristin McLeod, Adityo Prakosa, Tommaso Mansi, Maxime Sermesant, and Xavier Pennec. An incompressible log-domain demons algorithm for tracking heart tissue. In *International Workshop on Statistical Atlases and Computational Models of the Heart*, pages 55–67. Springer, 2011.

[90] E R McVeigh and E A Zerhouni. Noninvasive measurement of transmural gradients in myocardial strain with MR imaging. *Radiology*, 180(3):677–683, September 1991.

[91] Hannah V. Meyer, Timothy J. W. Dawes, Marta Serrani, Wenjia Bai, Paweł Tokarczuk, Jiashen Cai, Antonio de Marvao, Albert Henry, R. Thomas Lumbers, Jakob Gierten, Thomas Thumberger, Joachim Wittbrodt, James S. Ware, Daniel Rueckert, Paul M. Matthews, Sanjay K. Prasad, Maria L. Costantino, Stuart A. Cook, Ewan Birney, and Declan P. O'Regan. Genetic and functional

insights into the fractal structure of the heart. *Nature*, 584(7822):589–594, August 2020.

[92] Katherine T. Mills, Andrei Stefanescu, and Jiang He. The global epidemiology of hypertension. *Nature Reviews Nephrology*, 16(4):223–237, April 2020.

[93] Ioan-Alexandru Minciună, Olga Hilda Orășan, Iulia Minciună, Andrada-Luciana Lazar, Adela Viviana Sitar-Tăut, Monica Oltean, Raluca Tomoaia, Mihai Puiu, Dan-Andrei Sitar-Tăut, Dana Pop, and Angela Cozma. Assessment of subclinical diabetic cardiomyopathy by speckle-tracking imaging. *European Journal of Clinical Investigation*, 51(4), April 2021.

[94] William E. Moody, Robin J. Taylor, Nicola C. Edwards, Colin D. Chue, Fraz Umar, Tiffany J. Taylor, Charles J. Ferro, Alistair A. Young, Jonathan N. Townend, F. Leyva, and Richard P. Steeds. Comparison of magnetic resonance feature tracking for systolic and diastolic strain and strain rate calculation with spatial modulation of magnetization imaging analysis: CMR-Feature Tracking Versus Tagging. *Journal of Magnetic Resonance Imaging*, 41(4):1000–1012, April 2015.

[95] Daisuke Murai, Satoshi Yamada, Taichi Hayashi, Kazunori Okada, Hisao Nishino, Masahiro Nakabachi, Shinobu Yokoyama, Ayumu Abe, Ayako Ichikawa, Kota Ono, Sanae Kaga, Hiroyuki Iwano, Taisei Mikami, and Hiroyuki Tsutsui. Relationships of left ventricular strain and strain rate to wall stress and their afterload dependency. *Heart and Vessels*, 32(5):574–583, May 2017.

[96] Denisa Muraru, Umberto Cucchini, Sorina Mihăilă, Marcelo Haertel Miglioranza, Patrizia Aruta, Giacomo Cavalli, Antonella Cecchetto, Seena Padayattil-Josè, Diletta Peluso, Sabino Iliceto, and Luigi P. Badano. Left Ventricular Myocardial Strain by Three-Dimensional Speckle-Tracking Echocardiography in Healthy Subjects: Reference Values and Analysis of Their Physiologic and Technical Determinants. *Journal of the American Society of Echocardiography*, 27(8):858–871.e1, August 2014.

[97] Wilson Nadruz, Amil M. Shah, and Scott D. Solomon. Diastolic Dysfunction and Hypertension. *Medical Clinics of North America*, 101(1):7–17, January 2017.

[98] Arnold C.T. Ng, Matteo Bertini, See Hooi Ewe, Enno T. van der Velde, Dominic Y. Leung, Victoria Delgado, and Jeroen J. Bax. Defining Subclinical Myocardial Dysfunction and Implications for Patients With Diabetes Mellitus and Preserved Ejection Fraction. *The American Journal of Cardiology*, 124(6):892–898, September 2019.

[99] Christopher T Nguyen, James Dawkins, Xiaoming Bi, Eduardo Marbán, and Debiao Li. Diffusion tensor cardiac magnetic resonance reveals exosomes from cardiosphere-derived cells preserve myocardial fiber architecture after myocardial infarction. *JACC: Basic to Translational Science*, 3(1):97–109, 2018.

[100] Anna Nowogrodzki. The world's strongest mri machines are pushing human imaging to new limits. *Nature*, 563(7732):24–27, 2018.

[101] Milton Packer. Leptin-Aldosterone-Neprilysin Axis: Identification of Its Distinctive Role in the Pathogenesis of the Three Phenotypes of Heart Failure in People With Obesity. *Circulation*, 137(15):1614–1631, April 2018.

[102] Sung-Ji Park. The Role of Systolic Blood Pressure Reduction in Diastolic Dysfunction: RAAS Inhibition versus Non-RAAS Blood Pressure Lowering. *Journal of Cardiovascular Imaging*, 28(3):183, 2020.

[103] M Pascual. Effects of isolated obesity on systolic and diastolic left ventricular function. *Heart*, 89(10):1152–1156, October 2003.

[104] Virendra C. Patil, Kuldeep B. Shah, Jay D. Vasani, Pruthvi Shetty, and Harsha V. Patil. Diastolic dysfunction in asymptomatic type 2 diabetes mellitus with normal systolic function. *Journal of Cardiovascular Disease Research*, 2(4):213–222, October 2011.

[105] Gianni Pedrizzetti, Piet Claus, Philip J. Kilner, and Eike Nagel. Principles of cardiovascular magnetic resonance feature tracking and echocardiographic speckle tracking for informed clinical use. *Journal of Cardiovascular Magnetic Resonance*, 18(1):51, December 2016.

[106] Linda R Peterson, Alan D Waggoner, Kenneth B Schechtman, Timothy Meyer, Robert J Gropler, Benico Barzilai, and Víctor G Dávila-Román. Alterations in left ventricular structure and function in young healthy obese women. *Journal of the American College of Cardiology*, 43(8):1399–1404, April 2004.

[107] Mark A Peterzan, Oliver J Rider, and Lisa J Anderson. The Role of Cardiovascular Magnetic Resonance Imaging in Heart Failure. *Cardiac Failure Review*, page 115, 2016.

[108] Piotr Ponikowski, Adriaan A. Voors, Stefan D. Anker, Héctor Bueno, John G. F. Cleland, Andrew J. S. Coats, Volkmar Falk, José Ramón González-Juanatey, Veli-Pekka Harjola, Ewa A. Jankowska, Mariell Jessup, Cecilia Linde, Petros Nihoyannopoulos, John T. Parissis, Burkert Pieske, Jillian P. Riley, Giuseppe M. C. Rosano, Luis M. Ruilope, Frank Ruschitzka, Frans H. Rutten, and Peter van der Meer. 2016 ESC Guidelines for the diagnosis and treatment of acute and chronic heart failure: The Task Force for the diagnosis and treatment of acute and chronic heart failure of the European Society of Cardiology (ESC)Developed with the special contribution of the Heart Failure Association (HFA) of the ESC. *European Heart Journal*, 37(27):2129–2200, July 2016.

[109] Niek H. Prakken, Birgitta K. Velthuis, Arco J. Teske, Arend Mosterd, Willem P. Mali, and Maarten J. Cramer. Cardiac MRI reference values for athletes and

nonathletes corrected for body surface area, training hours/week and sex. *European Journal of Cardiovascular Prevention & Rehabilitation*, 17(2):198–203, April 2010.

[110] Esther Puyol-Anton, Bram Ruijsink, Wenjia Bai, Helene Langet, Mathieu De Craene, Julia A. Schnabel, Paolo Piro, Andrew P. King, and Matthew Sinclair. Fully automated myocardial strain estimation from cine MRI using convolutional neural networks. In *2018 IEEE 15th International Symposium on Biomedical Imaging (ISBI 2018)*, pages 1139–1143, Washington, DC, April 2018. IEEE.

[111] Mengyun Qiao, Yuanyuan Wang, Yi Guo, Lu Huang, Liming Xia, and Qian Tao. Temporally coherent cardiac motion tracking from cine MRI: Traditional registration method and modern CNN method. *Medical Physics*, 47(9):4189–4198, September 2020.

[112] Chen Qin, Wenjia Bai, Jo Schlemper, Steffen E. Petersen, Stefan K. Piechnik, Stefan Neubauer, and Daniel Rueckert. Joint Learning of Motion Estimation and Segmentation for Cardiac MR Image Sequences. *arXiv:1806.04066 [cs]*, June 2018. arXiv: 1806.04066.

[113] Chen Qin, Wenjia Bai, Jo Schlemper, Steffen E Petersen, Stefan K Piechnik, Stefan Neubauer, and Daniel Rueckert. Joint learning of motion estimation and segmentation for cardiac mr image sequences. In *International Conference on Medical Image Computing and Computer-Assisted Intervention*, pages 472–480. Springer, 2018.

[114] J. J. Rayner, S. Neubauer, and O. J. Rider. The paradox of obesity cardiomyopathy and the potential for weight loss as a therapy: The obesity paradox in heart failure. *Obesity Reviews*, 16(8):679–690, August 2015.

[115] Patricia Reant, Alexandre Metras, Dominique Detaille, Annabel Reynaud, Philippe Diolez, Beatrice Jaspard-Vinassa, Raymond Roudaut, Alexandre Ouattara, Laurent Barandon, Pierre Dos Santos, and Stephane Lafitte. Impact of Afterload Increase on Left Ventricular Myocardial Deformation Indices. *Journal of the American Society of Echocardiography*, 29(12):1217–1228, December 2016.

[116] Margaret M. Redfield, Steven J. Jacobsen, John C. Burnett, Douglas W. Mahoney, Kent R. Bailey, and Richard J. Rodeheffer. Burden of Systolic and Diastolic Ventricular Dysfunction in the Community: Appreciating the Scope of the Heart Failure Epidemic. *JAMA*, 289(2):194, January 2003.

[117] Matthew D Ritchey, Hilary K Wall, Mary G George, and Janet S Wright. Us trends in premature heart disease mortality over the past 50 years: Where do we go from here? *Trends in cardiovascular medicine*, 30(6):364–374, 2020.

[118] Robert Robinson, Vanya V Valindria, Wenjia Bai, Ozan Oktay, Bernhard Kainz, Hideaki Suzuki, Mihir M Sanghvi, Nay Aung, José Miguel Paiva, Filip Zemrak, et al. Automated quality control in image segmentation: application to the uk biobank cardiovascular magnetic resonance imaging study. *Journal of Cardiovascular Magnetic Resonance*, 21(1):1–14, 2019.

[119] Robert Robinson, Vanya V Valindria, Wenjia Bai, Ozan Oktay, Bernhard Kainz, Hideaki Suzuki, Mihir M Sanghvi, Nay Aung, José Miguel Paiva, Filip Zemrak, et al. Automated quality control in image segmentation: application to the uk biobank cardiovascular magnetic resonance imaging study. *Journal of Cardiovascular Magnetic Resonance*, 21(1):1–14, 2019.

[120] Michael Salerno. Feature Tracking by CMR. *JACC: Cardiovascular Imaging*, 11(2):206–208, February 2018.

[121] Jaskanwal D Sara, Takumi Toya, Riad Taher, Amir Lerman, Bernard Gersh, and Nandan S Anavekar. Asymptomatic Left Ventricle Systolic Dysfunction. *European Cardiology Review*, 15:e13, March 2020.

[122] Cian M Scannell, Mitko Veta, Adriana DM Villa, Eva C Sammut, Jack Lee, Marcel Breeuwer, and Amedeo Chiribiri. Deep-learning-based preprocessing for quantitative myocardial perfusion mri. *Journal of Magnetic Resonance Imaging*, 51(6):1689–1696, 2020.

[123] Jo Schlemper, Jose Caballero, Joseph V Hajnal, Anthony N Price, and Daniel Rueckert. A deep cascade of convolutional neural networks for dynamic mr image reconstruction. *IEEE transactions on Medical Imaging*, 37(2):491–503, 2017.

[124] A. Schuster, V.-C. Stahnke, C. Unterberg-Buchwald, J.T. Kowallick, P. Lamata, M. Steinmetz, S. Kutty, M. Fasshauer, W. Staab, J.M. Sohns, B. Bigalke, C. Ritter, G. Hasenfuß, P. Beerbaum, and J. Lotz. Cardiovascular magnetic resonance feature-tracking assessment of myocardial mechanics: Intervendor agreement and considerations regarding reproducibility. *Clinical Radiology*, 70(9):989–998, September 2015.

[125] W Paul Segars, G Sturgeon, S Mendonca, Jason Grimes, and Benjamin MW Tsui. 4d xcat phantom for multimodality imaging research. *Medical physics*, 37(9):4902–4915, 2010.

[126] Hisham Sharif, Stephen Ting, Lynsey Forsythe, Gordon McGregor, Prithwish Banerjee, Deborah O'Leary, David Ditor, Keith George, Daniel Zehnder, and David Oxborough. Layer-specific systolic and diastolic strain in hypertensive patients with and without mild diastolic dysfunction. *Echo Research and Practice*, 5(1):41–49, March 2018.

[127] Wenzhe Shi, Xiahai Zhuang, Haiyan Wang, Simon Duckett, Duy VN Luong, Catalina Tobon-Gomez, KaiPin Tung, Philip J Edwards, Kawal S Rhode,

Reza S Razavi, et al. A comprehensive cardiac motion estimation framework using both untagged and 3-d tagged mr images based on nonrigid registration. *IEEE transactions on medical imaging*, 31(6):1263–1275, 2012.

[128] Georgios Simantiris and Georgios Tziritas. Cardiac mri segmentation with a dilated cnn incorporating domain-specific constraints. *IEEE Journal of Selected Topics in Signal Processing*, 14(6):1235–1243, 2020.

[129] Otto A. Smiseth, Hans Torp, Anders Opdahl, Kristina H. Haugaa, and Stig Urheim. Myocardial strain imaging: how useful is it in clinical decision making? *European Heart Journal*, 37(15):1196–1207, April 2016.

[130] Scott D Solomon, Rajesh Janardhanan, Anil Verma, Mikhail Bourgoun, William L Daley, Das Purkayastha, Yves Lacourcière, Stephen E Hippler, Harold Fields, Tasneem Z Naqvi, Sharon L Mulvagh, J Malcolm O Arnold, James D Thomas, Michael R Zile, and Gerard P Aurigemma. Effect of angiotensin receptor blockade and antihypertensive drugs on diastolic function in patients with hypertension and diastolic dysfunction: a randomised trial. *The Lancet*, 369(9579):2079–2087, June 2007.

[131] Syed Amin Tabish. Is diabetes becoming the biggest epidemic of the twenty-first century? *International Journal of health sciences*, 1(2):V, 2007.

[132] Lennart Tautz, Anja Hennemuth, and Heinz-Otto Peitgen. Motion analysis with quadrature filter based registration of tagged mri sequences. In *International Workshop on Statistical Atlases and Computational Models of the Heart*, pages 78–87. Springer, 2011.

[133] Sian Taylor-Phillips and Chris Stinton. Fatigue in radiology: a fertile area for future research. *The British journal of radiology*, 92(1099):20190043, 2019.

[134] D. Thomas, V.A. Ferrari, M. Janik, D.H. Kim, S. Pickup, J.D. Glickson, and R. Zhou. Quantitative assessment of regional myocardial function in a rat model of myocardial infarction using tagged MRI. *Magnetic Resonance Materials in Physics, Biology and Medicine*, 17(3-6):179–187, December 2004.

[135] Catalina Tobon-Gomez, Mathieu De Craene, Kristin Mcleod, Lennart Tautz, Wenzhe Shi, Anja Hennemuth, Adityo Prakosa, Hengui Wang, Gerry Carr-White, Stam Kapetanakis, et al. Benchmarking framework for myocardial tracking and deformation algorithms: An open access database. *Medical image analysis*, 17(6):632–648, 2013.

[136] Filippos Triposkiadis, Javed Butler, Francois M Abboud, Paul W Armstrong, Stamatis Adamopoulos, John J Atherton, Johannes Backs, Johann Bauersachs, Daniel Burkhoff, Robert O Bonow, Vijay K Chopra, Rudolf A de Boer, Leon de Windt, Nazha Hamdani, Gerd Hasenfuss, Stephane Heymans, Jean-Sébastien Hulot, Marvin Konstam, Richard T Lee, Wolfgang A Linke, Ida G Lunde, Alexander R Lyon, Christoph Maack, Douglas L Mann, Alexandre

Mebazaa, Robert J Mentz, Petros Nihoyannopoulos, Zoltan Papp, John Parissis, Thierry Pedrazzini, Giuseppe Rosano, Jean Rouleau, Petar M Seferovic, Ajay M Shah, Randall C Starling, Carlo G Tocchetti, Jean-Noel Trochu, Thomas Thum, Faiez Zannad, Dirk L Brutsaert, Vincent F Segers, and Gilles W De Keulenaer. The continuous heart failure spectrum: moving beyond an ejection fraction classification. *European Heart Journal*, 40(26):2155–2163, July 2019.

[137] HG Tsang, NA Rashdan, CBA Whitelaw, BM Corcoran, KM Summers, and VE MacRae. Large animal models of cardiovascular disease. *Cell biochemistry and function*, 34(3):113–132, 2016.

[138] Johnathan D. Tune, Adam G. Goodwill, Daniel J. Sassoon, and Kieren J. Mather. Cardiovascular consequences of metabolic syndrome. *Translational Research*, 183:57–70, May 2017.

[139] M Usman, B Ruijsink, MS Nazir, G Cruz, and C Prieto. Free breathing whole-heart 3d cine mri with self-gated cartesian trajectory. *Magnetic resonance imaging*, 38:129–137, 2017.

[140] Juan José Vaquero and Paul Kinahan. Positron emission tomography: current challenges and opportunities for technological advances in clinical and preclinical imaging systems. *Annual review of biomedical engineering*, 17:385–414, 2015.

[141] Bharath Ambale Venkatesh, Sirisha Donekal, Kihei Yoneyama, Colin Wu, Verônica R.S. Fernandes, Boaz D. Rosen, Monda L. Shehata, Robyn McClelland, David A. Bluemke, and João A.C. Lima. Regional myocardial functional patterns: Quantitative tagged magnetic resonance imaging in an adult population free of cardiovascular risk factors: The multi-ethnic study of atherosclerosis (MESA): Reference Values of Strain From Tagged MRI. *Journal of Magnetic Resonance Imaging*, 42(1):153–159, July 2015.

[142] Tom Vercauteren, Xavier Pennec, Aymeric Perchant, and Nicholas Ayache. Diffeomorphic demons: Efficient non-parametric image registration. *NeuroImage*, 45(1):S61–S72, 2009.

[143] J.-U. Voigt, G. Pedrizzetti, P. Lysyansky, T. H. Marwick, H. Houle, R. Baumann, S. Pedri, Y. Ito, Y. Abe, S. Metz, J. H. Song, J. Hamilton, P. P. Sengupta, T. J. Kolias, J. d'Hooge, G. P. Aurigemma, J. D. Thomas, and L. P. Badano. Definitions for a common standard for 2D speckle tracking echocardiography: consensus document of the EACVI/ASE/Industry Task Force to standardize deformation imaging. *European Heart Journal - Cardiovascular Imaging*, 16(1):1–11, January 2015.

[144] Beatrice von Jeinsen, Ramachandran S. Vasan, David D. McManus, Gary F. Mitchell, Susan Cheng, and Vanessa Xanthakis. Joint influences of obesity,

diabetes, and hypertension on indices of ventricular remodeling: Findings from the community-based Framingham Heart Study. *PLOS ONE*, 15(12):e0243199, December 2020.

[145] Siu-Hin Wan, Mark W. Vogel, and Horng H. Chen. Pre-Clinical Diastolic Dysfunction. *Journal of the American College of Cardiology*, 63(5):407–416, February 2014.

[146] Qin Wang, Qi-Wei Sun, Dan Wu, Ming-Wu Yang, Rong-Juan Li, Bo Jiang, Jiao Yang, Zhi-An Li, Ying Wang, and Ya Yang. Early Detection of Regional and Global Left Ventricular Myocardial Function Using Strain and Strain-rate Imaging in Patients with Metabolic Syndrome. *Chinese Medical Journal*, 128(2):226–232, January 2015.

[147] Yi-Chih Wang, Chang-seng Liang, Deepa M. Gopal, Nir Ayalon, Courtney Donohue, Rajalakshmi Santhanakrishnan, Harpaul Sandhu, Alejandro J. Perez, Jill Downing, Noyan Gokce, Wilson S. Colucci, and Jennifer E. Ho. Preclinical Systolic and Diastolic Dysfunctions in Metabolically Healthy and Unhealthy Obese Individuals. *Circulation: Heart Failure*, 8(5):897–904, September 2015.

[148] Wenzhe Shi, Xiahai Zhuang, Haiyan Wang, S. Duckett, D. V. N. Luong, C. Tobon-Gomez, KaiPin Tung, P. J. Edwards, K. S. Rhode, R. S. Razavi, S. Ourselin, and D. Rueckert. A Comprehensive Cardiac Motion Estimation Framework Using Both Untagged and 3-D Tagged MR Images Based on Nonrigid Registration. *IEEE Transactions on Medical Imaging*, 31(6):1263–1275, June 2012.

[149] Karina Wierzbowska-Drabik, Łukasz Chrzanowski, Anna Kapusta, Barbara Uznańska-Loch, Edyta Płońska, Maria Krzemińska-Pakuła, Małgorzata Kurpesa, Tomasz Rechciński, Ewa Trzos, and Jarosław D. Kasprzak. Severe Obesity Impairs Systolic and Diastolic Heart Function - The Significance of Pulsed Tissue Doppler, Strain, and Strain Rate Parameters. *Echocardiography*, 30(8):904–911, September 2013.

[150] Lukas Wissmann, Claudio Santelli, William P Segars, and Sebastian Kozerke. Mrxcat: Realistic numerical phantoms for cardiovascular magnetic resonance. *Journal of Cardiovascular Magnetic Resonance*, 16(1):1–11, 2014.

[151] Chih M. Wong, Nathaniel M. Hawkins, Pardeep S. Jhund, Michael R. MacDonald, Scott D. Solomon, Christopher B. Granger, Salim Yusuf, Marc A. Pfeffer, Karl Swedberg, Mark C. Petrie, and John J.V. McMurray. Clinical Characteristics and Outcomes of Young and Very Young Adults With Heart Failure. *Journal of the American College of Cardiology*, 62(20):1845–1854, November 2013.

[152] Fan Yang, Yan Zhang, Pinggui Lei, Lihui Wang, Yuehong Miao, Hong Xie, and Zhu Zeng. A Deep Learning Segmentation Approach in Free-Breathing Real-

Time Cardiac Magnetic Resonance Imaging. *BioMed Research International*, 2019:1–12, July 2019.

[153] Rehab Ibrahim Yaseen, Mahmoud Kamel Ahmed, and Waleed Abdou Hamed. Assessment of abnormal LV myocardial deformation properties in obese patients by 2D based strain and strain rate imaging. *The Egyptian Heart Journal*, 67(3):183–191, September 2015.

[154] Susan B Yeon, Nathaniel Reichek, Barbara A Tallant, João A.C Lima, Linda P Calhoun, Neil R Clark, Eric A Hoffman, Kalon K.L Ho, and Leon Axel. Validation of in vivo myocardial strain measurement by magnetic resonance tagging with sonomicrometry. *Journal of the American College of Cardiology*, 38(2):555–561, August 2001.

[155] A A Young, L Axel, L Dougherty, D K Bogen, and C S Parenteau. Validation of tagging with MR imaging to estimate material deformation. *Radiology*, 188(1):101–108, July 1993.

[156] Hanchao Yu, Shanhui Sun, Haichao Yu, Xiao Chen, Honghui Shi, Thomas S. Huang, and Terrence Chen. FOAL: Fast Online Adaptive Learning for Cardiac Motion Estimation. In *2020 IEEE/CVF Conference on Computer Vision and Pattern Recognition (CVPR)*, pages 4312–4322, Seattle, WA, USA, June 2020. IEEE.

[157] Lin Zhang, Lei Zhang, Xuanqin Mou, and David Zhang. A comprehensive evaluation of full reference image quality assessment algorithms. In *2012 19th IEEE International Conference on Image Processing*, pages 1477–1480. IEEE, 2012.

[158] Lin Zhang, Lei Zhang, Xuanqin Mou, and David Zhang. A comprehensive evaluation of full reference image quality assessment algorithms. In *2012 19th IEEE International Conference on Image Processing*, pages 1477–1480, Orlando, FL, USA, September 2012. IEEE.

[159] Hang Zhao, Orazio Gallo, Iuri Frosio, and Jan Kautz. Loss functions for image restoration with neural networks. *IEEE Transactions on computational imaging*, 3(1):47–57, 2016.

[160] Qiao Zheng, Hervé Delingette, and Nicholas Ayache. Explainable cardiac pathology classification on cine MRI with motion characterization by semi-supervised learning of apparent flow. *arXiv:1811.03433 [cs, stat]*, March 2019. arXiv: 1811.03433.

[161] Bo Zhu, J Liu, Neha Koonjoo, B Rosen, and Matthew S Rosen. Automated pulse sequence generation (autoseq) and neural network decoding for fast quantitative mr parameter measurement using continuous and simultaneous rf transmit and receive. In *ISMRM Annual Meeting & Exhibition*, volume 1090, 2019.

[162] Bo Zhu, Jeremiah Z Liu, Stephen F Cauley, Bruce R Rosen, and Matthew S Rosen. Image reconstruction by domain-transform manifold learning. *Nature*, 555(7697):487–492, 2018.

[163] Bo Zhu, Jeremiah Z. Liu, Bruce R. Rosen, and Matthew S. Rosen. Image reconstruction by domain transform manifold learning. *arXiv:1704.08841 [cs]*, April 2017. arXiv: 1704.08841.

[164] Paul Z Zimmet. Diabetes and its drivers: the largest epidemic in human history? *Clinical diabetes and endocrinology*, 3(1):1–8, 2017.

[165] Clement Zotti, Zhiming Luo, Alain Lalande, and Pierre-Marc Jodoin. Convolutional neural network with shape prior applied to cardiac mri segmentation. *IEEE journal of biomedical and health informatics*, 23(3):1119–1128, 2018.

[166] Ewa Świerblewska, Jacek Wolf, Katarzyna Kunicka, Beata Graff, Katarzyna Polonis, Michał Hoffmann, Marzena Chrostowska, Anna Szyndler, Piotr Bandosz, Beata Graff, and Krzysztof Narkiewicz. Prevalence and distribution of left ventricular diastolic dysfunction in treated patients with long-lasting hypertension. *Blood Pressure*, 27(6):376–384, November 2018.